Doctorate Dissertation

博士論文

The effect of interaction with the interstellar medium on the over-ionisation of plasma in evolved supernovae remnants (進化した超新星残骸における過電離プラズマの形成過程への星間環境の影響)

A Dissertation Submitted for Degree of Doctor of Philosophy

December 2018

平成 30 年 12 月博士（理学）申請

Department of Physics, Graduate School of Science,
The University of Tokyo

東京大学大学院理学系研究科物理学専攻

Miho Katsuragawa

桂川　美穂

Abstract

We studied the evolution of plasma of evolved supernova remnants (SNRs). We firstly analysed data from a SNR CTB 1 observation with Suzaku, which is an X-ray astronomical satellite having a superb sensitivity for observing fainter diffuse objects. CTB 1 has a non-thermal radio shell with centre-filled thermal X-ray emissions. We found recombining plasma in southwestern region of CTB 1 where an atomic cloud is detected. This is the first result that indicates the association between the formation of recombining plasma and an atomic cloud.

Secondary, in order to study physical and astrophysical causes of the formation of the recombining plasma in evolved SNRs, we developed a new framework which enables us to simulate the evolution of plasma in SNRs with an age of $> 10^4$ years. The code provides a method for generating X-ray spectra and images of evolved SNRs based on a one-dimensional Lagrangian hydrodynamics simulation. We include physical processes of shock heating, energy exchange by Coulomb interaction, radiative cooling, evolution of ionisation states.

To study the relation between the formation of the recombining plasma of SNRs and their surrounding gas, we simulate the time evolution of an electron temperature and ion fractions in each interstellar medium (ISM) density (1, 3, 10, and 30 cm^{-3}). As an indicator of describing the ionisation state, we use ionisation temperatures estimated from the ion fractions. From the study of the electron and ionisation temperatures, we obtain the results that the recombining plasma is produced in evolved SNRs ($\sim 10^4$ yr) which exploded in the dense ISM.

In order to investigate capability of our framework, we compare the simulation results with an observation of a SNR Cygnus Loop which is a bright shell-like SNR with an old age. Our code produces basic observational figures and characteristics including the size, spectrum, electron and ionisation temperatures of the evolved shell-like SNR Cygnus Loop. We demonstrate that our code is able to follow time evolution of an SNR from the early phase of its SN explosion to an old age of $\sim 10^4$ yr without any significant error.

We also compare simulation results for ISM densities $n_{ISM} = 1$, 3, 10, and 30 cm^{-3} with observations of evolved SNRs that show the presence of the recombining plasma. The simulations with the ISM densities of 10 or 30 cm^{-3} well agree with observational trends. We successfully demonstrate that the ionisation temperatures of the simulation models are in excellent agreement with the observed values. The lower electron temperatures with an age of $> 10^4$ yr than

the ionisation temperatures obtained from simulation are consistent with observational trends. The RP can be explained by the combination of simple processes: hydrodynamic processes including the shock heating and adiabatic cooling, energy exchanges between ions and electrons via Coulomb interactions, and collisional ionisations and recombinations of ions.

Contents

Chapter 1

Introduction

Supernova (SN) explosions have been thought the sources from which most heavy elements in the universe are produced. A supernova remnant (SNR) is the aftermath of an exploding star that has blasted matter into space in an ever-expanding gas cloud. SNRs play important roles to explain evolution of a galaxy because of the huge amount of energy ($\sim 10^{51}$ erg) they release into the surrounding environment. This violent release of energy heats up the ambient gas, causing it to emit X-rays. This X-ray signal is of great interest as it provides information about the thermal, dynamical processes of the heated electrons and ions and also provides information about the type of heavy elements produced by a supernova explosion.

The ejected matter (ejecta) in the explosion of the progenitor star goes through a free expansion phase and in the process forms a shock wave as the ejecta sweep up interstellar medium (ISM). The shocked ejecta and ISM expand adiabatically (adiabatic expansion phase) and they gradually move to the next phase in which they are strongly affected by radiative cooling (radiative cooling phase).

An SNR forms a shell-like structure seen in the radio and X-ray wavelength. Ions in the plasma heated by the shock wave in SNRs are ionised and reach a state of collisional ionisation equilibrium (CIE). However, some of SNRs have unique structures such as a radio bright shell, but with a centre-filled X-ray emission. These SNRs are called mixed-morphology (MM) SNRs.

Recent X-ray observations revealed that some of the MM-SNRs have plasmas in which the recombination process becomes more dominant than the ionisation process. In most of these MM-SNRs having the recombining plasma, association of molecular and atomic clouds are observed. This implies that the evolution and formation process of SNRs are considered to be deeply related to the environment of the ambient gas, though they are not fully understood.

In order to study the formation of MM-SNRs, it is necessary to investigate how surrounding environment affects the evolution of such SNRs. However, only 16 SNRs have shown the presence of the RP. Moreover, plasma models used for spectral analysis in X-ray observations do not take the time evolution of the electron temperature into account.

Recently, a series of theoretical studies by means of numerical simulations that calculate both temperature evolution and resultant ion fractions of young SNRs ($\sim$ 100–1000 yr) have been performed. In young SNRs, the results of the simulations are mostly compared with the central energy of X-ray lines of irons observed in X-ray spectra. However, for evolved SNRs which are considered to stay in the radiative cooling phase, we need simulations of SNRs for more than $\sim 10^4$ yrs. In order to study the evolution of plasma of these evolved SNRs, we need a code that takes the radiative cooling process into account.

In this thesis, we firstly analyse Suzaku observation of a MM SNR, CTB 1, and report the significant detection of the signature of recombining plasma in the southwestern region of CTB 1, in the vicinity of an atomic cloud. This is the first result that shows an association of an atomic cloud with the region of recombining plasma. In order to preform quantitative study, we have developed a new framework for simulating evolved SNRs which include the radiative cooling process. The code includes the formation of X-ray spectra and images based on calculated evolutions of electron and ion temperatures and ion fractions. This enables us to compare our results with X-ray observation, directly. By using the framework, we compare results of the simulation results with observations of MM-SNRs that exhibit the signature of recombining plasma.

This thesis organised as follows. We review the SNRs and the evolution of plasmas in chapter 2. The basic characteristics of the instruments on board Suzaku are described in chapter 3. Chapter 4 provides the observation results of CTB 1, and we give detailed description of our new framework in Chapter 5. In Chapter 6 we discuss how the code is validated and discuss the relationship between the recombining plasma and the ISM density. In chapter 7, we compare the simulation results with observations and discuss the formation process of the recombining plasma. Chapter 8 gives our conclusions of this thesis.

Chapter 2

Review

Where did all the heavy elements in our universe come from? One of the strongest candidates for the origin of heavy elements are supernovae (SNe) that are stars that end their lives in an explosion. Supernova explosions release kinetic energy of $\sim 10^{51}$ erg and eject matter including heavy elements into space. The ejected matter from the progenitor (ejecta) expands sweeping the inter stellar medium (ISM). SNe leaves behind a supernova remnant (SNR) composed of the ejecta and ISM, which create a strong collision-less shock waves. The electromagnetic frequencies emanating from SNRs such as radio, optical, X-ray, and gamma rays are not fully understood. In this chapter, we provide a basic overview of the characteristics of SNe and SNRs and the evolution processes of SNRs.

2.1 Supernova explosion

The mechanism of supernova explosions is based on the presence or absence of certain features in their optical spectra and brightness curves as shown in Table 2.1. If absorption lines of hydrogen (H) Balmer series do not appear in optical spectra, then the SNe is classified as Type I, otherwise they are classified as Type II SNe (Minkowski 1939; 1940). Type I SNe are sub-categorised by silicon (Si) and helium (He) absorption lines (Elias et al. 1985, Wheeler et al. 1987). Type Ia SNe contain an obvious Si absorption lines, whereas Type Ib and Ic SNe have no Si absorption lines. In addition, Type Ib SNe display He absorption lines and Type Ic SNe show no He absorption lines. Type II SNe are classified into four types that are in terms of brightness curves or spectra. The brightness curves of Type II-P SNe are plateau, while Type II-L SNe shows linear brightness curves (Barbon et al. 1973). Type II-n SNe have narrow width hydrogen absorption lines in the spectra (Schlegel 1990). Type II-b SNe show weak hydrogen absorption line in its initial spectrum and its line becomes undetectable (Filippenko 1988, Utrobin 1996).

Type Ia was the results of an explosion of a carbon–oxygen (C/O) white dwarf limited to

Table 2.1: Classification of Supernovae.

Type	Class	Feature of a spectrum			Feature of a brightness curve
		H	Si	He	
I	Ia	×	◯		
	Ib	×	×	◯	
	Ic	×	×	×	
II	II-P	◯			plato
	II-L	◯			increase
	II-n	◯(narrow line)			
	II-b	◯(becomes undetectable)			

below near-Chandrasekhar mass ($\sim 1.4\ M_\odot$) that has a binary system. One of the formation scenario for Type Ia is the single-degenerate model with a near-Chandrasekhar-mass white dwarf. When the white dwarf increases in mass by the accretion from the companion and approaches the Chandrasekhar mass, carbon burning ignites deep in the interior (e.g. Nomoto 1982). The other scenario is the double-degenerate model that invokes the merger of two C/O white dwarfs (e.g. Webbink 1984). Since the heavy elements of silicon to iron are selectively synthesised in Type Ia SNe, thus the Ia SNe chiefly provide them into the universe (Nomoto et al. 1984, Iwamoto et al. 1999).

The other type of SNe is an explosion of massive stars ($\geq 10\ M_\odot$) via the core collapse. Nucleosynthesis is proceeded in the core of the massive star, at which point pressure and gravity are in balanced because of the high temperature. When the gravitational force becomes greater than what the Fe core can sustain and a pressure imbalance occurs, the star collapses into a compact object such as a neutron star or a black hole. In this explosion, the gravitational energy of $\sim 10^{53}$ erg is released. Neutrinos carry away 99% of the gravitational energy and the remaining ($\sim 1\%$) is carried away as kinetic energy.

2.2 Supernova remnants

2.2.1 Standard Evolution of Supernova Remnants

The time evolution of SNRs are generally divided into the several phase: the free expansion phase, the adiabatic phase, and the radiative cooling phase (Cioffi et al. 1988, Truelove & Mckee 1999). In the following section we examine each phase assuming of the uniform ambient gas.

Free Expansion Phase

After a SN explosion, the ejecta expands though the thin ISM at approximately constant velocity, since a mass of the ISM swept up by the ejecta can be ignored for the total ejected

mass M_{ej}. The period of the expansion for a constant velocity is called the free expansion phase. The velocity of the ejecta v_f is a function of the kinetic energy of the explosion ($E_{SN} \sim 10^{51}$ erg) as

$$v_f = \sqrt{\frac{2E_{SN}}{M_{ej}}} = 8.5 \times 10^8 \left(\frac{E}{10^{51}\ \mathrm{erg}}\right)^{\frac{1}{2}} \left(\frac{M_{ej}}{1.4\ M_\odot}\right)^{-\frac{1}{2}}\ \mathrm{cm\ s^{-1}}. \tag{2.1}$$

The evolution of SNRs finishes the free expansion phase and evolves to the next phase, when the mass of the swept-up ISM becomes comparable with M_{ej}, indicated by

$$M_{ej} = \frac{4}{3}\pi R_f^3 \mu n_0, \tag{2.2}$$

where R_f, μ, and n_0 are the radius of the remnant, mean atomic mass, and number density of the ISM, respectively. The timescale of the free expansion phase t_f is calculated from $R_f = v_f t_f$,

$$t_f = 2.5 \times 10^2 \left(\frac{E}{10^{51}\ \mathrm{erg}}\right)^{-\frac{1}{2}} \left(\frac{M_{ej}}{1.4\ M_\odot}\right)^{\frac{5}{6}} \left(\frac{n_0}{1\ \mathrm{cm^{-3}}}\right)^{-\frac{1}{3}}\ \mathrm{yr}. \tag{2.3}$$

The typical free expansion timescale is $\sim 10^2$–10^3 yr.

Adiabatic Phase (Sedov Phase)

When the mass of the swept-up ISM becomes greater than the ejecta mass, the shock wave forms and expands adiabatically. This causes the velocity of the ejecta to decrease and the loss of energy is exchanged to the thermal energy of shocked matter. The shock wave moving in the ISM is called the forward shock (FS), while the reverse shock (RS) wave goes into the ejecta. The schematic view of a SNR is shown in Figure 2.1.

The gas where the shock wave passed is compressed and heated. Figure 2.2 shows a schematic picture around the shock wave. Taking a coordinate system in which the shock is at rest, the conservation of mass, momentum and energy flux between upstream and downstream as follows:

$$\rho_1 v_1 = \rho_2 v_2, \tag{2.4}$$

$$\rho_1 v_1^2 + P_1 = \rho_2 v_2^2 + P_2, \tag{2.5}$$

$$\{\rho_1(u_1 + \frac{1}{2}v_1^2) + P_1\}v_1 = \{\rho_2(u_2 + \frac{1}{2}v_2^2) + P_2\}v_2, \tag{2.6}$$

where ρ, v, P, and u are the density, velocity, pressure, and internal energy of upstream (1) and downstream (2), respectively. Using the ratio for specific heat $\gamma(= C_p/C_v)$, equations (2.4),

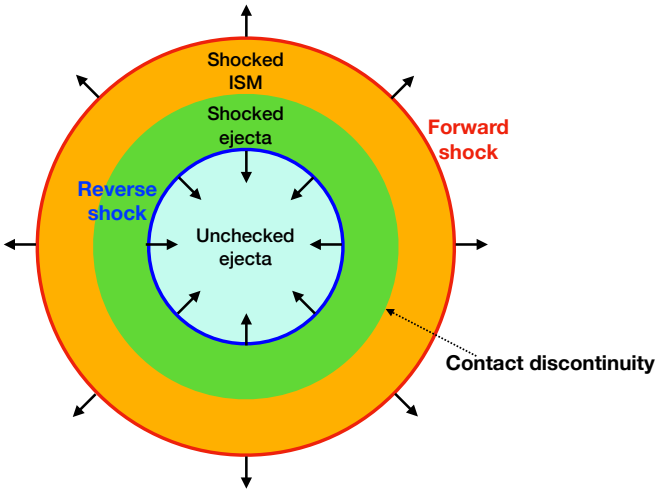

Figure 2.1: A schematic view of a SNR in the transition phase between the free expansion and the adiabatic phase.

(2.5), and (2.6) take the form

$$\frac{\rho_1}{\rho_2} = \frac{(\gamma+1)P_1+(\gamma-1)P_2}{(\gamma-1)P_1+(\gamma+1)P_2} \tag{2.7}$$

$$\frac{P_1}{P_2} = \frac{(\gamma+1)\rho_1-(\gamma-1)\rho_2}{(\gamma+1)P_2-(\gamma-1)P_1} \tag{2.8}$$

$$\frac{T_2}{T_1} = \frac{P_2\rho_1}{P_1\rho_2} = \frac{P_2}{P_1}\frac{(\gamma-1)P_1+(\gamma-1)P_2}{(\gamma-1)P_1+(\gamma+1)P_2}. \tag{2.9}$$

Here, the shock velocity v_s is regard as v_1. Assuming the shock ($P_2/P_1 \gg 1$), the post-shock temperature is described as,

$$kT_2 = \mu m_H \frac{P_2}{\rho_2} = \frac{2(\gamma-1)}{(\gamma+1)^2}\mu m_H v_s^2, \tag{2.10}$$

where k is the Boltzmann constant. In the case of the non-relativistic single atomic gas ($\gamma = 5/3$), the ratio of the density and velocity are given as $\rho_2/\rho_1 \sim 4$ and $v_2/v_1 \sim 4$, in which case we obtain the post-shock temperature such that

$$kT_2 = \frac{3}{16}\mu m_H v_s^2, \tag{2.11}$$

which implies that the kinetic energy is converted into the thermal energy.

The evolution of the adiabatic phase of the SNR shock wave is modelled on a point source SNR explosion. This propagation is solved analytical (Sedov-Taylor solution) by Sedov (1959)

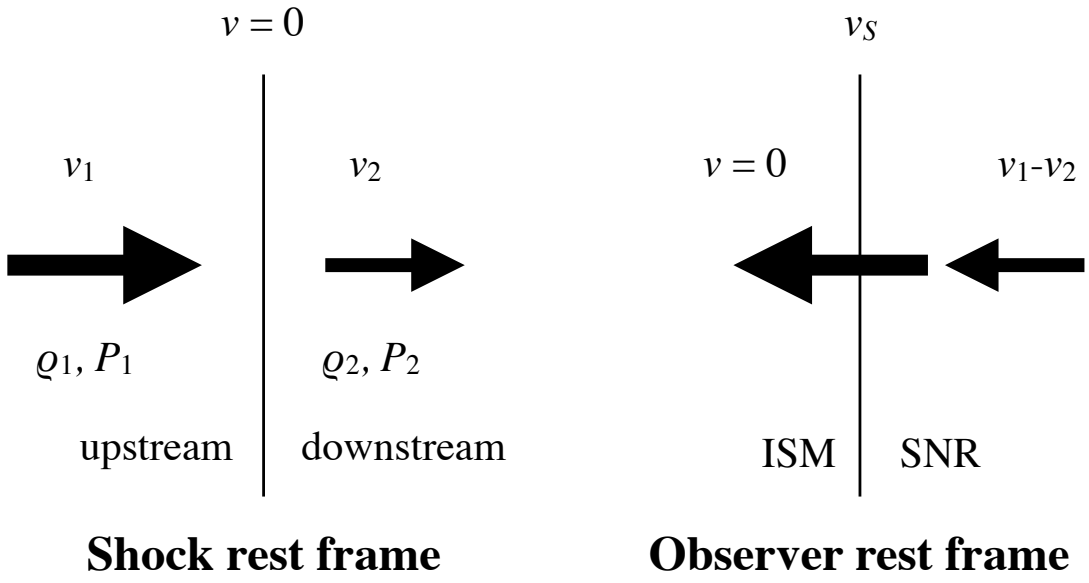

Figure 2.2: A schematic view around the shock front and gas flow in the shock rest frame (left) and observer rest frame (right).

and Taylor (1950). The radius and velocity of the blast wave and the post-shock temperature are described as

$$R_s = 4 \times 10^{19} \left(\frac{E}{10^{51}\ \mathrm{erg}}\right)^{\frac{1}{5}} \left(\frac{t}{10^4\ \mathrm{yr}}\right)^{\frac{2}{5}} \left(\frac{n_0}{1\ \mathrm{cm}^{-3}}\right)^{-\frac{1}{5}}\ \mathrm{cm}, \tag{2.12}$$

$$v_s = \frac{dR_s}{dt} = 5 \times 10^7 \left(\frac{E}{10^{51}\ \mathrm{erg}}\right)^{\frac{1}{5}} \left(\frac{t}{10^4\ \mathrm{yr}}\right)^{-\frac{3}{5}} \left(\frac{n_0}{1\ \mathrm{cm}^{-3}}\right)^{-\frac{1}{5}}\ \mathrm{cm\ s}^{-1}, \tag{2.13}$$

$$T_s = 3 \times 10^6 \left(\frac{E}{10^{51}\ \mathrm{erg}}\right)^{\frac{2}{5}} \left(\frac{t}{10^4\ \mathrm{yr}}\right)^{-\frac{6}{5}} \left(\frac{n_0}{1\ \mathrm{cm}^{-3}}\right)^{-\frac{2}{5}}\ \mathrm{K}. \tag{2.14}$$

The time evolution of the shock positions and velocities for the forward shock and reverse shock are shown in Figure 2.3. 70% of the initial kinematic energy is transformed into the thermal energy of shocked matter (Chevalier 1974). This adiabatic phase continues for a few ten thousand years.

Radiative Cooling Phase

Both the velocity and temperature of the shock wave decreases with the passage of time. When the temperature decreases by $\sim 10^6$ K, the SNR transitions out of the adiabatic phase and into a phase where its energy loss is effectively due to the emission of X-ray radiation (radiative cooling phase). Figure 2.4 shows cooling rates as a function of the temperature. When the

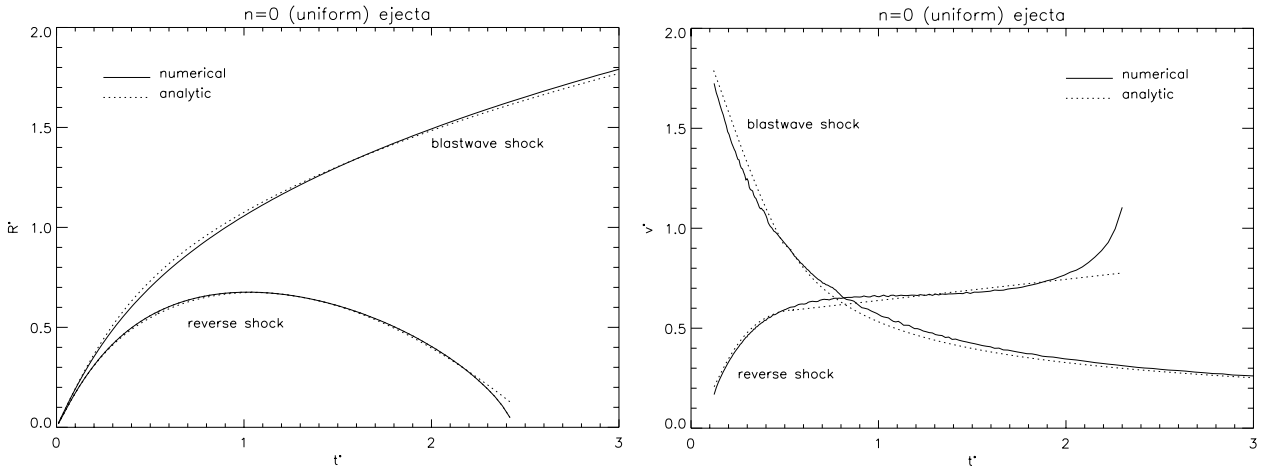

Figure 2.3: Shock positions and velocities for blast-wave and reverse shocks in remnants of n = 7 ejecta ($\rho \propto r^{-n}$). Note that the reverse shock velocity is measured in the frame of the unshocked ejecta ahead of it. (Truelove & Mckee 1999)

pressure is still high in the inner shell, the shell continues to expand with the time dependency of $R_s \propto t^{2/7}$ (McKee & Ostriker 1977), and is referred to as the pressure-driven snowplow (PDS) stage. After the PDS stage, the pressure becomes consistent with that of the ISM and also referred to as the momentum-conserving snowplow (MCS) stage (Cioffi et al. 1988). In this stage, the shock expands remaining its momentum ($M_s v_s$ = constant), where M_s is the mass of the shell. The shock velocity and its radius is described as $v_s \propto t^{-3/4}$ and $R_s \propto t^{1/4}$.

2.2.2 Classification of Supernova Remnants

SNRs are classified by the structure of emission in the radio and X-ray band. The X-ray contains the thermal emission from plasmas and the non-thermal emission by the synchrotron radiation, while the radio emission is the result of the non-thermal emission by synchrotron radiation. Main remnant type is shell-like SNR that has the shell-like emissions in both the radio and X-ray band as shown in Figure 2.5. Plerionic SNRs shown in Figure 2.6 have the centre-filled structure of the radio and X-ray emissions, where the X-ray comes from a neutron star or its wind nebula. Figure 2.7 shows a composite SNR whose emissions in radio and X-ray have both characteristics of shell-like and plerionic SNRs.

SNRs having the centre-filled X-ray emission with the radio shell are categorised into the mixed-morphology (MM) SNRs (Rho & Petre 1998) shown in Figure 2.8. Two formation scenarios are suggested for the MM-SNR. One is the evaporation model that suggests that SNRs have a clumpy gas and evaporates. The other model describes the thermal conduction between the plasma and its ambient gas with a low temperature such as for a molecular cloud.

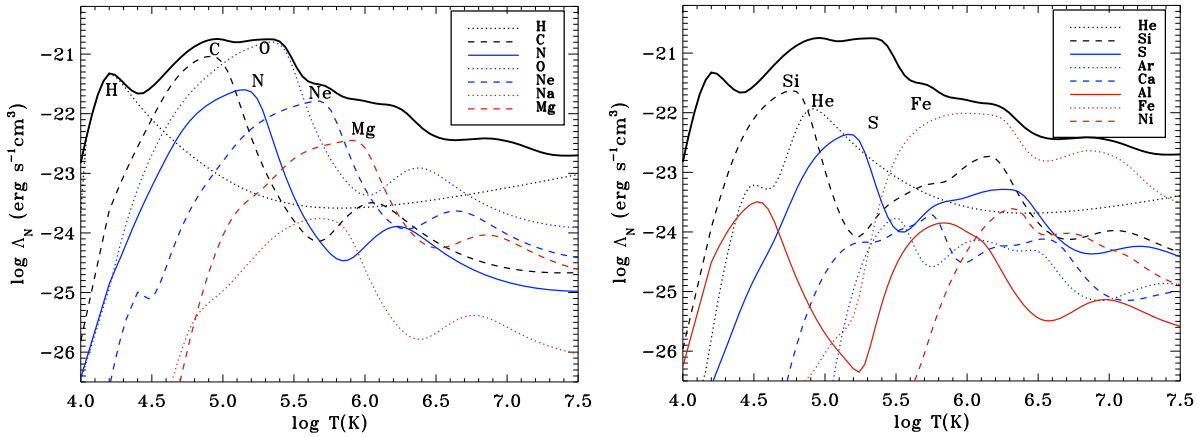

Figure 2.4: Contributions of different elements to the cooling curve are given. Each of the plots shows a different set of elements. Important peaks are labelled with the name of the element. The total cooling curve (black solid line) is an addition of the individual elemental contributions. (Schure et al. 2009)

Most of the MM-SNRs are likely to interact with a dense interstellar medium (ISM) as indicated by detections of CO emissions or OH masers at 1720 MHz in some cases (e.g. Tatematsu et al. 1990, Rho & Petre 1998, Yusef-Zadeh et al. 2003). Some of them are also associated with GeV gamma-ray emissions (e.g. Acero 2016), supporting the presence of a dense ISM in the vicinity of the remnants if the origin of the gamma-ray is π^0 decays. Such a dense surrounding environment probably plays an important role in the formation of MM-SNRs, but detailed physical processes are still under debate (e.g. White & Long 1991, Cox et al. 1999).

2.3 Thermal Radiation Processes

Thermal X-ray radiation is emitted from the optically thin hot plasma, which consists of the shocked ejecta and ISM in SNRs. In this section, we explain the physical process of the continuum and line emission from SNRs.

2.3.1 Continuum emission

The continuum component of X-ray emissions from plasma in SNRs consists of the bremsstrahlung radiation, radiative recombination continuum (RRC), and two-photon emission and are caused by free-free, free-bound, and bound-bound transitions of electrons, respectively. Figure 2.9 shows the emissivity produced by three processes (Vink 2012).

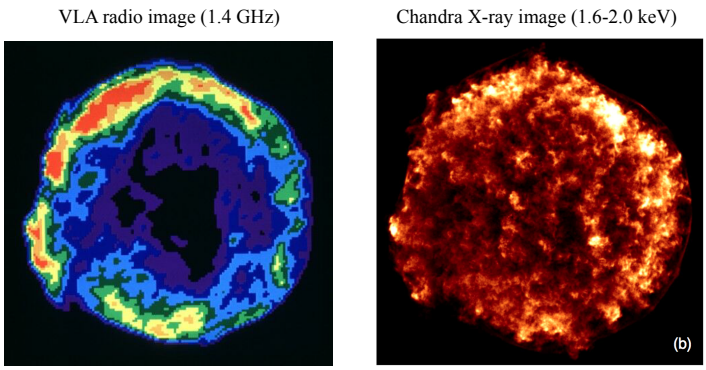

Figure 2.5: Radio (left) and X-ray (right) images of the shell-like SNR, Tyhco. 1.4 GHz radio continuum image from with the Very Large Array (VLA; Credit Radio: NSF/NRAO/VLA). X-ray image in 1.6–2.0 keV with Chandra (Lu et al. 2015).

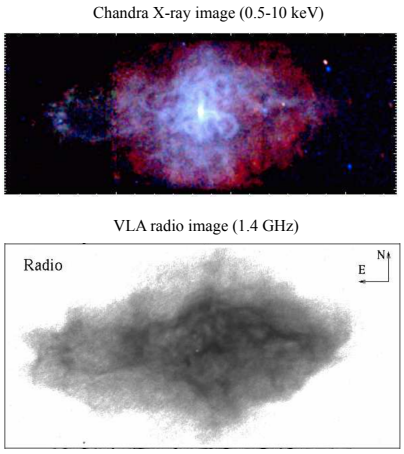

Figure 2.6: Radio (bottom) and X-ray (upper) images of the plerionic SNR, 3C 58. 1.4 GHz radio continuum image from with VLA. X-ray image in 0.5–10.0 keV with Chandra (Slane et al. 2004).

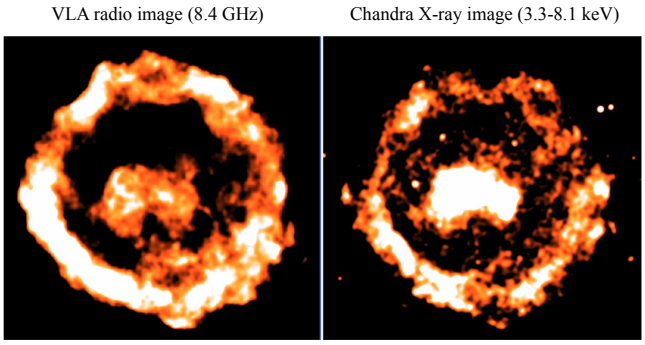

Figure 2.7: Radio (left) and X-ray (right) images of the composite SNR, G11.2-0.3. 8.4 GHz radio continuum image from with VLA. X-ray image in 3.3–8.1 keV with Chandra (Borkowski et al. 2016).

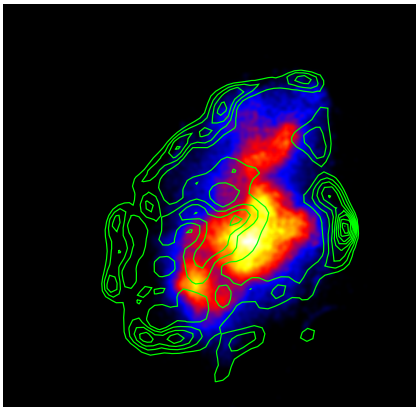

Figure 2.8: Radio (green contour) and X-ray (colore) images of the mixed-morphology SNR, W44. 1.5 GHz radio continuum image from with VLA. X-ray image in 0.3–10.0 keV with Suzaku (Matsumura 2018).

Free-free emission (Bremsstrahlung)

Bremsstrahlung or free-free radiation is caused by the emission of photons by accelerating charged particles in a Coulomb force field environment. The emissivity of the optically-thin thermal bremsstrahlung is given as,

$$\frac{dW}{dVdtd\nu} = \frac{2\pi e^6 Z^2}{3m_e c^3} n_e n_i T^{-\frac{1}{2}} \left(\frac{2\pi}{3m_e}\right)^{\frac{1}{2}} \exp\left(-\frac{h\nu}{kT}\right) \overline{g}_{ff}, \tag{2.15}$$

where e, Z, m_e, c, n_e, n_i, and $\overline{g}_{ff}$ are charge unit, atomic number, electron mass, light speed, electron density, ion density, and the velocity averaged Gaunt factor. The Gaunt factor is a certain function of the electron temperature and the frequency of the emission, reviewed by Bressaard & van de Hulst (1962), Karzas & Latter (1961). In the thermal plasma emitting X-ray, the Gaunt factor is given as

$$\overline{g}_{ff}(T,\nu) = \left(\frac{3}{\pi}\frac{kT_e}{h\nu}\right)^{-\frac{1}{2}}. \tag{2.16}$$

We obtain the total power per unit volume emitted by thermal bremsstrahlung by integrating equation (2.15) over frequency as

$$\frac{dW}{dVdt} = \frac{2^5\pi e^6 Z^2}{3hm_e c^3} n_e n_i \left(\frac{2\pi kT}{3m_e}\right)^{\frac{1}{2}} \overline{g}_B, \tag{2.17}$$

$$= 1.4\times10^{-27} Z^2 n_e n_i T^{\frac{1}{2}} \overline{g}_B \text{ erg s}^{-1} \text{ cm}^{-3}. \tag{2.18}$$

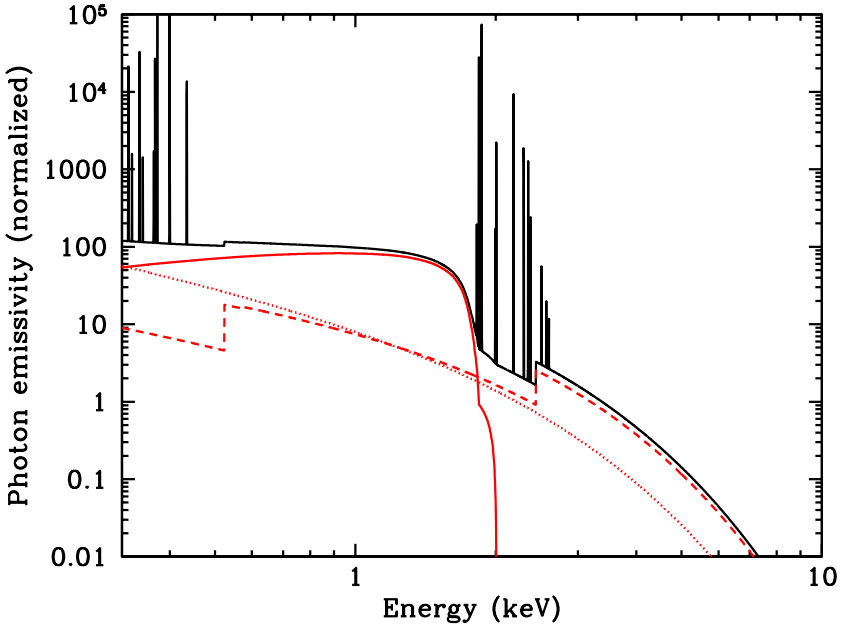

Figure 2.9: The emissivity of a pure silicon plasma out of ionisation equilibrium ($kT_e = 1$ keV, $n_e t = 5 \times 10^{10}$ cm^{-3}s). Shown are the contributions of two-photon emission (red solid line), free-bound continuum (red dashed line) and bremsstrahlung (free-free emission, red dotted line). The total emissivity is also shown, including Si-L and Si-K shell line emission (based on calculations made with the spectral code SPEX, Kaastra et al., 2003). (Vink 2012)

where $\overline{g}_B$ is a frequency average of the velocity averaged Gaunt factor, which is ~ 1.3 with the electron temperature of 3×10^6 K (Itoh et al. 2002). Because the power of the bremsstrahlung emission depends on the electron temperature and density of electrons and ions, we can estimate them from the intensity and shape of the thermal continuum spectrum.

Free-bound emission (Radiative recombination continuum)

Photons, which is called as a free-bound emission or RRC, are emitted when free electrons recombine with ions. The spectra shape of the RRC is continuum because of the various electron energy. The K-shell edge energy of the RRC is the binding energy of the levels as shown in Figure 2.9. The emissivity of the RRC is described by

$$\varepsilon_{fb} = 4 n_e n_{i+1} h\nu \frac{h\nu - \chi_n}{kT_e} \left(\frac{1}{2\pi m_e kT_e} \right)^{\frac{1}{2}} \sigma_n^{rec}(h\nu - \chi_n) \exp\left(-\frac{h\nu - \chi_n}{kT_e} \right) \text{ ergs}^{-1}\text{cm}^{-3}\text{Hz}^{-1}, \quad (2.19)$$

where n_{i+1}, χ_n, and σ_n^{rec} are the density of an ion with charge $i+1$, the ionisation potential for an electron in level n, and the cross section of the recombination to the level n at given electron

energy, respectively. In this paper, we indicate the RRC emitted from electrons dropping into a bare ion and a H-like ion as "H-like RRC" and "He-like RRC". Their K-shell edge energy are summarised in Table 2.2.

Table 2.2: The energy edge of H-like and He-like RRC emissions.

Element	K-shell edge energy (keV)	
	H-like RRC	He-like RRC
Ne	1.362	1.196
Mg	1.958	1.763
Si	2.666	2.439
S	3.482	3.225
Ar	4.406	4.121
Ca	5.440	5.128
Fe	9.194	8.830

Bound-bound emission (two photon emission)

When a electron transits between two bound states where the direct transition is forbidden by a selection rule, it transits emitting two photons. Although the total energy of the two photons is consistent with the binding energy, the energy of each photon is not uniquely determined. Therefore, the two photon emission produces a continuum spectrum as shown in Figure 2.9.

2.3.2 Line emission

The line emission from the SNRs plasma results from collisional excitation of ions, which is dominated by electron-ion collisions. When an electron transits between two bounds with different energy levels, it emits a photon called as line emission or bound-bound emission. For a hydrogen atom or a H-like ion, the energy of a photon is

$$E_{bb} \sim Z^2 R_y \left(\frac{1}{n^2} - \frac{1}{n'^2} \right), \tag{2.20}$$

where Z, R_y, n, and n' are the atomic number, Rydberg constant (13.6 keV), principal quantum number before and after transition, respectively. The H-like transition is called as "Lyman series"; Lyα (H-like Kα, $2p \to 1s$), Lyβ (H-like Kβ, $3p \to 1s$), and Lyγ (H-like Kγ, $4p \to 1s$), and so on, where s and p mean azimuthal quantum numbers l are 0 and 1, respectively. In the case of He-like ion, we call Heα (He-like Kα, $2p \to 1s$), Heβ (He-like Kβ, $3p \to 1s$), and Heγ

(He-like Kγ, $4p \rightarrow 1s$). The line energies of the Lyman series and He-like ions emitted from major elements are summarized in Table 2.3.

Table 2.3: The line energies of K-shell transition lines from H-like and He-like ions.

Element	Line energy (keV)							
	H-like ion			He-like ion				
	Lyα	Lyβ	Lyγ	K$\alpha(r^*)$	K$\alpha(f^*)$	K$\alpha(i^*)$	Kβ	Kγ
C	367	436	459	308	299	304	355	371
N	500	593	625	431	420	426	498	522
O	654	774	817	574	561	569	666	698
Ne	1022	1211	1277	921	905	914	1073	1127
Mg	1472	1745	1840	1352	1330	1343	1579	1660
Si	2006	2377	2506	1865	1840	1854	2183	2294
S	2623	3107	3277	2461	2431	2447	2884	3033
Ar	3323	3936	4151	3140	3104	3124	3685	3875
Ca	4106	4864	5130	3908	3845	3892	4582	4819
Fe	6966	8266	8732	6702	6641	6670	7798	8217
Ni	8077	9590	10107	7806	7744	7766	9190	9680

* r, f, and i indicate resonance, forbidden, and inter-combination lines, respectively.

2.4 Ionisation state of thermal plasma

2.4.1 ionisation state

The plasma is divided into the ionising, recombining and collisional ionisation equilibrium (CIE) states based on the relation between the electron temperature and the ionisation temperature. The ionisation temperature T_Z is equivalent to the electron temperature T_e that would reproduce the observed ion fractions in a CIE state. Therefore, the electron temperature is equal to the ionisation temperature ($T_e = T_z$) in the CIE state. If the electron temperature is higher than the ionisation temperature ($T_e > T_z$), the plasma is in an ionising-dominant state called as a ionising plasma (IP). When the electron temperature is lower than the ionisation temperature ($T_e < T_z$), The recombining process dominates and is referred to as a recombining plasma (RP). The IP and RP are called as non-equilibrium ionisation (NEI) state, against the CIE state.

After the shock passage, electrons and ions are heated and are $\propto m_i v_s^2$. Due to the mass of the electron and ions ($m_p/m_e \sim 2000$), their temperatures are non-equilibrium ($T_p \sim 2000 T_e$) but thermalise by Coulomb collisions. The thermal equilibrium timescales of electron-proton and electron-electron interactions are described as follows:

$$\tau_{ep} = 3.1 \times 10^{11} \left(\frac{n_p}{1\ cm^{-3}}\right)^{-1} \left(\frac{kT}{1\ keV}\right)^{\frac{3}{2}} \left(\frac{ln\Lambda}{30.9}\right)\ \text{s}, \tag{2.21}$$

$$\tau_{ee} = 4.9 \times 10^{8} \left(\frac{n_e}{1\ cm^{-3}}\right)^{-1} \left(\frac{kT}{1\ keV}\right)^{\frac{3}{2}} \left(\frac{ln\Lambda}{30.9}\right)\ \text{s}, \tag{2.22}$$

where lnΛ is the Coulomb logarithm (Zel'dovich & Raizer 1966), whose typical value is ~ 30.9 in X-ray emitting plasma at $n_e = 1$ cm^{-3}.

On the other hand, the ionisation state is considered to be neutral after the shock. The ions are gradually ionised by collisions with free electrons until they reach the CIE state. The ionisation equilibrium timescale is indicated as

$$\begin{aligned} n_e \tau_{ion} &= \sum_{j=1}^{Z} (S_j + \alpha_j)^{-1} \\ &\approx [(S_j + \alpha_j)_{min|S_j - \alpha_j|}]^{-1} \\ &\approx 10^{12}\ \text{cm}^{-3}\ \text{s}, \end{aligned} \tag{2.23}$$

where S_j and α_j are the ionisation and recombination rates coefficient from the jth ion (Masai 1994). $(S_j + \alpha_j)_{min|S_j - \alpha_j|}$ is the absolute value of the diagonal element that gives the minimum difference between S_j and α_j.

2.4.2 ionisation state from observations

X-ray spectra consists of the continuum and line emissions, whose shape mainly depends on the electron temperature and ion fractions. Therefore, we can obtain the electron temperature and ion fractions from observed spectra. Because of the energy resolution of X-ray satellite detectors, the ion fraction is estimated from the centroid energy of an iron Kα line in X-ray spectra, as shown in Figure 2.10. In addition, the Fe Kα centroid energies of Type Ia SNRs are well reproduced using a one-dimensional hydrodynamics simulations by Martínez-Rodríguez et al. (2018). They developed a one-dimensional hydrodynamics code, the CR-hydro-NEI code, which includes the calculation of the cosmic-ray (CR) acceleration and the thermal X-ray emission, for production in evolving SNRs. Figure 2.11 shows their simulation results, which provides an excellent match to the observations of most Type Ia SNRs.

Since the ionisation timescale is generally $\sim 10^5$ yr that is longer than the age of SNRs

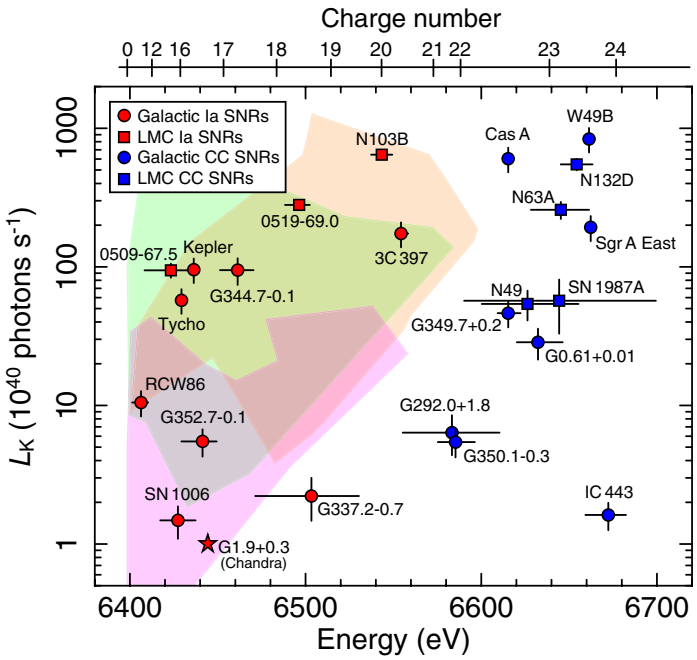

Figure 2.10: Centroid energies and line luminosities of Fe Kα emission from various SNRs in our Galaxy (circles) and the LMC (squares). The corresponding effective charge number is given above the panel. Red and blue represent Ia and CC SNRs or their candidates, respectively. The shaded regions represent the Fe Kα centroids and luminosities predicted by the theoretical Type Ia SNR models (DDTa: green, DDTg: magenta, PDD: orange; see right panel for details). (Yamaguchi et al. 2014a)

(10^2–10^4 yr), the plasma in SNRs is thought to be an ionising or in a CIE states. On the other hand, Kawasaki et al. (2002) detected an indication of the RP in an observation of IC 443. Ozawa et al. (2009) and Yamaguchi et al. (2009) discovered the RRC emission that is evidence of the RP, in MM SNRs: W48B and IC 443, respectively. However, the production mechanism of the RP is not entirely understood. We mention details of the RP in next section.

2.5 Recombining plasma in evolved SNR

The RP was first suggested by Kawasaki et al. (2002). They estimate the ionisation temperatures of Si and S from the line intensity ratio of H-like to He-like Kα. They report the ionisation temperatures of Si and S are significantly higher than the continuum temperature. The evidence of the RP, the RRC emission, was discovered in the SNRs; W48B (Ozawa et al. 2009) and IC 443 (Yamaguchi et al. 2009). Figure 2.12 shows the Suzaku X-ray spectra in which the RRC from Mg, Si, and S was detected. Recently, X-ray observations found RPs in many other MM SNRs (e.g., Ohnishi et al. 2011, Sawada & Koyama 2012, Uchida et al. 2012,

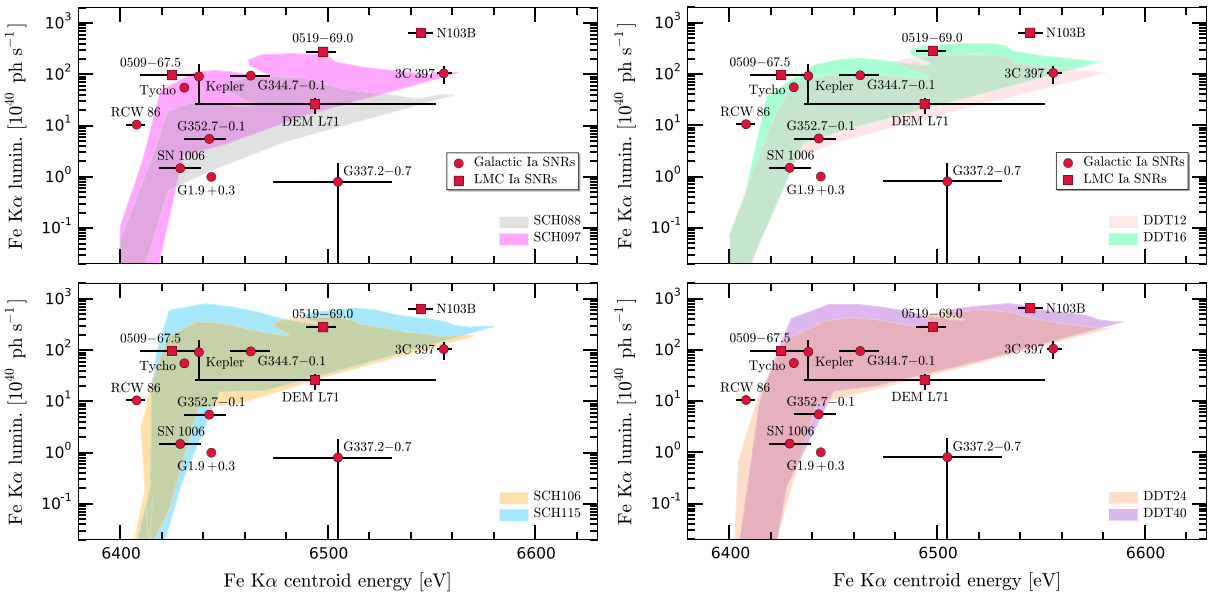

Figure 2.11: Centroid energies and line luminosities of Fe Kα emission from various Type Ia SNRs in our Galaxy (circles) and the LMC (squares). The shaded regions depict the Fe Kα centroids and luminosities predicted by our theoretical sub-M_{Ch} and M_{Ch} models with various uniform ISM densities (SCH088: grey; SCH097: magenta; SCH106: orange; SCH115: blue; DDT12: pink; DDT16: green; DDT24: light brown; DDT40: purple). (Martínez-Rodríguez et al. 2018)

Matsumura et al. 2017a). An RP indicates the unusual evolution of thermal plasmas, because the ionisation timescale is longer ($\sim 10^5$ yr) than the typical age of SNRs in the typical density of electrons (0.1–1 cm^{-3}) and an ionising plasma is expected in SNRs. The type of most SNRs in which the RP is discovered are thought to be CC SNe due to a low abundance of iron or the discovery of a compact object in some SNRs. In addition, a molecular cloud or atomic cloud associating SNRs have been discovered and their typical temperature is 10 K that is lower than that of plasma ($\sim 10^7$ K).

For the formation of the RPs in MM SNRs, two scenarios are mainly discussed, although the formation process of RPs are not completely understood yet. One of the proposed scenarios is rapid decreasing electron temperature (kT_e) via the rarefaction of the plasma when the shock breaks out of the dense circumstellar medium (CSM) into low density ISM (Itoh & Masai 1989, Yamaguchi et al. 2018). Because of the CC SNRs, the dense CSM is produced by the pre-SN wind and the expanding CSM creates the shell-like structure. When the shock wave of the SNR pass through the dense CSM, the electron temperature goes down by adiabatic expansion. The other is the thermal conduction scenario, in which the electron temperature decreases rapidly due to the interaction between the surrounding cold ISM and the hot plasmas (Kawasaki et al.

2002, Matsumura et al. 2017a). In order to investigate the origin of RPs, we need to deep analysis of RPs with the consideration of the ambient gas.

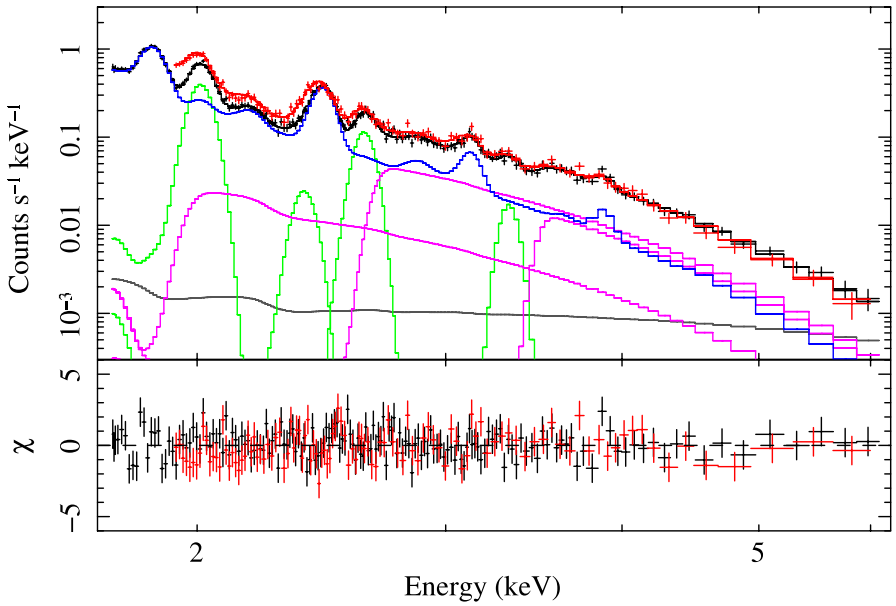

Figure 2.12: Suzaku XIS spectra (black and red) in the 1.75–6 keV band. Individual components of the best-fit model for the FI data are shown with solid coloured lines: blue, green, magenta and grey are the VAPEC, Gaussians (Si-Lyα, Si-Lyβ, S-Lyα, and Ar-Lyα), RRC components of H-like Mg, Si, and S, and CXB, respectively. The lower panel shows the residual from the best-fit model. (Yamaguchi et al. 2009)

Chapter 3

Instrumentation

For spectra analysis of observations, we utilise observational data obtained by the *Suzaku* orbiting X-ray observatory. In this chapter, we describe the properties of the *Suzaku* orbiting X-ray observatory and in-orbit performance.

3.1 Suzaku

the *Suzaku* orbiting X-ray observatory is the fifth Japanese X-ray astronomy satellite launched with the M-V rocket from JAXA Uchinoura Space Centre on July 10, 2005 (Mitsuda et al. 2007). It developed to observe celestial X-ray sources by the Institute of Space and Astronautical Science of the Japan Aerospace Exploration Agency (ISAS/JAXA) in collaboration with the Goddard Space Flight Centre of the National Aeronautics and Space Administration (GSFC/NASA) and other institutions. *Suzaku* was successfully put into a near circular orbit at 570 km altitude with an inclination angle of 31°. The orbital period was about 96 minutes. A schematic view of *Suzaku* is shown in figure 3.1. After long operations in a decade, *Suzaku* completed scientific observations in 2015 and is under operations in order to terminate radio wave transmissions.

Suzaku carries three types of scientific instrumentations which allows us to observe in a broad-band energy range from 0.2 to 600 keV. Figure 3.2 shows a side view of *Suzaku*. The spacecraft length is 6.5 m along the telescope axis after deployment of an extensible optical bench (EOB). First instrument is the X-ray Imaging Spectrometer (XIS) which consists of four charge coupled devices (CCDs) with an energy range of 0.2–12.0 keV (Koyama et al. 2007). Second is the Hard X-ray Detector (HXD) for extending the bandpass of the *Suzaku* observatory to much higher energies (Takahashi et al. 2007). The HXD is a non-imaging, collimation-type hard-X-ray instrument sensitive to photon of 10–600 keV (Kokubun et al. 2007). The last is the X-ray Spectrometer (XRS: X-ray micro-calorimeter) which was not operational due to liquid helium loss just after the launch (Kelley et al. 2007). Five sets of X-ray telescopes (XRTs) are

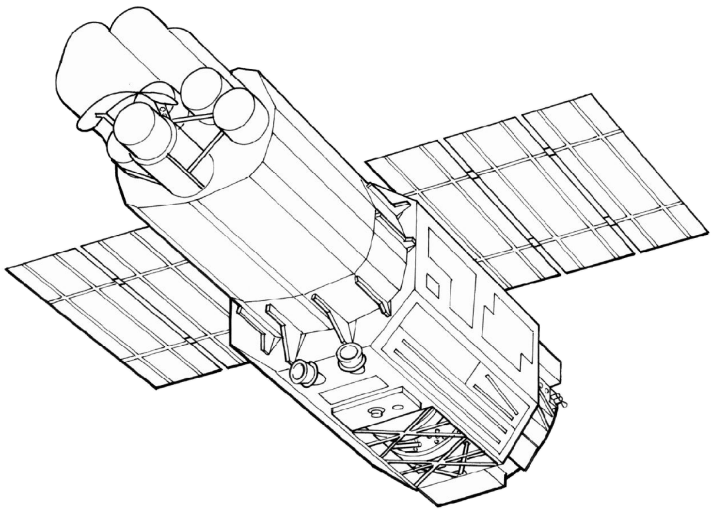

Figure 3.1: A schematic views of the *Suzaku* satellite in orbit (Mitsuda et al. 2007).

installed on the top of the EOB (Serlemitsos et al. 2007). The XIS and XRS are located in the focal plane of a dedicated XRT. Since data of the XIS are used in our study, we describe the detail of the XRT and XIS in the following sections. The HXD and XRS will not be discussed further.

3.2 X-ray telescope (XRT)

The X-ray telescopes (XRTs) are thin-foil-nested Wolter-I type telescopes developed by GSFC/NASA, Nagoya University, Tokyo Metropolitan University, and ISAS (Serlemitsos et al. 2007). Figure 3.3 shows the XRT-I1 module. In oder to avoid a stray light such as X-rays arriving from outside the field of view, a pre-collimator are installed on the top of each XRT. Basic parameters of the XRT are summarised in table 3.1. Due to very thin foils ($\sim$175 μm) of the reflectors and conical shape, XRTs provide a large aperture efficiency with a moderate imaging capability in the wide energy range of 0.2–12 keV.

Figure 3.4 shows the total effective area of the four XRT-I modules compared with that of XMM-Newton and Chandra. Though total weight of XRTs ($<$ 80 kg) is smaller than that of XMM-Newton mirrors ($\sim$1300 kg) and Chandra ($\sim$950 kg), the effective area of the four XRT-I modules at 7 keV is comparable. One of the XRTs is referred to as the XRT-S with a focal length of 4.50 m for the XRS. The other four XRTs are XRT-I0, I1, I2, I3 with a focal length of 4.75 m for the HXI. The XRT has a angular resolution of 2$'$ expressed in terms of the half-power diameter (HPD), which is defined as the diameter within which half of the focused

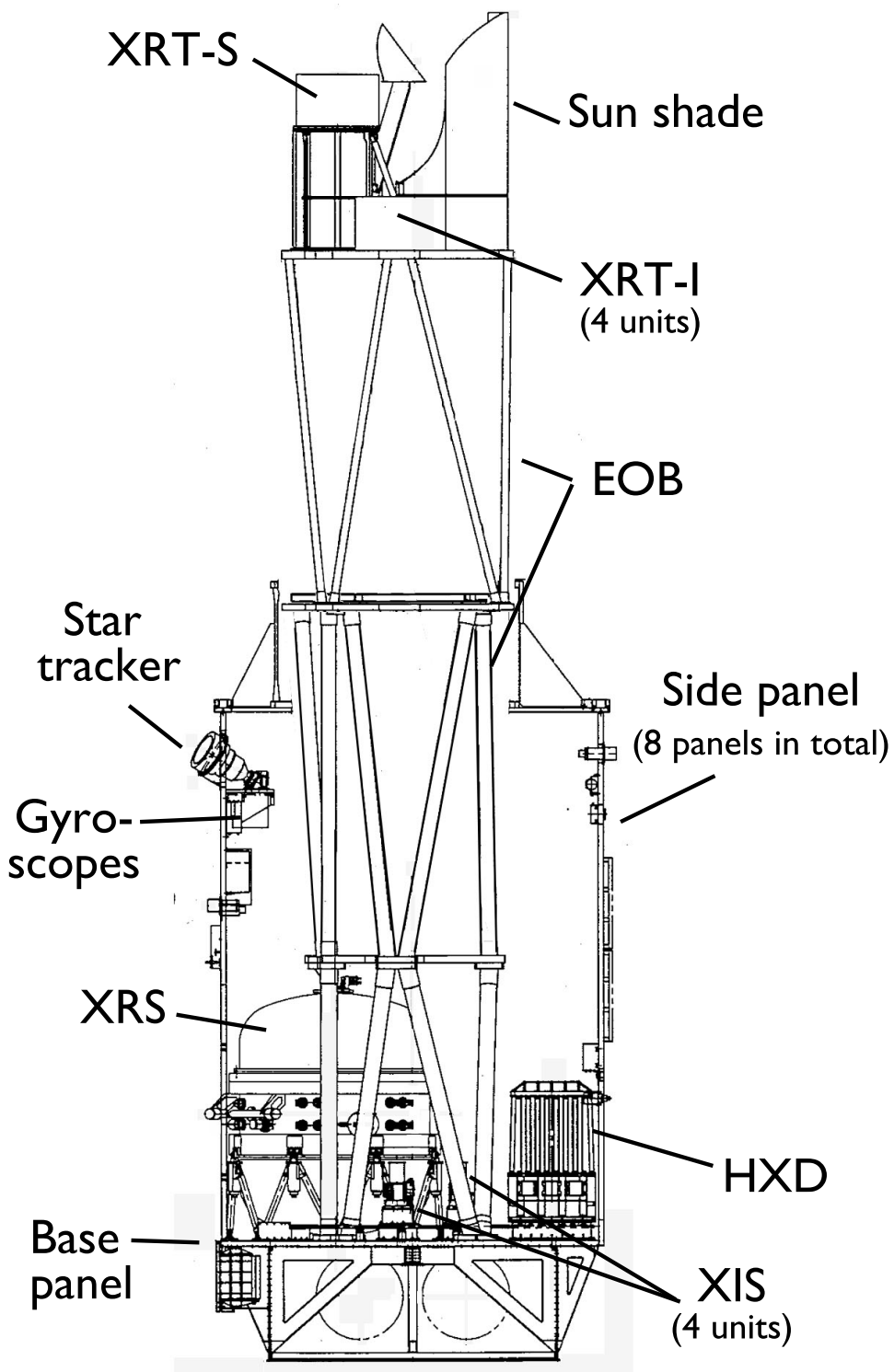

Figure 3.2: A side view of *Suzaku* with the internal structures after deployment of the EOB (Mitsuda et al. 2007). The spacecraft length is 6.5 m along the telescope axis after the EOB deployment.

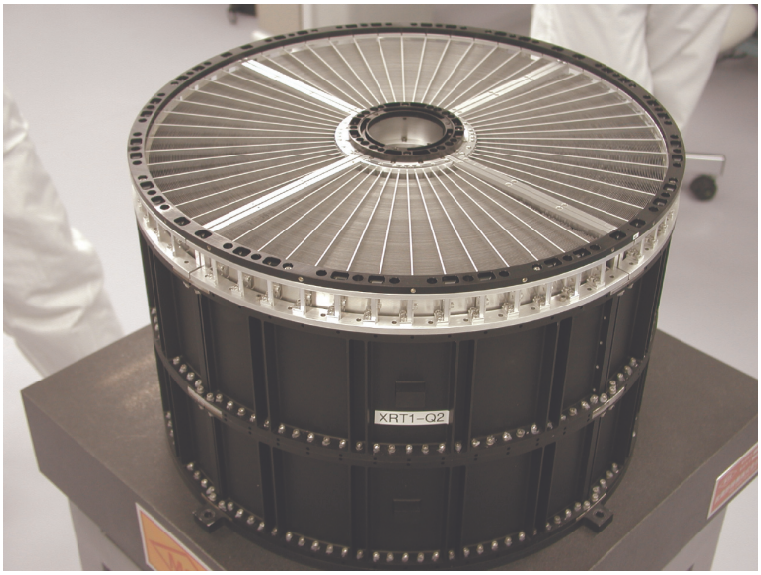

Figure 3.3: The module XRT-I1 (Serlemitsos et al. 2007). The thermal shield is not yet attached.

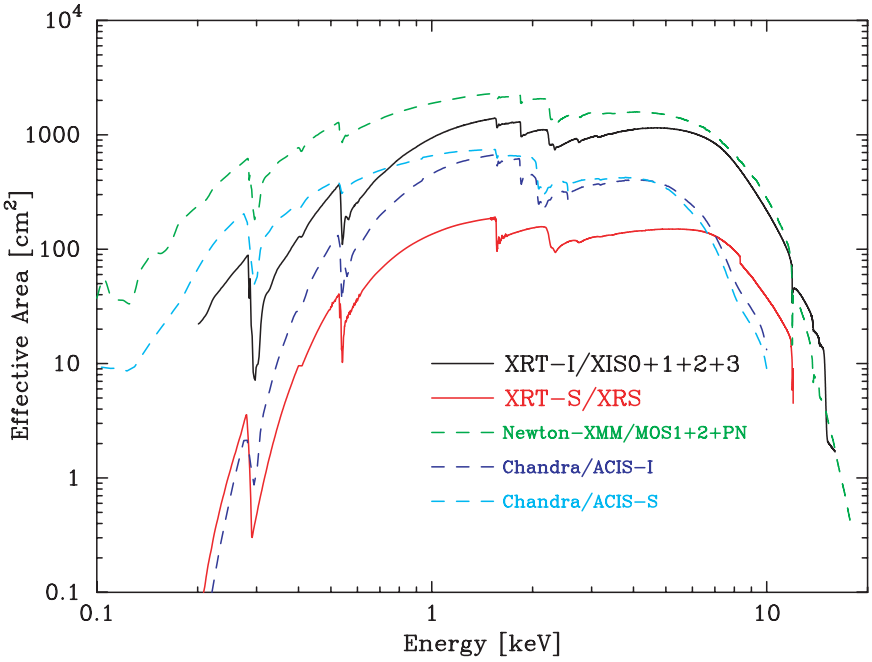

Figure 3.4: Total effective area of the four XRT-I modules compared with that of XMM-Newton and Chandra (Serlemitsos et al. 2007).

Table 3.1: Overview of the XRT

Focal length (XRT-S)	4.50 m
(XRT-I)	4.75 m
Weight	19.3 kg
Field of View	$20'$ at 1 keV
	$14'$ at 7 keV
Effective area	450 cm^2 at 1.5 keV
	250 cm^2 at 7.0 keV
Angular Resolution (HPD)	$2'$

X-ray is enclosed. The HPD is independent of the incident X-rays energy in 0.2–12.0 keV. The Point-Spread Function (PSF) and Encircle-Energy Fraction (EEF) of all the XRT-I modules are shown in figure 3.5. The HPD of the XRT-I0, I1, I2 and I3 is $1.'8$, $2.'3$, $2.'0$, and $2.'0$ at , respectively. These are significantly improved from ASCA ($\sim 3.'6$).

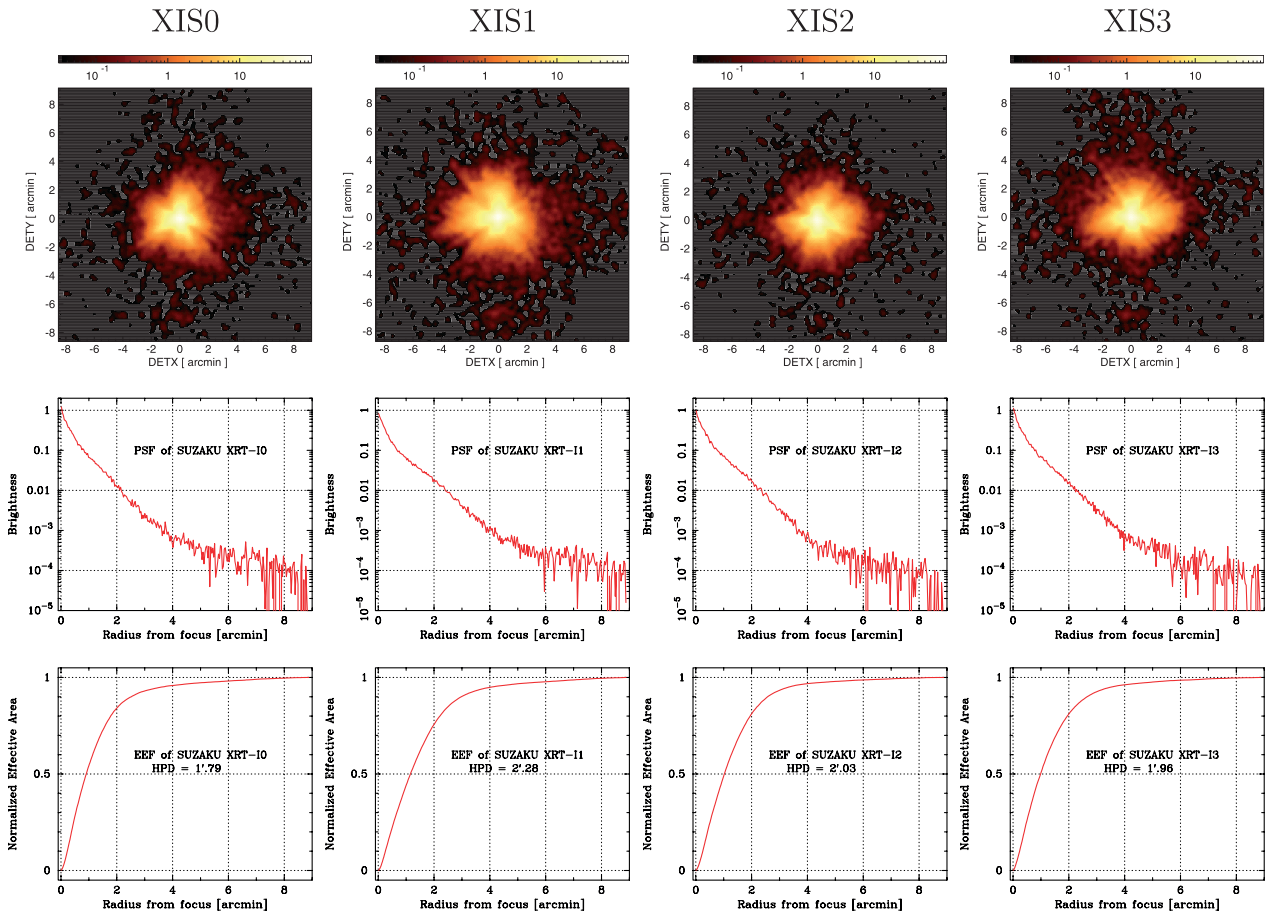

Figure 3.5: Images of the PSF and EEF of the four XRT-I modules in the focal plane (Serlemitsos et al. 2007). The EEF is normalised to unity at the edge of the CCD chip.

3.3 X-ray Imaging Spectrometer (XIS)

The X-ray Imaging Spectrometer (XIS) consists of four X-ray charge-coupled devices (CCDs), which is a MOS-type three-phase CCD operated in the frame transfer mode (Koyama et al. 2007). X-ray CCDs have been adopted as the principal detector of recent X-ray satellites such as XMM-Newton, Chandra and ASCA which is the first successful space flight used X-ray CCDs as photon counting and spectroscopic imagers. The digital electronics and a part of the sensor housing of the *Suzaku* XIS are developed by Kyoto University, Osaka University, Rikkyo University, Ehime University, and ISAS/JAXA and others are developed at the Massachusetts Institute of Technology. Figure 3.6 shows the XIS sensor and a cross section of it. Four CCDs are placed at the focal plane of a dedicated XRT-I. Three CCDs of XIS 0, 2 and 3 are front-illuminated (FI) devices with an energy range of 0.4–12.0 keV and XIS 1 is back-illuminated (BI) CCD with an energy range of 0.2–12.0 keV. Since the CCDs are sensitive to optical and UV light, the XIS has optical blocking filters (OBFs) which has a low transmission coefficient for optical light ($\leq 5 \times 10^5$), while the OBF is transparent to X-rays ($\geq 80\%$ above 0.7 keV).

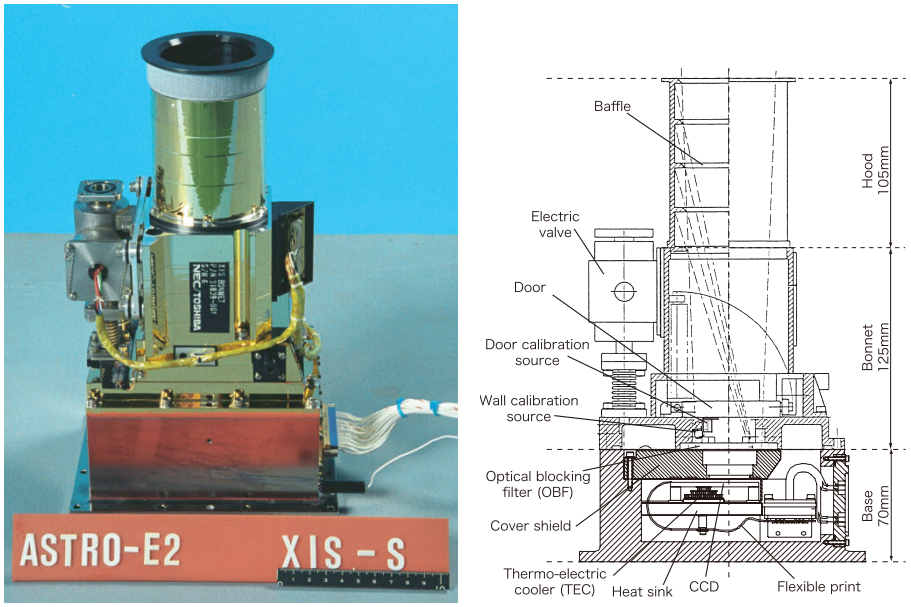

Figure 3.6: The XIS sensor (left) and schematic view of the XIS CCD (right) (Koyama et al. 2007).

The structure of a CCD chip installed in the base part of the XIS is shown in figure **??**. Basic parameters of the XIS are summarised in table 3.2. The size of an imaging area in the CCD chip is 25 mm × 25 mm, having 1024 × 1024 pixels, and covers an 17.′8 × 17.′8 region on the sky. The thickness of the BI CCD (∼42 μm) is thinner than that of the FI CCDs (∼65 μm). The CCDs are operated at a temperature of -90°C to reduce the effects of radiation

damage. Each CCD censer has a radiative source of ^{55}Fe for calibration of energy. The XIS 2 and a part of the XIS 0 have not been functional since anomalies occurred in 2006 November and in 2009 June, respectively. We therefore do not used the entire XIS 2 and segment A of XIS 0 for analysis.

Table 3.2: Overview of the XIS

Field of View	$18' \times 18'$
Energy range	0.2–12.0 keV
Format	1024 × 1024 pixels
Pixel size	24 μm × 24 μm
Effective area	330 cm^2 (FI), 370 cm^2 (BI) at 1.5 keV
	160 cm^2 (FI), 110 cm^2 (BI) at 8 keV
Energy resolution (FWHM)	∼130 eV at 5.9 keV

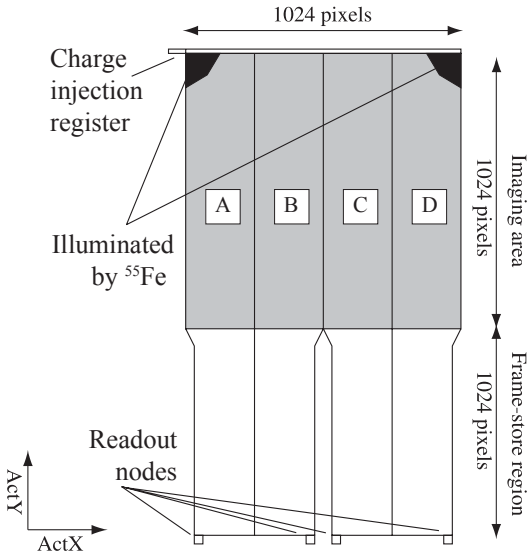

Figure 3.7: Schematic view of the XIS CCD (Koyama et al. 2007). Segments A, B, C, and D are CCDs with a dedicated read-out node.

The quantum efficiency (QE) of the BI CCD at high energy (> 4 keV) is lower than that of the FI CCDs because of these different thicknesses as shown in figure 3.8. XIS CCDs have the effective area of 160 cm^2 (FI) and 110 cm^2 (BI), hence the sum of the XIS CCDs is comparable to that of the XMM-Newton such as we described in previous section. The key feature of XIS is a high energy resolution defined as the full width at half maximum (FWHM) of the Gaussian function. The energy resolution achieves ∼130 eV at 5.9 keV for both of XIS-FI and XIS-BI.

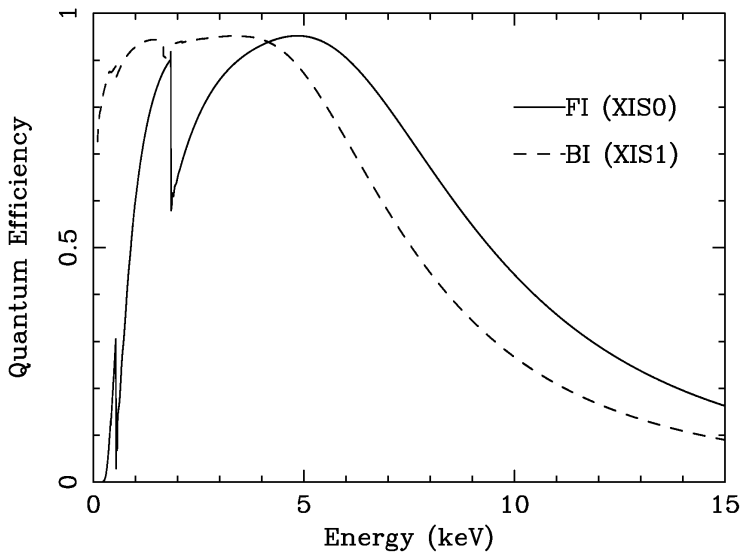

Figure 3.8: The QE calculated using best estimate values of the thickness of dead layers and depletion layer (Koyama et al. 2007).

The non-X-ray background (NXB) caused by high energy particle such as cosmic rays is detected in orbit. The NXB is fairly low for the XIS due to the low altitude of the orbit of *Suzaku*. Figure 3.9 which is the background counting rate of various X-ray satellite missions normalised with the effective area and the field of view. Comparing with other missions, the background level of the XIS-FI and BI is low and achieves a level next to ASCA SIS0.. The low background of the XIS enables us to achieve a high sensitivity for spatially extended sources.

The performance of the energy resolution is gradually degrading by radiation damage which is mostly caused by the charge transfer inefficiency. Figure 3.10 shows the time history of the energy resolution (FWHM) of Mn Kα from the calibration sources. The calibration results on the degradation of the energy resolution are reflected to the response matrix files (RMFs) Ishisaki et al. (2007).

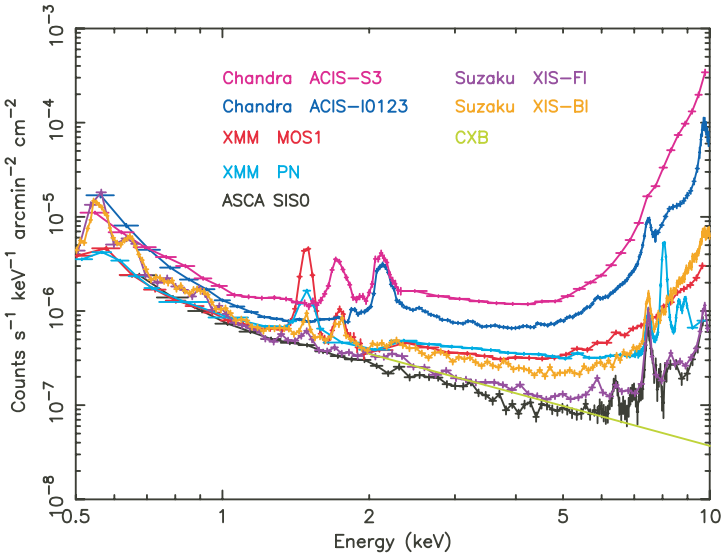

Figure 3.9: XIS background counting rate as a function of energy, where the background rate was normalised with the effective area and the field of view (Mitsuda et al. 2007).

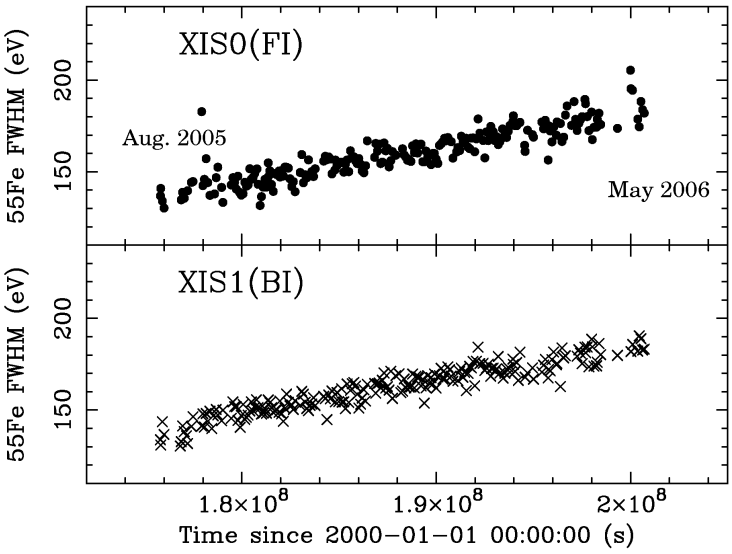

Figure 3.10: The time history of the energy resolution of Mn Kα line from the ^{55}Fe calibration sources for XIS FI (upper) and for XIS BI (lower) (Koyama et al. 2007).

Chapter 4

Suzaku X-ray observations of the MM SNR CTB 1

4.1 Overview of CTB 1

CTB 1 (G116.9+0.2) is one of the MM SNRs and it has a characteristic morphology as shown in figure 4.1. The remnant has a non-thermal radio shell, which breaks at the northeast quadrant (Landecker et al. 1982, Kothes et al. 2006), and its thermal X-rays extend outward from the break region (Craig & Hailey 1997). Optical emission lines also show an incomplete shell morphology similar to the radio shell (Fesen 1997). Yar-Uyaniker et al. (2004) argued that CTB 1 is located inside a large H I bubble, and that the radio shell is interacting with the edge of the bubble. No detections of gamma-ray emissions have been reported so far (e.g. Acero 2016). The distance to the remnant is highly uncertain in the range of 1.6–3.1 kpc (Craig & Hailey 1997, Yar-Uyaniker et al. 2004). The SNR age is estimated to be a few 10^4 years (Koo & Heiles 1991, Hailey & Craig 1994).

ASCA and Chandra observed CTB 1 and the nature of its thermal X-rays has been studied by Lazendic & Slane (2006) and by Pannuti et al. (2010). Their results show that a primary component is a thermal plasma in collisional ionisation equilibrium (CIE) with $kT_e \sim 0.2$–0.3 keV. However, they reported different minor components probably due to different analysis methods. Lazendic & Slane (2006) argued that another high-temperature plasma ($kT_e \sim$ 0.8 keV) is present inside the radio shell, whereas Pannuti et al. (2010) claimed a detection of a significant hard tail represented by a very high-temperature plasma ($kT_e \sim 3$ keV) or a power-law function with a photon index ($\Gamma \sim 2$–3) in both the inner radio shell and the breakout regions. Therefore, the nature of the X-ray plasmas is still unclear.

Here, we present new X-ray observations of CTB 1 with Suzaku/XIS (Mitsuda et al. 2007). Because of low instrumental background, the X-ray CCDs aboard Suzaku have very high sen-

Table 4.1: Observation log.

Target Name	Ods. ID	Obs. Date	l	b	Effective Exposure
CTB 1_SW	506034010	2011-12-29	116.°8913	0.°2952	29 ks
CTB 1_NE	506035010	2011-12-28	117.°1835	0.°1796	53 ks
GALACTIC PLANE 111 (BG1)	501100010	2006-06-06	111.°5011	1.°3149	72 ks
ANTICENTER2 (BG2)	503006010	2008-08-01	122.°9896	0.°0395	86 ks

sitivity to diffuse sources in the 0.6–5.0 keV band and are suitable to reveal a precise physical property of CTB 1. Throughout this paper, statistical errors are quoted at a 68% (1σ) confidence level.

4.2 Observation

We observed the southwest (SW) and northeast (NW) regions of CTB 1 with the X-ray Imaging Spectrometer (XIS: Koyama et al. 2007) aboard the Suzaku satellite. Table 4.1 shows the observation log and the total effective exposure time is $\sim$ 82 ks.

We also used nearby archival observations of GALACTIC PLANE 111 and ANTICENTER2 (hereafter BG1 and BG2, respectively) for evaluation of a background spectrum. As shown in table 4.1, the pointing direction of BG1 and BG2 are $\sim$ 5' away from CTB 1 in the Galactic latitude, but are on the Galactic plane. Therefore, an average spectrum of BG1 and BG2 likely represents a background spectrum at the coordinates of CTB 1. We also confirmed that no bright sources are included in the XIS field-of-views (FoVs) of BG1 and BG2.

We processed the above XIS data with the HEADAS software version 6.20 and the calibration database released in December 2016. We started with cleaned event lists produced by the standard pipeline process. The data taken by the 3×3 and 5×5 editing modes were merged. We discarded cumulative flickering pixels and pixels adjacent to the flickering pixels according to the noisy pixel maps provided by the XIS team[1]. Events below 0.6 keV were not used because contamination of O I Kα from the sunlit-Earth atmosphere in our observations was more severe than that shown in Sekiya et al. (2014), and spectral modelling below 0.6 keV is highly uncertain even when we add a Gaussian for O I Kα.

[1] `http://www.astro.isas.ac.jp/suzaku/analysis/xis/nxb_new2`

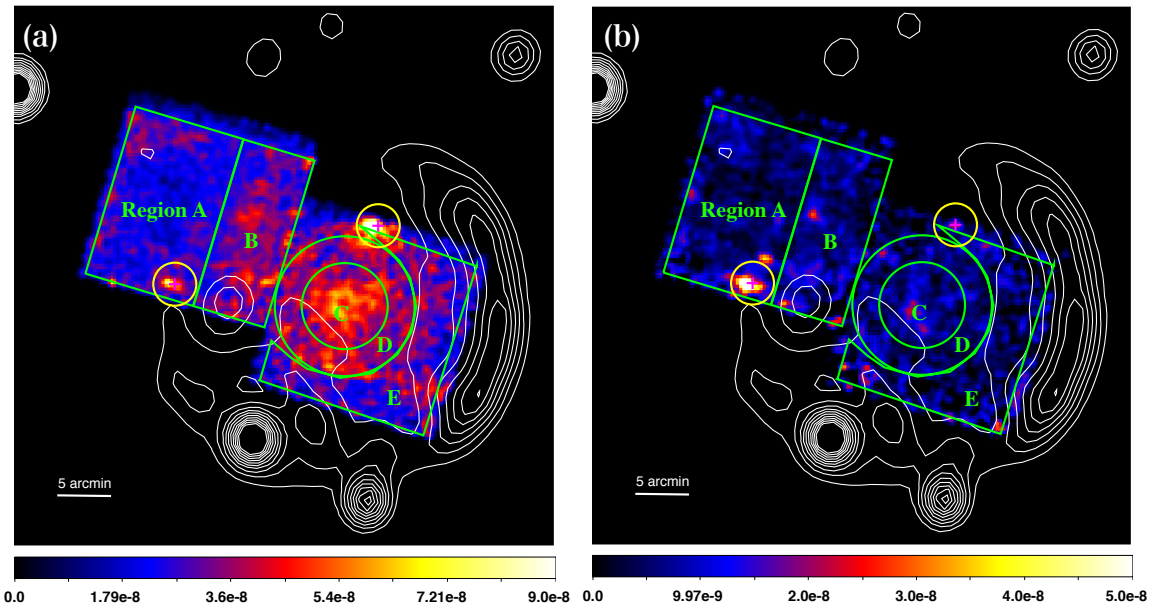

Figure 4.1: Exposure-corrected XIS images of CTB 1 in the (a) 0.6–2.0 keV band and (b) 2.0–5.0 keV band. The contours are a radio intensity map observed with the Canadian Galactic Plane Survey at 408 MHz Kothes et al. (2006). The magenta crosses with the yellow circles indicates bright point sources excluded in the spectral analyses. The green regions labeled with A, B, C, D, and E are spectral extraction regions (see section 4.3.2).

4.3 Analysis and Results

4.3.1 XIS Images of CTB 1

Exposure-corrected XIS images of CTB 1 in the 0.6–2.0 keV band and the 2.0–5.0 keV band are shown in Figure 4.1. The data of XIS 0, 1, and 3 were co-added, and the non X-ray backgrounds (NXBs) estimated by `xisnxbgen` Tawa et al. (2008) were subtracted. Soft X-ray emission in the 0.6–2.0 keV band is concentrated at the centre of the radio shell and extends toward the break of the radio shell as already reported by Lazendic & Slane (2006) and Pannuti et al. (2010). On the other hand, no remarkable diffuse structures are seen in the 2.0–5.0 keV band image.

We found two bright point sources at the southern edge of the NE observation and the northern edge of the SW observation. They were also identified in the 2XMMi catalog Watson & otheres (2009) and have fluxes of $\sim 4 \times 10^{-13}$ erg cm^{-2} s^{-1}. In the following spectral analyses, we excluded those point sources by the circular regions with 2 arcmin radii as shown in Figure 4.1.

4.3.2 Spectral modelling

In this section, we performed spectral modelling using the XSPEC version 12.9.1a. Spectra in 0.6–10.0 keV and 0.6–8.0 keV were extracted from the FI CCDs and BI CCD, respectively, and then subtracted corresponding NXB spectra created by `xisnxbgen` from them. We generated redistribution matrix files and auxiliary response files by `xisrmfgen` and `xissimarfgen` Ishisaki et al. (2007), respectively. The FI and BI CCDs spectra were simultaneously fitted.

Background Estimation

Using the BG1 and BG2 observations, we estimated background spectra before analysing the spectra of CTB 1. Figure 4.2 shows spectra extracted from the entire FoVs of those background observations. Weak emission lines were seen below 2 keV and continua dominate the spectra.

The X-ray background of the anti-Galactic centre direction likely consists of a superposition of unresolved stellar sources and the cosmic X-ray background (CXB) (e.g. Masui et al. 2009). The former component was approximated by two thin thermal plasma models in CIE, because individual stellar sources show a broad range of average temperatures Güdel & Nazé (2009). We used the APEC code with the AtomDB version 3.0.8 to reproduce the plasma spectra (Foster et al. 2012). The abundance (Z) were fixed to the solar value of Anders & Grevesse (1989) while the temperatures and the normalisations (N) were treated as free parameters. Those plasma models are subject to the absorption due to the foreground cold ISM, which was modelled by the PHABS code in XSPEC (hereafter PHABS1). The absorption column density ($N_{\rm H}$) of PHABS1 was allowed to vary. The CXB component was modelled by a power-law function (PL) with Γ of 1.4 and the 2–10 keV surface brightness of 6.9×10^{-15} erg cm^{-2} s^{-1} arcmin^{-2} according to Kushino et al. (2002). The CXB component is subject to the Galactic absorption (PHABS2) of which column density was estimated from the `nh` tool (Kalberla et al. 2005). In summary, our model is expressed as

$$\begin{aligned} &\mathrm{CONST} \times \mathrm{PHABS1} \times (\mathrm{APEC1} + \mathrm{APEC2}) \\ &\qquad + \mathrm{PHABS2} \times \mathrm{PL}, \end{aligned}$$

where CONST represents the difference in the surface brightness of the stellar component between BG1 and BG2. CONST of BG1 was fixed to 1.0, while that of BG2 was allowed to vary. The BG1 and BG2 spectra were simultaneity fitted with the above model. The model parameters are common between BG1 and BG2 except for CONST and PHABS2.

The best-fit model and parameters are shown in figure 4.2 and table 4.2, respectively. The model represents the spectra with $\chi^2_\nu = 1.21$. The obtained plasma temperatures of 0.21 keV and 0.96 keV agree with the typical temperature range of coronal X-rays (Johnstone & Güdel 2015). We found that the surface brightness of the stellar component is different by a factor of

2 between BG1 and BG2. CONST was fixed at 1.5 (the average of them) in following spectral analyses of CTB 1 because CTB 1 is located in the middle of BG1 and BG2. We confirmed that our results were not affected even when CONST was fixed to 1 or 2.

Table 4.2: Best-fit parameters of the background*

Model	Parameter (unit)	Value
CONST	factor of BG1	1.0 (fixed)
	factor of BG2	2.0±0.1
PHABS1	$N_{\rm H}$ (10^{21} cm^{-2})	5.8±0.5
APEC1	kT_e (keV)	$0.21^{+0.01}_{-0.02}$
	Z (solar)	1.0 (fixed)
	$N^{\dagger}$(10^{11} cm^{-5})	$1.6^{+0.9}_{-0.4}$
APEC2	kT_e (keV)	$0.96^{+0.05}_{-0.04}$
	Z (solar)	1.0 (fixed)
	$N^{\dagger}$(10^{11} cm^{-5})	0.16±0.02
PHABS2	$N_{\rm H}$ of BG1 (10^{21} cm^{-2})	7.63 (fixed)
	$N_{\rm H}$ of BG2 (10^{21} cm^{-2})	7.38 (fixed)
PL	Γ	1.4 (fixed)
	surface brightness‡	5.3 (fixed)
χ^2/d.o.f.		875.52/726

* Parameters are common between BG1 and BG2 except for CONST and PHABS2.

† Normalisation of the APEC component is $\frac{1}{4\pi D^2}\int n_e n_{\rm H} dV$, where D is the distance to the source, n_e and $n_{\rm H}$ are the electron and hydrogen densities, respectively, and V is the X-ray emitting volume.

‡ Unit of 10^{-15} erg cm^{-2} s^{-1} arcmin^{-2} in the 2.0–10.0 keV band.

Spectra of the NE region

Figure 4.3(a) shows spectra extracted from the entire FoV of the NE observation of CTB 1. Strong emission lines of highly ionised O, Ne, and Mg present below 2 keV while no remarkable features are seen above 2 keV.

According to Pannuti et al. (2010), we modelled those spectra by a single CIE plasma model with variable abundances of individual metals (the VAPEC model). Abundances of Ne, Mg,

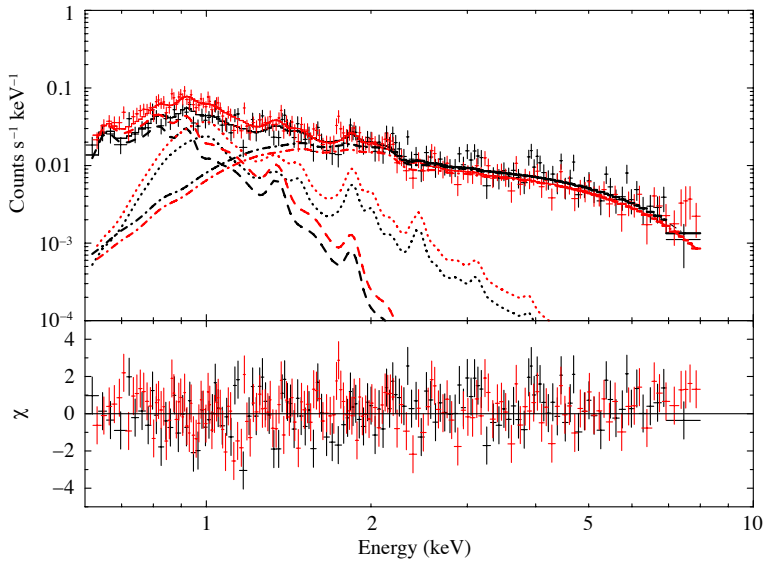

Figure 4.2: XIS 1 spectra of BG1 (black) and BG2 (red) after the NXB subtraction. The solid curves show the Galactic background model described in section 4.3.2. The dashed, dotted, and dash-dotted curves indicate the APEC1, the APEC2, and the CXB components, respectively.

Si, and Fe were allowed to vary. Abundances of S and Ni were linked to those of Si and Fe, respectively. If the O abundance was treated as a free parameter, it was not constrained. That is because the intensity of the radiative recombination continua from O is much higher than that of the bremsstrahlung from H for a plasma with $kT_e = 0.2$–0.3 keV. Therefore, we fixed the O abundance to the solar value. Other metals were fixed to the solar abundances. Absorption of the ISM was represented by the PHABS model. The background model constructed in the previous section is also included. In the background model, $N_{\rm H}$ of PHABS2 was fixed to 5.96×10^{21} cm^{-2} estimated by the `nh` tool. Hereafter, we refer to this model as NE Model1.

Table 4.3 shows the best-fit parameters and the residuals between the data and the NE Model1 are shown in figure 4.3(b). The model almost reproduces the observed spectra below 2 keV, but we found an excess of the data above 2 keV with $\chi^2_\nu = 1.50$. It suggests that an additional hard component is necessary as reported by Pannuti et al. (2010). We therefore tried two different models; one includes another APEC model (NE Model2) and the other includes a power-law function (NE Model3).

Table 4.3: Best-fit parameters of the NE spectra.

Model	Parameter (unit)	NE Model1	NE Model2	NE Model3
PHABS	$N_{\rm H}$ (10^{21}cm^{-2})	3.5±0.2	$2.4^{+0.2}_{-0.3}$	$2.1^{+0.3}_{-0.4}$
VAPEC	kT_e (keV)	$0.293^{+0.005}_{-0.004}$	$0.295^{+0.004}_{-0.003}$	0.30±0.05
	$Z_{\rm Ne}$ (solar)	1.30±0.06	$1.9^{+0.15}_{-0.08}$	$2.2^{+0.3}_{-0.2}$
	$Z_{\rm Mg}$ (solar)	0.98±0.09	1.6±0.1	$1.9^{+0.4}_{-0.3}$
	$Z_{\rm Si,\ S}$ (solar)	0.9±0.2	< 1.3	<1.6
	$Z_{\rm Fe,\ Ni}$ (solar)	0.14±0.02	0.22±0.02	0.23±0.03
	$Z_{\rm Others}$ (solar)	1.0 (fixed)	1.0 (fixed)	1.0 (fixed)
	N^*(10^{12} cm^{-5})	0.96±0.08	$0.5^{+0.07}_{-0.08}$	$0.40^{+0.10}_{-0.09}$
	$N*$ (10^{12} cm^{-5})	0.96±0.08	$0.5^{+0.07}_{-0.08}$	$0.40^{+0.10}_{-0.09}$
APEC	kT_e (keV)	-	$2.2^{+0.2}_{-0.3}$	-
	Z (solar)	-	< 0.031	-
	$N*$ (10^{12} cm^{-5})	-	$0.097^{+0.013}_{-0.008}$	-
PL	Γ	-	-	2.7±0.2
	surface brightness†	-	-	1.2±0.2
χ^2/d.o.f.		735.97/492	586.46/489	585.25/490

* Normalisation of the APEC component is $\frac{1}{4\pi D^2}\int n_e n_{\rm H} dV$, where D is the distance to the source, n_e and $n_{\rm H}$ are the electron and hydrogen densities, respectively, and V is the X-ray emitting volume.
† Unit of 10^{-15} erg cm^{-2} s^{-1} arcmin^{-2} in the 2.0–10.0 keV band.

In the NE Model2, the temperature, the normalisation, and the abundance relative to the solar values in the APEC were allowed to vary. The resultant best-fit parameters and residuals are shown in table 4.3 and figure 4.3(c), respectively. The fit statistic was remarkably reduced to $\chi^2_\nu = 1.20$. The parameters of the VAPEC component in the NE Model2 was almost consistent with those in the NE Model1. The APEC component shows kT_e of 2.2 keV and the abundance of < 0.031 solar. Such a high temperature plasma has been observed only in young supernova remnants. Moreover, the very low abundance does not agree with the abundance of the ejecta nor the ISM. We thus consider that the NE Model2 is physically unreasonable.

Table 4.3 and Figure 4.3(d) show the best-fit parameters and residuals of the NE Model3, respectively. The χ^2_ν of this model is the lowest (1.19). The absorption column density and the metal abundances were slightly changed from the NE Model1. The photon index Γ of the PL component is 2.7, and the surface brightness in the 2–10 keV band is lower than that of the CXB component by a factor of ~ 5. We consider that the NE Model3 is the best representative of the spectra.

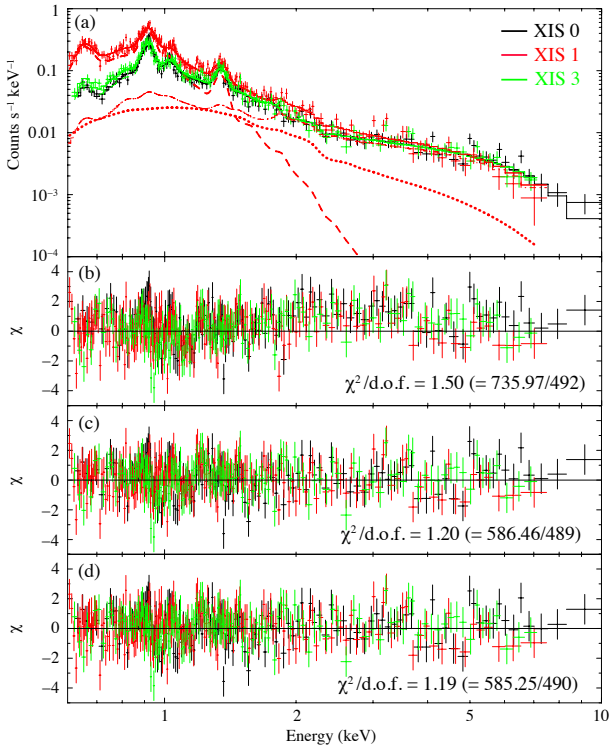

Figure 4.3: Top panel (a) shows spectra of the NE observation taken by the XIS 0 (black), 1 (red) and 3 (green). The solid curves are the NE Model3. The dashed, dotted, and dash-dotted curves represent the VAPEC, the PL, and the background components of XIS 1, respectively. The lower three panels show the residuals of the data compared to the NE Model1(b), the NE Model2 (c) and the NE Model3 (d).

Spectra of the SW region

Spectra extracted from the entire FoV of the SW observation of CTB 1 are shown in Figure 4.4(a). They are similar to the NE spectra, but have hump-like structures in the 1.1–1.7 keV band.

At first, we fitted the SW spectra with the same model as the NE Model3 (hereafter SW Model1). For the CXB component, we estimated the absorption column density of 6.35×10^{21} cm^{-2} from the `nh` tool. The best-fit parameters and the residuals are shown in table 4.4 and figure 4.4(b), respectively. The fit statistic χ^2_ν is 1.52. Sawtooth like residuals are shown around $\sim$ 1.23 keV and $\sim$ 1.45 keV. These energies correspond to the centroid energies of Fe L lines (e.g., Fe XXI 1s2 2s1 2p2 4s1$\rightarrow$1s2 2s1 2p3 and Fe XXI 1s2 2s2 2p1 5d1$\rightarrow$1s2 2s2 2p2), but these emissions are not strong in a plasma with kT_e of $\sim$ 0.3 keV. In order to improve the residuals, we tried to add another plasma component with a high kT_e because these Fe L lines have a peak at $kT_e \sim 0.9$ keV, but a suitable model could not be found.

Table 4.4: Best-fit parameters of the SW spectra.

Model	Parameter (unit)	SW Model1	SW Model2
PHABS	$N_{\rm H}$ (10^{21}cm^{-2})	2.9±0.4	4.5±0.2
VAPEC	kT_e (keV)	$0.298^{+0.008}_{-0.007}$	$0.186^{+0.005}_{-0.004}$
/VRNEI	$kT_{\rm init}$ (keV)	-	3.0 (fixed)
	$Z_{\rm Ne}$ (solar)	$2.0^{+0.4}_{-0.3}$	2.9±0.3
	$Z_{\rm Mg}$ (solar)	$1.8^{+0.5}_{-0.4}$	1.0±0.2
	$Z_{\rm Si,\ S}$ (solar)	<2.6	0.4±0.2
	$Z_{\rm Fe,\ Ni}$ (solar)	$0.43^{+0.07}_{-0.06}$	$2.1^{+0.3}_{-0.2}$
	$Z_{\rm Others}$ (solar)	1.0 (fixed)	1.0 (fixed)
	N^*(10^{12} cm^{-5})	$0.6^{+0.2}_{-0.1}$	$3.0^{+0.5}_{-0.4}$
	n_et (10^{11}s cm^{-3})	-	9.3±0.4
PL	Γ	3.5±0.1	2.2±0.3
	surface brightness†	$1.6^{+0.2}_{-0.1}$	$1.7^{+0.3}_{-0.2}$
χ^2/d.o.f.		572.58/377	443.43/376

* Normalisation of the APEC component is $\frac{1}{4\pi D^2}\int n_e n_{\rm H} dV$, where D is the distance to the source, n_e and $n_{\rm H}$ are the electron and hydrogen densities, respectively, and V is the X-ray emitting volume.
† Unit of 10^{-15} erg cm^{-2} s^{-1} arcmin^{-2} in the 2.0–10.0 keV band.

Because of a lack of radiative recombination continua (RRCs), sawtooth like residuals are often found in MM SNRs with RPs (e.g. Yamaguchi et al. 2009). The residuals around ~ 1.23 keV and ~ 1.45 keV indicate the excess of RRCs of He-like and H-like Ne, which are clear evidence of an RP. We added two REDGE models to the SW Model1 for investigation of this hypothesis. The result of the spectra fitting is shown in Figure 4.5. We confirmed that the fit was significantly improved and the electron temperature of the REDGE models is $0.13^{+0.04}_{-0.03}$ keV. The best-fit energies of the REDGE models are 1.20±0.02 keV and $1.34^{+0.04}_{-0.03}$ keV, which are consistent with the edge energies of He-like and H-like Ne (1.196 keV and 1.362 keV), respectively.

In order to apply an RP model to the full-band spectra, we used the VRNEI model, which takes into account ion fractions and ionisation timescales of all elements in the recombination-dominant state. We therefore replace the VAPEC model to the VRNEI model and refer to this model as SW Model2. The VRNEI model calculates the spectrum of a non-equilibrium ionisation plasma after a rapid transition of the electron temperature from $kT_{\rm init}$ to kT_e with a recombining timescale (n_et). Since the initial temperature $kT_{\rm init}$ was not well constrained

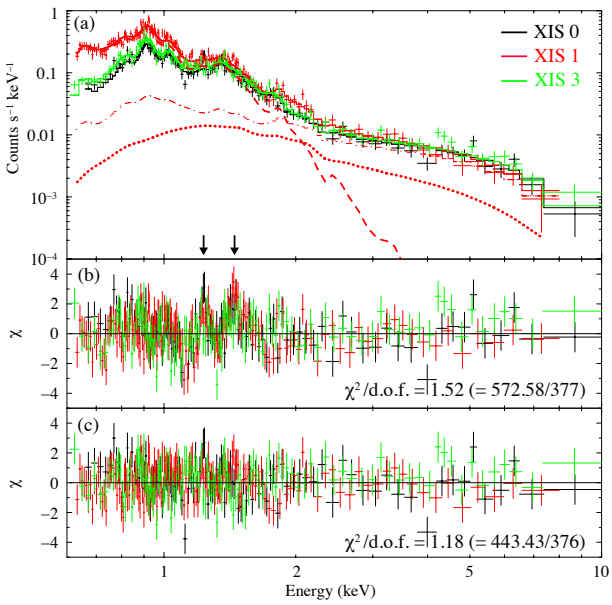

Figure 4.4: Top panel (a) shows spectra of the SW observation taken by the XIS 0 (black), 1 (red) and 3 (green). The solid curves are the SW Model2. The dashed, dotted, and dash-dotted curves represent the VRNEI, the PL, and the background components of XIS 1, respectively. The lower two panels show the residuals of the data compared to the SW Model1 (b), the SW Model2 (c). The two arrows point at 1.23 keV and 1.45 keV, respectively.

in our data, we fixed it to 3 keV, in which most Ne and Mg ions become bare nuclei. The best-fit parameters and the residuals are shown in table 4.4 and figure 4.4(c), respectively. No remarkable residuals are seen in the SW Model2, and the fit statistic is significantly improved to $\chi^2_\nu = 1.18$. The obtained $n_e t = 9.3 \times 10^{11}$ s cm^{-3} indicates that the plasma in the SW region is indeed an RP.

Spatially resolved spectra

We found that the plasma in the SW region is in the recombining phase, while that in the NE region is CIE state. To investigate more detailed spatial variation of the plasma properties, we divided the FoVs into five regions (A, B, C, D and E) as shown in figure 4.1 according to the 0.6–2.0 keV morphology.

Since the regions A and B are included in the NE observation, we fitted their spectra with the NE Model3. On the other hand, we applied the SW Model2 to regions C, D, and E, which are included in the SW observation. Since the non-functioning segment of XIS 0 occupies a large area in the region E, we did not use the XIS 0 spectrum extracted from the region E. We show the best-fit parameters and the fitted spectra in table 4.5 and figure 4.6, respectively. All the spectra are well reproduced by the models. The photon index in the region E is fixed

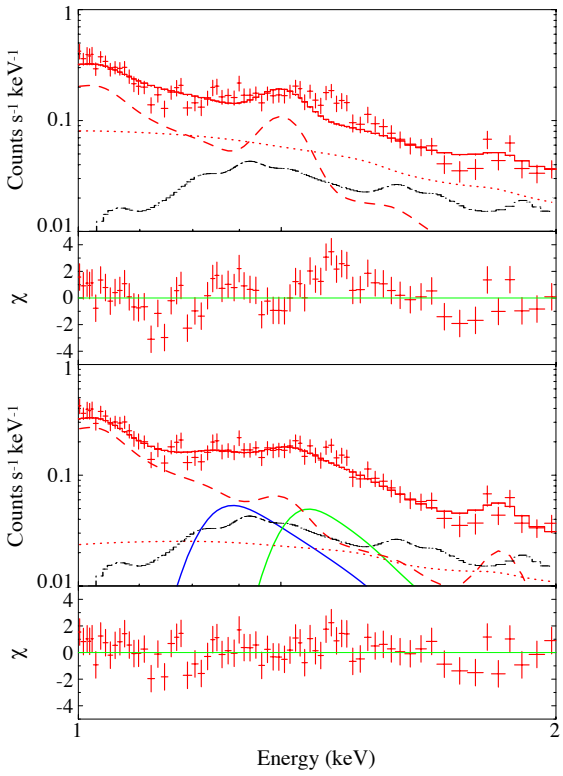

Figure 4.5: Top and third panels show spectra (red crosses) of the SW observation taken by XIS 1 with the best-fit models (red solid lines). In the top panel, the model consists of the VAPEC (red dashed), PL (red dotted) and background (black dashed). In the third panel, the model is same as that in the top panel but it additionally includes two REDGE components with the edge energies of 1.189 keV (blue solid) and 1.34 keV (green solid). Second and the lower panels show the residuals of the data compared to the models.

at 2.2, which is the best-fit value of the entire SW region, because that was not constrained in the fitting. We found significant spatial variations in $N_{\rm H}$, kT_e, the metal abundances, and $n_e t$.

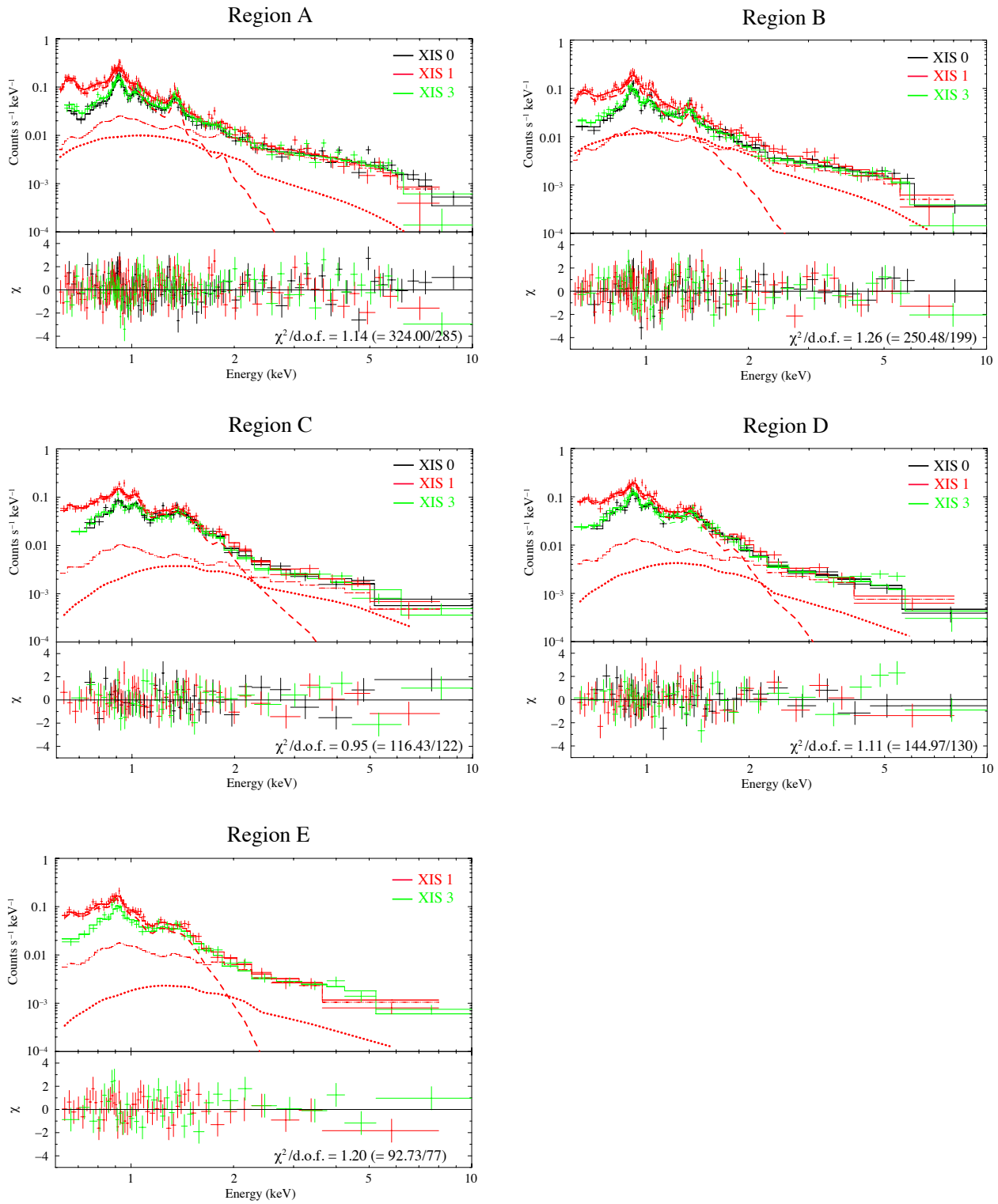

Figure 4.6: Each panel shows spectra extracted from each region taken by the XIS 0 (black), 1 (red) and 3 (green) and residuals from the best-fit models. The solid curves are the best-fit model. The dashed, dotted, and dash-dotted curves represent the VAPEC (regions A and B)/VRNEI (regions C, D and E), the PL, and the background components of XIS 1, respectively.

Table 4.5: Best-fit parameters of spectra for the spatial resolved analysis.

Model	Parameter (unit)	region A	region B	region C	region D	region E
Absorption	$N_{\rm H}$ (10^{21}cm^{-2})	2.3±0.4	2.2±0.5	$4.4^{+0.4}_{-0.5}$	4.4±0.4	$4.3^{+0.5}_{-0.6}$
VAPEC	kT_e (keV)	$0.288^{+0.007}_{-0.006}$	$0.306^{+0.010}_{-0.009}$	$0.193^{+0.010}_{-0.009}$	0.20±0.01	0.155±0.009
/VRNEI	$kT_{\rm init}$ (keV)	-	-	3.0 (fixed)	3.0 (fixed)	3.0 (fixed)
	$Z_{\rm Ne}$ (solar)	$1.9^{+0.3}_{-0.2}$	$2.4^{+0.5}_{-0.4}$	$2.9^{+0.6}_{-0.5}$	$2.7^{+0.5}_{-0.4}$	$3.2^{+0.9}_{-0.6}$
	$Z_{\rm Mg}$ (solar)	$1.8^{+0.5}_{-0.3}$	$1.6^{+0.5}_{-0.4}$	0.8±0.3	$1.3^{+0.4}_{-0.3}$	<1.7
	$Z_{\rm Si,\ S}$ (solar)	<2.7	<2.9	0.4±0.2	$0.6^{+0.4}_{-0.5}$	<4.0
	$Z_{\rm Fe,\ Ni}$ (solar)	0.20±0.03	$0.30^{+0.06}_{-0.05}$	1.4±0.5	$1.2^{+0.6}_{-0.4}$	>2.4
	$Z_{\rm Others}$ (solar)	1.0 (fixed)	1.0 (fixed)	1.0 (fixed)	1.0 (fixed)	1.0 (fixed)
	N^*(10^{12} cm^{-5})	0.5±0.1	$0.4^{+0.2}_{-0.1}$	3.3±0.8	$2.7^{+0.8}_{-0.7}$	$2.6^{+1.1}_{-0.8}$
	n_et (10^{11}s cm^{-3})	-	-	7.0±0.5	$9.9^{+0.8}_{-0.6}$	10.5±1.0
PL	Γ	2.7±0.4	2.6±0.2	$1.9^{+0.5}_{-0.6}$	2.6±0.7	2.2 (fixed)
	surface brightness†	0.8±0.2	1.9±0.3	2.5±0.6	1.1±0.3	0.7±0.3
χ^2/d.o.f.		324.00/285	250.48/199	116.43/122	144.97/130	92.73/77

* Normalisation of the APEC component is $\frac{1}{4\pi D^2}\int n_e n_{\rm H} dV$, where D is the distance to the source, n_e and $n_{\rm H}$ are the electron and hydrogen densities, respectively, and V is the X-ray emitting volume.
† Unit of 10^{-15} erg cm^{-2} s^{-1} arcmin^{-2} in the 2.0–10.0 keV band.

4.4 Discussion

4.4.1 Absorption column density toward CTB 1

We obtained the absorption column densities of the five regions from the spatially resolved analysis (section 4.3.2). The column densities of the inner radio-shell of regions C, D and E are about 2 times higher than those of the breakout regions of A and B. This result might indicate that there is a local enhancement of the ISM density around the radio shell of CTB 1. Indeed, Yar-Uyaniker et al. (2004) reported the interaction between the CTB 1 shell and a surrounding H I gas. However, excess of a hydrogen column density estimated from the H I gas interacting with CTB 1 ($T_{\rm B} \sim 30$ K at $v_{\rm LSR} = -15.5$–-18.5 km/s) is 1.6×10^{20} cm^{-2}, which is one order of magnitude smaller than that of our observations. No association between CTB 1 and molecular clouds have been reported so far, though the survey of ^{12}CO ($J = 1$–0) in this area was performed by Heyer et al. (1998). Further observations of the cold ISM are necessary to identify the origin of the excess of the X-ray absorption column density at the shell of CTB 1.

We estimated the distance to CTB 1 according to the absorption column density toward the breakout region ($N_{\rm H} \sim 2.3 \times 10^{21}$ cm^{-2}). Assuming the mean interstellar hydrogen density of 1 cm^{-3}, the distance is to be ~ 0.8 kpc. This is the lowest value among estimation from other studies (1.6–3.1 kpc: Craig & Hailey 1997, Yar-Uyaniker et al. 2004). However, the mean interstellar hydrogen density toward the CTB1 direction is highly uncertain. If we adopt a hydrogen density of 0.4 cm^{-3}, we obtained a distance of 2 kpc, which is an intermediate value of the previous estimates. In the following discussion, we assumed a distance of 2 kpc. We confirmed that our conclusions are not affected even when the distance is changed within 0.8–3.1 kpc.

4.4.2 Recombining plasma in the SW region

Previous observations with Chandra and ASCA suggested that both the NE and SW plasmas of CTB 1 are in the CIE state with kT_e of 0.2–0.3 keV (Lazendic & Slane 2006, Pannuti et al. 2010). However, our spectral analyses revealed that the SW plasma is not in CIE but in recombining phase for the first time.

Previous studies of RPs indicate that it is effective for the investigation of the formation process of the RPs to compare between the distributions of densities of ISM and kT_e of the RPs (W49B: Lopez et al. 2013, IC 443: Matsumura et al. 2017b). Lopez et al. (2013) discussed that higher kT_e would be expected in a region with a high ambient gas density if they consider the rarefaction as the formation process of RPs. On the contrary, Matsumura et al. (2017b) founds that kT_e of RPs in shock-cloud interaction regions is significantly lower than those in the other

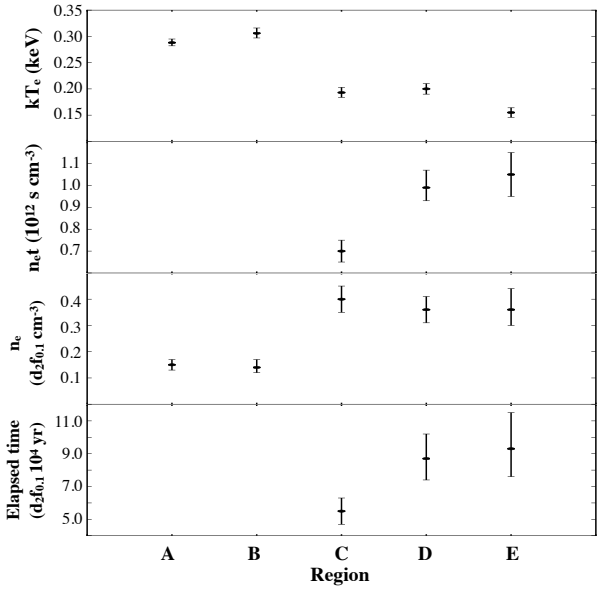

Figure 4.7: Top panel shows electron temperatures in the regions A–E with a unit of keV. Second panel shows ionisation parameters in the regions A–E with a unit of 10^{12} s cm^{-3}. Third panel shows the densities of electrons. d_2 is the distance to CTB 1 divided by 2 kpc and $f_{0.1}$ is the filling factor divided by 0.1. The lower panel shows elapsed times for each region.

region, suggesting that the origin of the RPs is cooling by thermal conduction between the SNR plasma and the cool dense ISM.

CTB 1 provides a unique opportunity to test the formation process of the RP; its ambient density is low at the breakout region and high at the shell region (Yar-Uyaniker et al. 2004). As shown in figure 4.7, we found that kT_e in the inner-shell region is lower than that in the breakout region. Moreover, the rim of the shell (region E) shows the lowest kT_e. Therefore, the RP in CTB 1 is most likely explained by the thermal conduction scenario rather than the rarefaction scenario.

In addition, we calculated the elapsed time since recombination started to dominate over ionisation ($t_{\rm rec}$) using $n_e t$ obtained from our spectral analyses. The bottom two panels of figure 4.7 show the electron densities (n_e) estimated from the best-fit emission measures and the derived $t_{\rm rec}$ for the region C, D, and E. The result suggests that the outer region became an RP earlier than the central region did. It is consistent with the thermal conduction scenario.

Associated molecular clouds are detected with a SNR that shows the RP in radio observation (e.g. Yusef-Zadeh et al. 2003). On the other hand, CTB 1 has an associated H I gas, while no association between CTB 1 and molecular clouds have been reported. Since the density of H I gas is lower than that of molecular clouds, the detection of the RP in CTB 1 suggests that it is possible to produce RPs by thinner gas than molecular clouds.

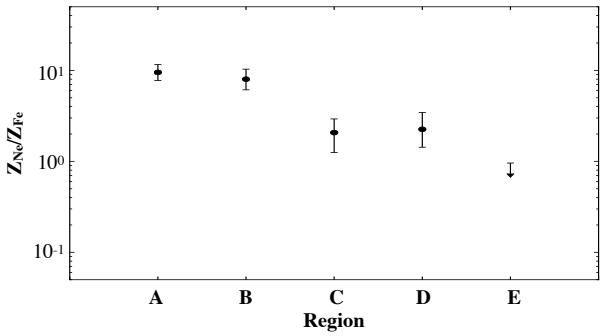

Figure 4.8: The abundance ratios of Ne to Fe in the regions A–E.

4.4.3 Spatial variation of the metal abundances

The Ne and Mg abundances are larger than the solar values in both the NE and SW regions. This result is consistent with results of previous studies (Lazendic & Slane 2006, Pannuti et al. 2010). In contrast, we found that the abundance of Fe in the SW region is much higher than that in the NE region. We note that the Fe abundance is significantly affected by an assumed model as shown in a comparison between the SW Model1 and the SW Model2 (see table 4.4). Therefore, precise modelling of the ionisation state of the plasma is crucial to determine the metal abundances.

Figure 4.8 shows a spatial variation in the abundance ratio of Ne to Fe. The ratios are systematically larger than unity suggesting the origin of a core-collapse supernova (e.g. Nomoto et al. 2006, Takeuchi et al. 2016). In addition, the ratios in the inner-radio shell region are smaller than those in the breakout region, particularly Fe is enhanced in the region E. This result indicates an asymmetric ejecta distribution as also found in other SNRs with the origin of core-collapse supernovae (e.g. Katsuda et al. 2008, Uchida et al. 2009). One of the possibilities is that Ne was isotropically ejected while Fe was ejected toward SW.

4.4.4 Origin of the hard-band excess

We found that the observed fluxes above 2 keV are larger than that of the CXB model by $\sim$13–47% in both NE and SW regions. These hard-band excesses are represented by power-law functions. Figure 4.9 shows photon indexes and surface brightnesses for all the regions. The photon index is in the range of 2–3, and marginal spectral steeping is seen at the outer of CTB 1. On the other hand, the surface brightness has a peak at the centre of the radio shell. A flux and a luminosity integrated over the observed regions in the 2–10 keV band are 4.5×10^{-13} erg s^{-1}cm^{-2} and $2.2 \times 10^{32} d_2^2$ erg s^{-1}, respectively, where d_2 is the distance to CTB 1 divided by 2 kpc. A spatial extent of the hard X-ray emission is 20 d_2 pc.

The detection of power-law components in the NE and SW regions is reported using ASCA spectra by Pannuti et al. (2010). The photon indexes and the fluxes they derived are consistent with those of our results. They also argued that a thermal plasma with $kT_e \sim 3$ keV, which might be a high-temperature plasma component in CTB 1, can explain the observed spectra instead of the power-law component. However, fitting a thermal plasma model to the Suzaku spectra (NE Model2) requires an extremely low abundance due to a lack of emission lines from He-like Fe. Because such a low abundance is not explained by either a supernova ejecta nor the ISM, the high-temperature plasma associated with CTB 1 is unlikely.

One possible origin of the hard-band excess is a flux fluctuation of the CXB due to the cosmic variance. Indeed, an expected amplitude of the fluctuation is $\sim 15\%$ for the Suzaku FoV (Moretti et al. 2009). We fitted the background spectra again with the free CXB normalisations to confirmation the CXB fluctuation in the two background regions. We found that the difference in the CXB normalisations between BG1 and BG2 is 14%, which is consistent with the above expectation. On the other hand, the hard-band excesses in CTB 1 are 13–47% of the CXB flux. The hard-band excesses in the regions B, C, and D are clearly higher than the expected fluctuation. Moreover, the derived photon index is significantly steeper than that of the CXB, and the excesses are observed in all regions. Therefore, the origin of the CXB fluctuation is unlikely.

No clear association is seen between the X-ray hard-band excess and the radio shell on the basis of the morphology. One possible origin is a pulsar wind nebula, since Γ, the luminosity, and the spatial extent is in the range of old Galactic pulsar wind nebulae (Kargaltsev et al. 2008, Bamba et al. 2010). According to the empirical relation between the luminosity and the characteristic age (Mattana et al. 2009), the characteristic age is to be 10^4–10^5 yr, which is consistent with the age of CTB 1. We estimated the spin down luminosity of the pulsar to be 2.8×10^{35} erg s^{-1} assuming $L_{\rm x}/\dot{E}_{\rm rot} = 8 \times 10^{-5}$ for old pulsar wind nebulae (Vink et al. 2011). However, no pulsar has been detected at the centre of CTB 1. Moreover, gamma-ray emission from a pulsar wind nebula has not been detected so far even though an expected TeV gamma-ray luminosity is $\sim 10^2 L_{\rm x}$ according to the relation shown by Mattana et al. (2009). Further multi-wavelength observations are necessary to examine this scenario.

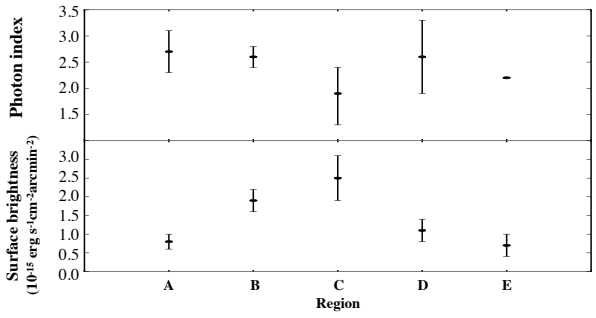

Figure 4.9: Top panel shows the photon index in the regions A–E. The photon index for the region E is fixed at the best-fit value of the entire SW region (2.2). The lower panel shows the surface brightness (2.0–10 keV) in the regions A–E with a unit of 10^{-15} erg cm^{-2}s^{-1}arcmin^{-2}.

Chapter 5

Time dependent model of X-ray emitting plasma in SNRs

In this chapter, we develop a model that describes time evolution of an SNR and its X-ray emission. To calculate the physical conditions of the plasma associated with the SNR, this model is implemented into a simulation code that treats one-dimensional hydrodynamics of the gas driven by interactions between the SN ejecta and its surroundings. The code then calculates X-ray spectra that are radiated from spatially resolved parts of the plasma at every temporal step set by the simulation. In order to check the accuracy of the code, we examine results of the simulation using several sets of parameters.

5.1 Basic Concept

In order to study the formation process of recombining plasmas with thermal X-ray emission, we need to analyse observational data using accurate models that include the time evolution of SNRs. The recombining plasmas have been observed in middle-aged and old SNRs, i.e. 10^4 yr after the explosion. However, any detailed simulations of a long timescale of several 10^4 yr have not been performed yet. We therefore develop a new framework to calculate X-ray spectra based on a one-dimensional numerical hydrodynamics simulation which can follow time evolution of SNRs for a few 10^4 yr. For interpretation of the X-ray spectra, it is important to calculate elemental abundances and ion fractions which determine the intensities of the X-ray emission.

We adopt the Lagrangian method, which describes gas flow by tracking motion of fluid particles, as opposed to the Eulerian method describing the fields of fluid properties. Thanks to conservation of a layer mass in the one-dimensional Lagrangian method, abundances in each grid can be fixed to the initial values.

Our simulation provides a method for generating X-ray spectra and images of evolved SNRs. An outline of the calculation is shown in Figure 5.1. The first step in the code (in Figure 5.1) is called the "hydrodynamics code" which uses a one-dimensional numerical hydrodynamics simulation to calculate the time evolution of the SNR plasma. The second step referred to as the "synthesis" is a spectral synthesis to generate X-ray spectra and images from the outputs of the hydrodynamics code.

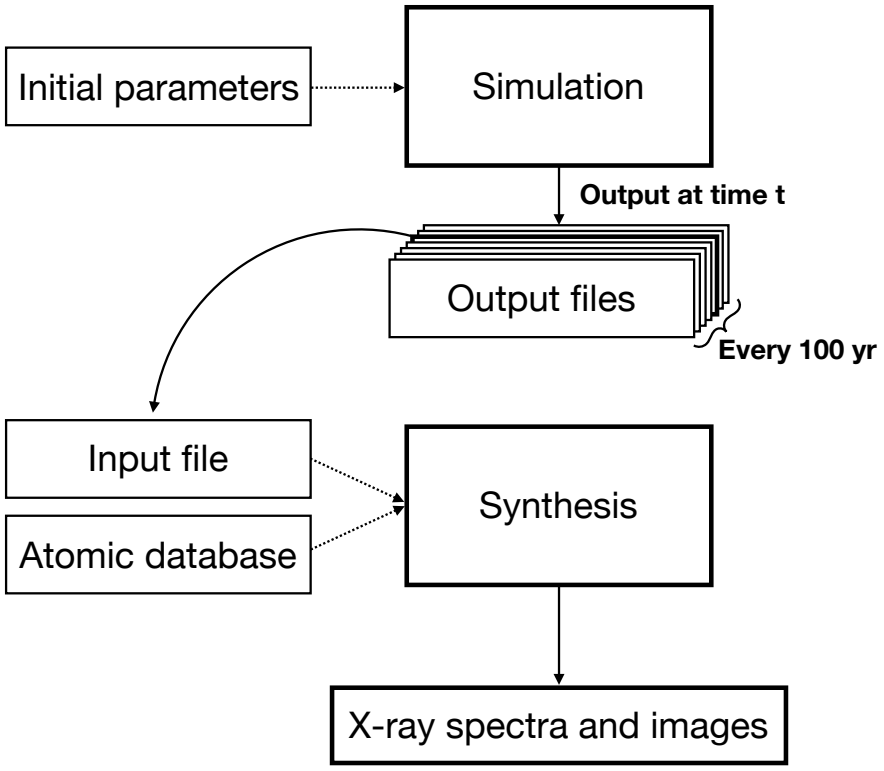

Figure 5.1: Outline of our numerical simulation code.

5.2 Hydrodynamics code

The hydrodynamics code provides a calculation of the time evolution of the temperatures and ion fractions based on the one-dimensional Lagrangian hydrodynamics simulation assuming spherical symmetry. Figure 5.2 shows the structure of the hydrodynamics code. To compute the initial conditions of the simulation, the code requires input parameters about the SN and its ambient gas. Based on the open-source Lagrangian hydrodynamics code VH-1, we here develop a hydrodynamics simulation that uses the Lagrangian grid number (i) and time (t) as independent variables. The simulation outputs a file in every 100 years containing a list

of information that includes the position of the forward shock (FS) and reverse shock (RS), age, and the grid position, grid width, density, pressure, velocity, temperatures of electrons and ions, and number density of electrons and ions.

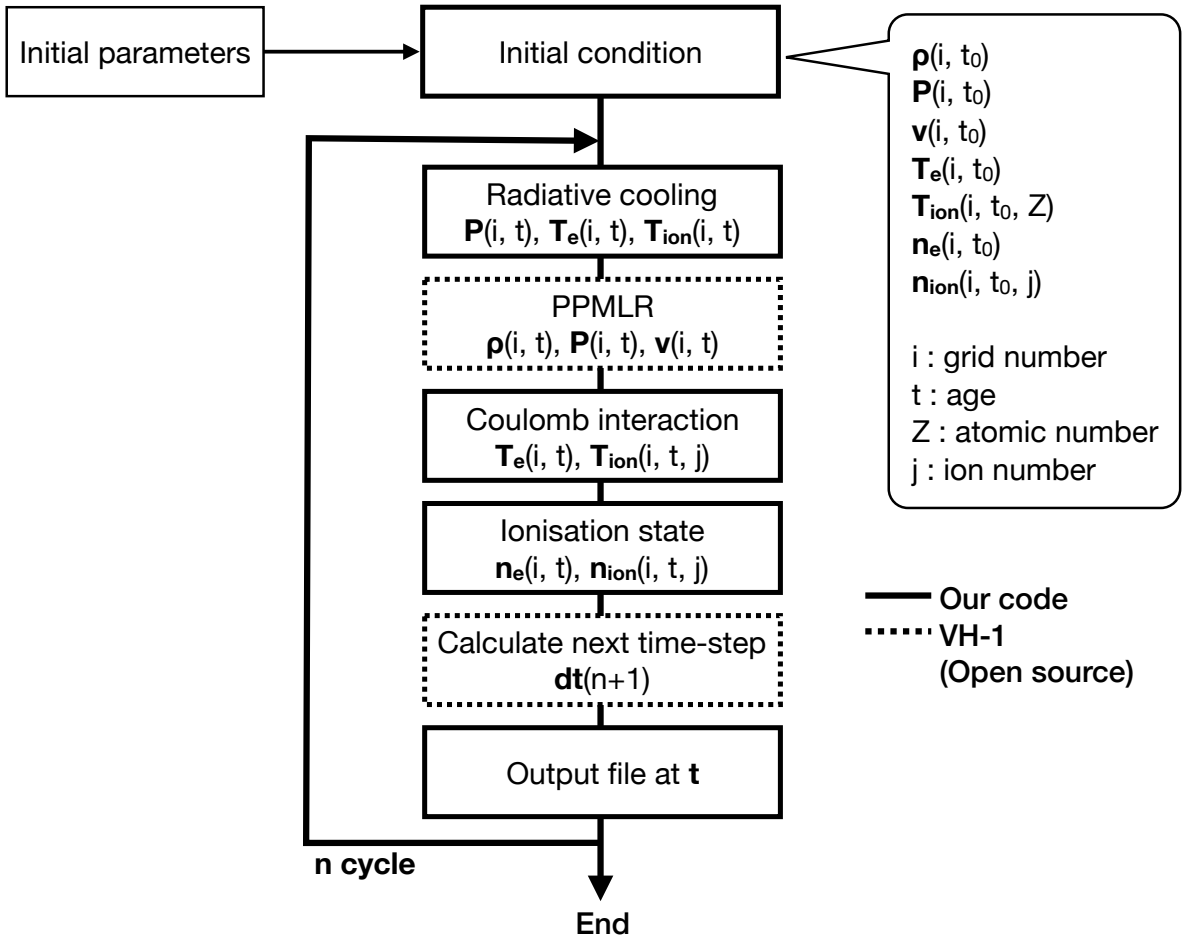

Figure 5.2: Outline of our hydrodynamics code.

5.2.1 The piece-wise parabolic method (PPM) in the Lagrangian coordinates

We adopt the VH-1 code which provides a framework for the Lagrangian hydrodynamics simulation. VH-1 is a multidimensional ideal compressible hydrodynamics code which was originally written by Prof. John Hawley and several postdocs and students at the University of Virginia in 1990. We describe an overview of the VH-1 code, which is open-source. VH-1 has 5 steps as follows:

1. Read an input data file "indat") for job control parameters

2. Open history file for recording metadata

3. Create the simulation grid

4. Set initial conditions

5. Loop over time (time = time + dt)

   (a) Hydrodynamic evolution

   (b) Compute maximum stable time step

   (c) Output data to disk

The required input file ("indat") determines the name of the output files, an interval of output time, and the end time of a simulation. Simulation grids are generated before the loop (5) and the mass in each grid is kept constant throughout the loop. The initial conditions needed in VH-1 are the density, pressure and velocity profiles, and their time evolution is calculated in each loop. The time step dt is defined by the initial sound speed $svel_{init}$ or the speed $xvel$ of a moving fluid as

$$svel_{init} = \max\left(\frac{\sqrt{\frac{\gamma P(i)}{\rho(i)}}}{dx(i)}\right), \tag{5.1}$$

$$xvel = \max\left(\frac{|u(i)|}{dx(i)}\right), \tag{5.2}$$

$$dt = \frac{0.5}{\max(svel_{init}, xvel)}, \tag{5.3}$$

where i and γ are the grid number and heat capacity ratio, and the gas is assumed to be ideal ($\gamma = 5/3$). In step 5, the code computes the hydrodynamical evolution of the system based on the Lagrangian-Remap version of the Piece-wise Parabolic Method (PPMLR).

The Piece-wise Parabolic Method (PPM) in Lagrangian coordinates is a scheme for solving a linear advection equation developed by Colella & Woodward (1984). The equations of gas dynamics in Lagrangian coordinates in conservation form are

$$\partial_t \tau - \partial_m (r^\alpha u) = 0 \tag{5.4}$$

$$\partial_t u + r^\alpha \partial_m P = 0 \tag{5.5}$$

$$\partial_t E + \partial_m (r^\alpha u P) = 0, \tag{5.6}$$

where τ, u, P, E, and m are the specific volume, the fluid velocity, the gas pressure, the total energy per unit volume, and a mass coordinate, respectively. α is a coefficient which depends

on a type of spatial symmetry: planar (= 0), cylindrical (= 1), or spherical (= 2). The total energy per unit mass is the sum of the kinetic energy and the internal energy e described as

$$E = \frac{1}{2}u^2 + e. \tag{5.7}$$

The density ρ and the pressure P are derived from the conserved quantities via

$$\rho = \frac{1}{\tau}, \tag{5.8}$$
$$P = (\gamma - 1)\rho e. \tag{5.9}$$

The difference approximation to the fundamental conservation law in equations (5.4), (5.5), and (5.6) is as follows:

$$x_{j+1/2}^{n+1} = x_{j+1/2}^{n} + \Delta t \overline{u}_{j+1/2}, \tag{5.10}$$
$$\overline{A}_{j+1/2} = \frac{(x_{j+1/2}^{n+1})^{\alpha+1} - (x_{j+1/2}^{n})^{\alpha+1}}{(\alpha+1)\overline{u}_{j+1/2}\Delta t}, \tag{5.11}$$
$$u_j^{n+1} = u_j^n + \frac{1}{2}(\overline{A}_{j+1/2} + \overline{A}_{j-1/2})\frac{\Delta t}{\Delta m_j}(\overline{P}_{j-1/2} - \overline{P}_{j+1/2}), \tag{5.12}$$
$$E_j^{n+1} = E_j^n + \frac{\Delta t}{\Delta m_j}(\overline{A}_{j-1/2}\overline{u}_{j-1/2}\overline{P}_{j-1/2} - \overline{A}_{j+1/2}\overline{u}_{j+1/2}\overline{P}_{j+1/2}) \tag{5.13}$$

Here $\overline{u}$ and $\overline{P}$ are the time-averaged values of the velocity and pressure at the Lagrangian grid.

5.2.2 Initial conditions

In order to simulate the plasma of SNRs, we compute the initial conditions of the SNR shortly after the explosion and surrounding environment. The initial conditions in each layer are the density, pressure, velocity, temperatures of electrons and ions, and elemental abundances and ion fractions of each element. These initial conditions are determined from the initial parameters which are defined by a type of SN and its surrounding environment. In our simulations, the surrounding environment consists of the ISM and CSM (originating from the stellar wind) in the case of CC SNe. The simulation begins at an age of 20 yr when the SNR is assumed to be in free expansion. We regard the plasma as an ideal gas in all simulations.

The initial parameters required by the simulation code are as follows:

- E_{SN}: Energy of the SN explosion (erg)
- M_{ej}: Mass of the ejecta (g)
- *Abd*: Abundance pattern normalised with respect to hydrogen

- $v_{\rm ej,max}$: Maximum velocity of the ejecta (cm s^{-1})
- n_{ISM}: Number density of the ISM (cm^{-3})

E_{SN} and M_{ej}, are Abd_{ej} are estimated from published models of the ejecta immediately after the explosion. We use the s25D model for CC SNe, which is a progenitor with a mass of 25 $M_\odot$ based on Rauscher & Thielemann (2000). The explosion energy and ejecta mass are 1.2×10^{51} erg and 12.3 $M_\odot$, respectively. For Ia SNe, we use a delayed-detonation model: DDTa (Badenes et al. 2008) with a ejecta mass of 1.38 $M_\odot$ and E_{SN} of 1.4×10^{51} erg. Figure 5.3 shows abundance distribution of s25D and DDTa models. For the abundance of the CSM and ISM, we use the ISM abundances in Wilms et al. (2000). We assume that the neutral and singly ionised ions occupy 90% and 10% for all elements (e.g., X_{ion}(C I, C II, C III, ..., C VII) = 0.9, 0.1, 0, ..., 0), $v_{\rm ej,max}$ is $\sim$ 0.05–0.1% of the speed of light, which is set to keep by the continuity of the density between the ejecta and the CSM. The initial temperatures of the ejecta, CSM and ISM are assumed at 10^4 K where X-ray radiation is not emitted. The temperatures of the CSM and ISM are kept constant until they are shocked.

To calculate the initial conditions, we need to decide the grid positions, i.e. the radius $r(i,t_0)$ and width $dr(i,t_0)$. Since free expansion is assumed at t_0, the radius of SNR, $r_{\rm ej,max}$, is given by $v_{\rm ej,max}t_0$. In our simulation, 10% of the total Lagrangian grid elements (N_{grid}) are assigned for the ejecta and the others are used for the ambient gas. $r(i,t_0)$ and $dr(i,t_0)$ are calculated by

$$r(i,t_0) = \sum dr(i,t_0) \tag{5.14}$$

$$dr(i,t_0) = \begin{cases} \frac{r_{\rm ej,max}}{0.1N_{grid}} & (i < 0.1N_{\rm max}) \\ \frac{(r_{\rm max}-r_{\rm ej,max})}{0.9N_{\rm max}} & (i > 0.1N_{\rm max}), \end{cases} \tag{5.15}$$

where $r_{\rm max}$ is the maximum radius of the ambient gas.

The initial density, pressure and velocity are calculated using these initial parameters. We take a simple composition of the density function of the mass coordinate. For the ejecta, we use a power-law profile ($\rho_{ej} \propto r^{-n}$) with a plateau in the inner core (Chevalier 1982, Truelove & Mckee 1999). The index n is a parameter chosen to fit the density profile from the SN explosion simulations. The solution of n = 9 is adopted for simulations of CC SNe. Thus, the density of ejecta is defined as

$$\rho(i,t_0) = \begin{cases} \rho_{flat} & (r(i,t_0) < r_{flat}) \\ C_{ej}r(i,t_0)^{-n} & (r_{flat} < r(i,t_0) < r_{\rm ej,Max}), \end{cases} \tag{5.16}$$

where C_{ej} is $\rho_{flat}r_{flat}^n$ considering the boundary condition at r_{flat}. ρ_{flat} and r_{flat} are calculated from the mass of the ejecta and energy of the explosion. The total ejecta mass (M_{ej}) is divided

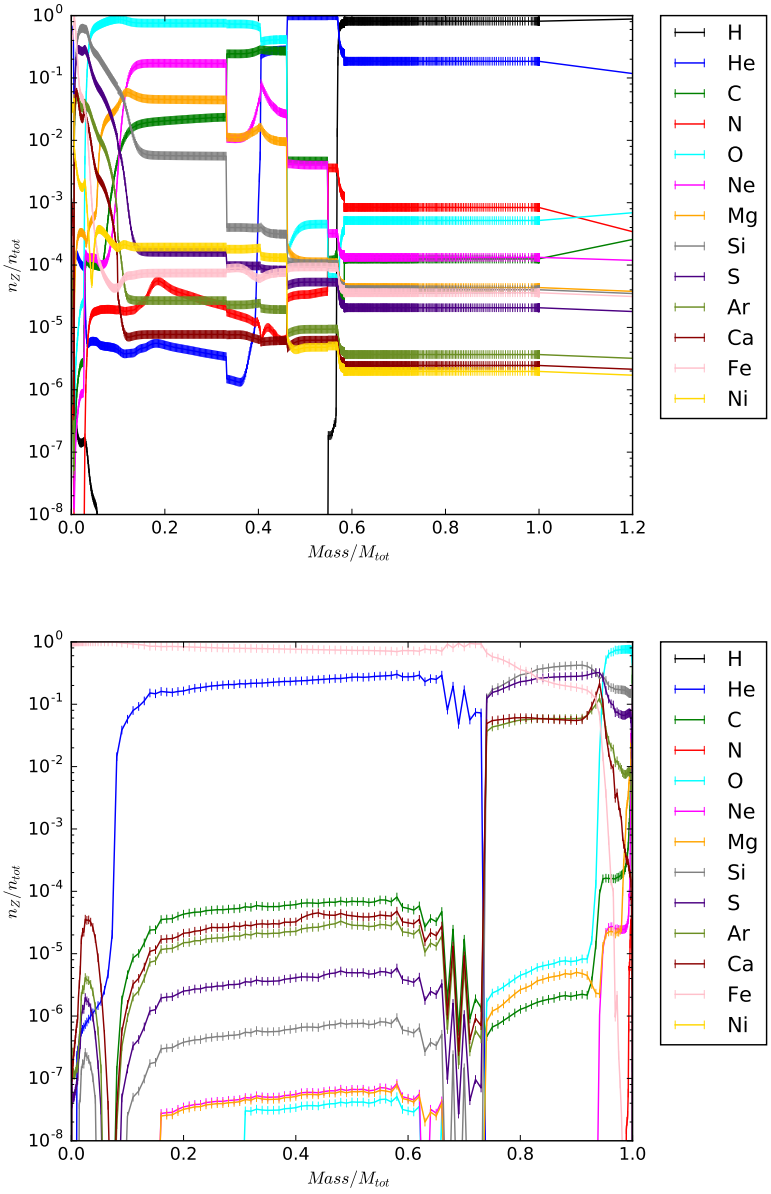

Figure 5.3: Abundances of models s25D (top) and DDTa (bottom) as functions of enclosed mass.

into the masses with a flat density profile (M_{flat}) and a power-law profile (M_{pl}) defined as

$$\begin{aligned} M_{ej} &= M_{flat} + M_{pl} && (5.17)\\ &= \int_{r=0}^{r=r_{flat}} \rho_{flat} dV + \int_{r=r_{flat}}^{r=r_{\rm ej,max}} \rho_{flat} r_{flat}^{n} r^{-n} dV && (5.18)\\ &= \rho_{flat}\frac{4}{3}\pi r_{flat}^{3} + \rho_{flat} r_{flat}^{n}\frac{4}{3-n}\pi(r_{\rm ej,max}^{3-n} - r_{flat}^{3-n}). && (5.19) \end{aligned}$$

Then ρ_{flat} is indicated by r_{flat} as

$$\rho_{flat} = \frac{M_{ej}}{\frac{4}{3}\pi r_{flat}^{3} + \frac{4}{3-n}\pi r_{flat}^{n}(r_{\rm ej,max}^{3-n} - r_{flat}^{3-n})}. \quad (5.20)$$

The explosion energy (E_{SN}) is similarly divided into E_{flat} and E_{pl} which are kinetic energy ($\frac{1}{2}mv^2$) of the free expansion, given by

$$\begin{aligned} E_{SN} &= E_{flat} + E_{pl} && (5.21)\\ &= \int_{r=0}^{r=r_{flat}} \frac{1}{2} v(r)^2 \rho_{flat} dV + \int_{r=r_{flat}}^{r=r_{\rm ej,max}} \frac{1}{2} v(r)^2 \rho_{flat} r_{flat}^{n} r^{-n} dV, && (5.22) \end{aligned}$$

where v is the velocity r/t. Therefore, the explosion energy is

$$E_{SN} = \frac{2\pi\rho_{flat}}{t_0^2}\frac{r_{flat}^{5}}{5} + \frac{2\pi\rho_{flat}}{t_0^2}\frac{r_{flat}^{n}}{5-n}(r_{\rm ej,max}^{5-n} - r_{flat}^{5-n}), \quad (5.23)$$

where t_0 is the age of the SNR when the simulation begins. With these equations in mind, we search for the value of r_{flat} for which the total ejecta mass matches the SN explosion model within an error of 10^{-6}.

In the case of CC SNe, we assume a CSM with the density of $\rho_{wind} \propto r^{-2}$ corresponding to the pre-SN wind (Chevalier 1982). Considering a mass ejected as a symmetric flow from a SN and a constant wind velocity v_{wind}, the density is given by

$$\rho(r) = \frac{\dot{M}}{4\pi v_{wind}} r^{-2}, \quad (5.24)$$

where $\dot{M}(= dM/dt)$ is the mass loss rate by Chevalier & Luo (1994), which is fixed at a typical value of $10^{-5} M_\odot$ yr^{-1} in our simulation. On the other hand, the ISM density is simply constant with n_{ISM}. Thus, the density in the surrounding environment is given by

$$\rho(i,t_0) = \begin{cases} \frac{\dot{M}}{4\pi v_{wind}} r(i,t_0)^{-2} & (r_{\rm ej,max} < r(i,t_0) < r_{\rm CSM,max}) \\ n_{\rm ISM} m_p & (r_{\rm CSM,max} < r(i,t_0)), \end{cases} \quad (5.25)$$

where m_p is the proton mass and the CSM is ignored in the Type Ia SNe simulation. $r_{\rm CSM,max}$ is the maximum radius of the CSM determined by the continuity of the density ($\dot{M} r_{\rm CSM,max}^{-2}/4\pi v_{wind} = n_{\rm ISM} m_p$).

In our calculation cosmic rays and magnetic flux density are ignored for simplicity. Therefore, particle acceleration process is ignored and the explosion energy is fully transferred into thermal energy. Since we assume an ideal gas and a free expansion phase, the pressure is calculated by the simple equation $P = nk_BT$ using the Boltzmann constant k_B. The pressure is given from the equation of state as

$$P(i, t_0) = \frac{\rho(i, t_0)}{\mu m_p} k_B T(i, t_0), \tag{5.26}$$

were μ is mean weight. In addition, the gas in the free expansion phase is considered to have a constant velocity. Therefore, the velocity of the ejecta is indicated as

$$v(i, t_0) = \frac{r(i, t_0)}{t_0} \quad (i < 0.1 N_{grid}). \tag{5.27}$$

The velocity of the wind and ISM are simply fixed at 20 km s^{-1} and 0 km s^{-1}, respectively. The variables ρ, P and v are dimensionless using r_{ch} and t_{ch} which are unique characteristic length and time scales, respectively (Chevalier 1982). Figure 5.4 shows an example of initial conditions for a model of CC SNe with $n_{\rm ISM}$ of 1 cm^{-3} at an age (t_0) of 20 yr. The contact discontinuities are smoothed by a gaussian.

5.2.3 Time evolution of electrons and ions temperatures in plasma

For modelling of X-ray emission of plasma in SNRs, the temperature evolution of electrons and ions is important. We have to consider the cooling and heating processes of particles in a plasma, such as shock heating, the adiabatic compression and expansion, Coulomb collisions between particles with different temperatures, and radiative cooling. Since the adiabatic process is already included in the hydrodynamics code, in this section, we describe the other processes included in our framework.

Shock wave heating

In order to simulate the time evolution of the temperatures and ion fraction, we have to detect the positions of shocks and calculate the post-shock temperature. The important shocks in SNRs are the forward shock (FS), which are created by the swept matter and is driven into the CSM and the ISM, and the reverse shock (RS), which is driven back into the ejecta. Ions are heated up to $\sim 10^8$ K after the strong shock and ionised to H- and He- like states.

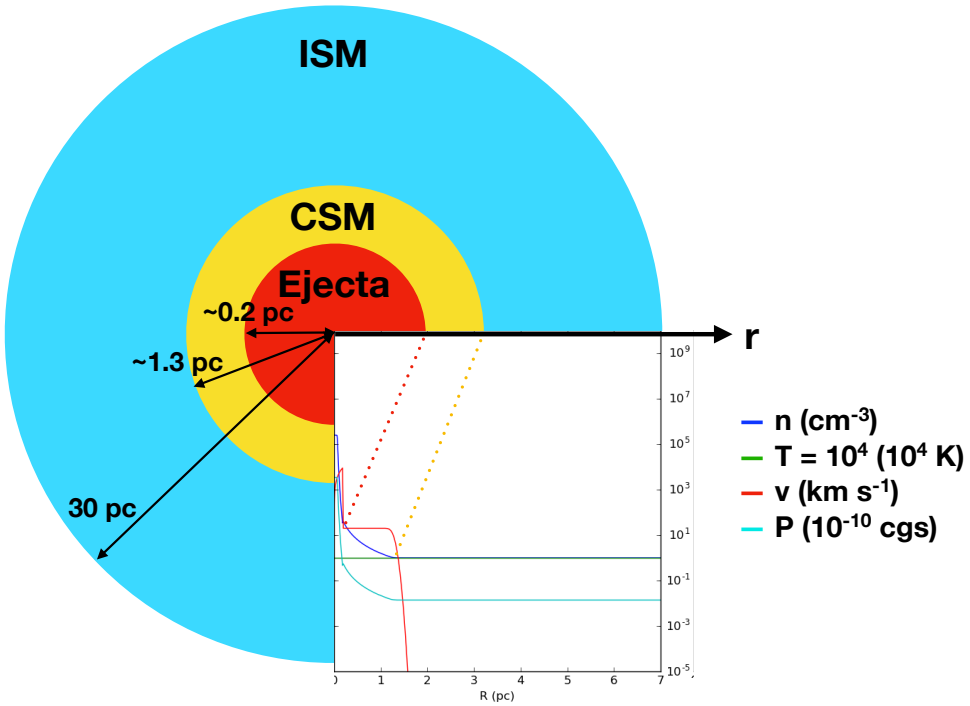

Figure 5.4: The initial condition of a CC SN with $n_{ISM} = 1$ cm^{-3} at t_0.

In our code, the FS is detected by the gradient g_P of the pressure defined by

$$g_P(i) = \frac{P(i+1) - P(i-1)}{P(i+2) - P(i-2)}. \tag{5.28}$$

When the $g_P(i)$ reaches its maximum value, the grid element i is considered to be the position i_{FS} of the FS. On the other hand, the RS is found using the transition of the velocity $u(i)$ of the plasma. We defined a grid element where the velocity slows down at first $(u(i) - u(i-1) < 0)$, as the position i_{RS} of the RS.

After the detection of shocks, the post-shock temperatures are calculated from the pressure, density and abundances. Assuming an ideal gas, the pressure equals nk_bT, then the pressure $P(i,t)$ is indicated as

$$P(i,t) \quad = \quad \sum_Z n_Z k_b T_Z + n_e k_b T_e. \tag{5.29}$$

We assume that ion temperatures are set in proportion to the mass number of each ion as $T_Z/T_p = A_Z$. We also assume that $T_e/T_p = m_e/m_p$ for electrons. A higher value of T_e/T_p relative to the mass ratio can change the ionisation structure behind the shock but for simplicity

we ignore this effect (e.g. Yamaguchi et al. 2014b). The equation (5.29) changes to

$$P(i,t) = n_p k_b T_p (\sum_Z Abd_Z A_Z + n_e \frac{m_e}{m_p}). \tag{5.30}$$

Using equation (5.30), the post-shock temperature of a proton is estimated from

$$T_p(i,t) = \frac{P(i,t)}{n_p(i,t) k_b (\sum_Z Abd_Z(i) A_Z + n_e(i,t)\frac{m_e}{m_p})}, \tag{5.31}$$

$$n_p(i,t) = \frac{\rho(i,t)}{\sum_Z m_p Abd_Z A_Z + \sum_Z m_e Abd_Z Z}, \tag{5.32}$$

$$n_e(i,t) = \sum_{Z,j} n_p(i,t) Abd_Z X_{ion}(i,t,Z,j) j. \tag{5.33}$$

Coulomb interaction

One of the important physical processes in NEI plasma is the interaction between electrons and ions by Coulomb collisions. When a charged particle moves through a plasma, it experiences weak Coulomb electric field forces from the surrounding charged particles. Then, the particles exchange energy and their temperatures reach equilibrium on the Coulomb collision timescale as we described in section 2.

Assuming the incident particle a and the target gas b, the Coulomb equilibration timescale between the two charged particles is calculated by Spitzer (1965) as

$$t_{eq}(a,b) = \frac{3}{8\sqrt{2\pi}} \frac{m_a m_b}{n_b Z_a^2 Z_b^2 e^4 \log\Lambda} \left(\frac{k_B T_a}{m_a} + \frac{k_B T_b}{m_b} \right)^{\frac{3}{2}}, \tag{5.34}$$

where m, Z and k_B are the particle mass, the atomic number, and the Boltzmann constant, respectively. $\log \Lambda$ is the Coulomb logarithm for the collisional pair given by

$$\log\Lambda = \log \left(\frac{b_{\max}}{b_{\min}} \right). \tag{5.35}$$

$b_{\max}$ is the Debye Length as

$$b_{\max} = \sqrt{\frac{kT_e}{4\pi e^2 n_e}}. \tag{5.36}$$

b_{min} is $\max(b_{\min}^{\rm cl}, b_{\min}^{\rm qm})$ (Callen 2006). For electron–ion collision, $b_{\min}^{\rm cl}$ and $b_{\min}^{\rm qm}$ are indicated by

$$b_{\min}^{\rm qm} = \frac{h}{4\pi\sqrt{3kT_e m_e}}, \quad b_{\min}^{\rm cl} = \frac{Z_b e^2}{3kT_e}. \tag{5.37}$$

On the other hand, they are described in the case of ion–ion collisions as follows:

$$b_{\rm min}^{\rm cl} = \frac{Z_a Z_b e^2}{m_{\rm cm}\overline{u^2}}, \quad b_{\rm min}^{\rm qm} = \frac{h}{4\pi m_{\rm cm}\sqrt{\overline{u^2}}}, \tag{5.38}$$

where the mass $m_{\rm cm}$ is defined by the reduced mass, $m_a m_b/(m_a + m_b)$. The average of u^2 over the distribution of target particles is

$$\overline{u^2} = 3\left(\frac{kT_a}{m_a} + \frac{kT_b}{m_b}\right). \tag{5.39}$$

$$\tag{5.40}$$

When a particle moves in the dense gas, the temperatures of the incident particle and the target gas become close in a short time, since the equilibration timescale is inversely proportional to the density of the target gas.

The temperature change of a particle a is indicated by

$$\frac{dT_a}{dt} = \frac{T_b - T_a}{t_{eq}(a,b)}. \tag{5.41}$$

Considering dT for electrons and all ions (z), the behaviour of their temperatures is indicated by

$$dT_z = \frac{T_e - T_z}{t_{eq}(z,e)}dt + \sum_{z\neq z'}\frac{T_{z'} - T_z}{t_{eq}(z,z')}dt, \tag{5.42}$$

$$dT_e = \sum_z \frac{T_z - T_e}{t_{eq}(e,z)}dt. \tag{5.43}$$

In our simulations, the new temperatures of ions and electrons is estimated using equation (5.44) and (5.45) as follows:

$$T_z(i,t+dt) = T_z(i,t) + \frac{T_e(i,t) - T_z(i,t)}{t_{eq}(z,e)}dt + \sum_{z'\neq z}\frac{T_{z'}(i,t) - T_Z(i,t)}{t_{eq}(z,z')}dt, \tag{5.44}$$

$$T_e(i,t+dt) = T_e(i,t) + \sum_z \frac{T_z(i,t) - T_e(i,t)}{t_{eq}(e,z)}dt. \tag{5.45}$$

We perform a test calculation for a simple case of H and electron. Figure 5.5 shows results of temperatures and the Coulomb equilibration timescale calculated by equation (5.34). The behaviour of the difference between the electron and H temperatures is consistent with the Coulomb equilibration timescale.

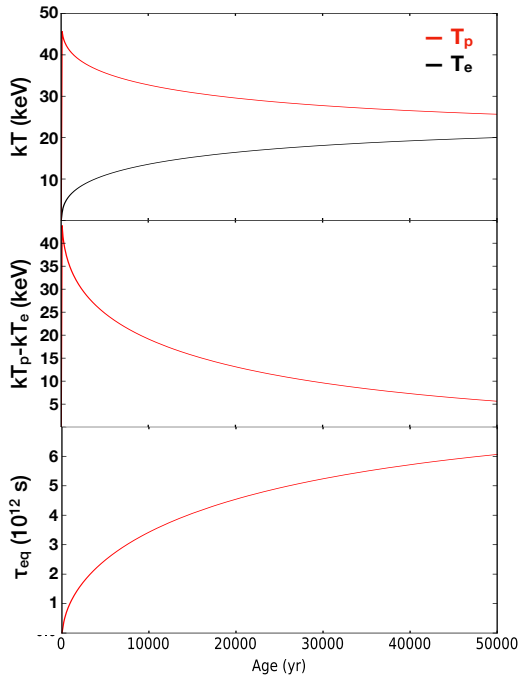

Figure 5.5: Top panel shows the electron and H temperatures obtained from the simulation. The second panel shows the difference between them. The bottom panel shows the Coulomb equilibration timescale calculated by equation (5.34). The change of the difference between kT_e and kT_p is consistent with τ_{eq}.

Radiative cooling

When particles in a plasma emit line and continuum radiation as described in chapter 2, they lose energy and their temperatures decrease. This phenomenon is called radiative cooling. The radiative cooling has an important effect in optically thin plasma, especially with temperatures in the range of 10^4–10^7 K. Therefore it is important that the radiative cooling is treated correctly in our simulation.

When a particle loses energy by emitting radiation, the total energy loss (erg s^{-1}) is described by

$$\frac{dE}{dt} = -\int n_H n_e \Lambda_N(T) dV, \tag{5.46}$$

where Λ_N is the cooling rate in units of erg s^{-1} cm^3 (Schure et al. 2009). Considering the total energy loss to be the total luminosity in the X-ray band ($dE/dt = L_X$), the cooling rate can be estimated from the X-ray spectra. Because the cooling rate is calculated by summing the contributions of all different ion species, it depends on the appropriate abundance ratio and

ion fraction as follows:

$$\Lambda_N(T) = \sum_Z \frac{n_Z}{n_Z(solar)} \Lambda_N(Z,T). \tag{5.47}$$

The cooling rate for each ion ($\Lambda_N(Z,T)$) and the cooling rate ($\Lambda_{hyd}(T)$) assuming $n_H = n_e$ are also estimated in Schure et al. (2009).

Figure 5.6 shows Λ calculated by Schure et al. (2009). They calculated the cooling rate Λ_N from X-ray spectrum in SPEX code, which includes the bound-bound, free-bound, and free-free emissions assuming a CIE plasma with solar abundances. The free-free emission dominates X-ray emissions in a high temperature ($\sim 10^{7-8}$ K), while the bound-bound emission is effective in the plasma with a low temperature. In the bound-bound emission process, a free electron collides with an ion (electron-ion collision) and excites it, then the ion emits X-ray radiation. Since the electron-ion collision is more effective than the ion-ion collision, the bound-bound emission is regarded as cooling of electrons. On the other hand, the free-bound emission is the capture of a free electron by an ion, then, the number of free electrons changes and the electron temperature does not change. However, the contribution of the RRC emission is smaller than that of the free-free emission in CIE plasma. The radiative cooling is considered to be electron cooling on the assumption that a plasma is CIE, though it is not accurate for detail processes such as the ion-ion collision and RRC emission in NEI plasma.

We adopt the cooling curve of the CIE plasma with solar abundances in Schure et al. (2009) regardless of the plasma state (CIE and NEI), for simplicity. Λ_N in Figure 5.6 is used for our simulation. Using equation (5.47), the energy loss rate per unit volume by the radiative cooling is calculated by

$$\frac{de}{dt} = -n_H n_e \Lambda_N(T), \tag{5.48}$$

where e is the energy per unit volume. In order to account for the effects of the radiative cooling in our hydrodynamics code, we update the pressure $P(i,t)$ by

$$\begin{aligned} P(i,t+dt) &= P(i,t) + dP(i,t), & (5.49)\\ &= P(i,t) + \frac{2}{3}\frac{de}{dt}dt, & (5.50)\\ &= P(i,t) - \frac{2}{3} n_H(i,t) n_e(i,t) \Lambda_N(T_e(i,t))dt. & (5.51) \end{aligned}$$

Then, the electron temperature is also update by

$$T_e(i,t+dt) = T_e(i,t) - \frac{2}{3k_b} n_H(i,t) \Lambda_N(T_e(i,t))dt. \tag{5.52}$$

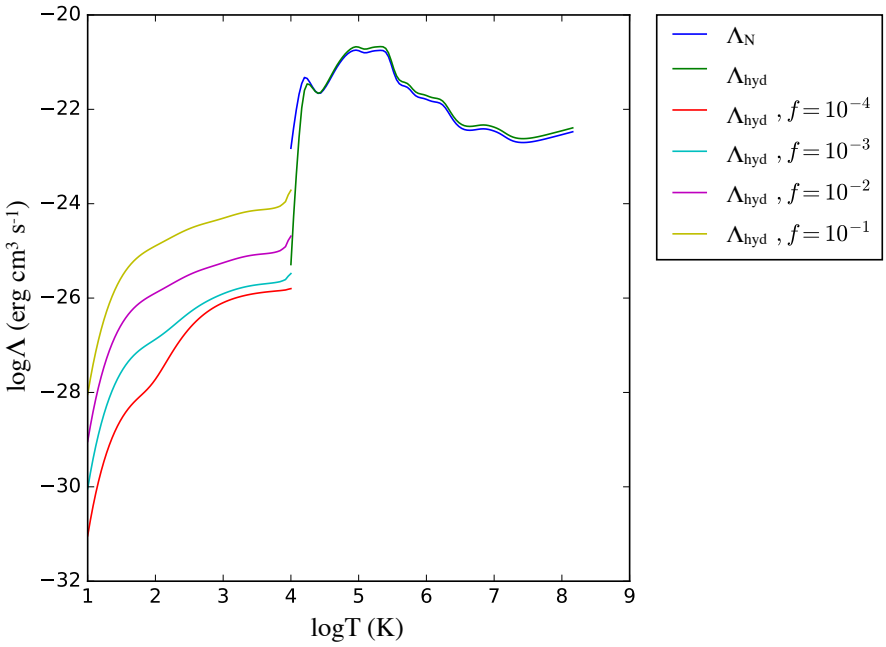

Figure 5.6: Cooling curve from Schure et al. (2009). f is the ionisation fraction, n_e/n_H. The CIE plasma with solar abundances is assumed.

5.2.4 Time evolution of the ion fractions

The shape of the emitted X-ray spectra depend on the electron temperature and the ion fractions. Therefore, we need to calculate the time evolution of the ionisation state for all elements. In our simulation, the ion fractions of 13 elements are estimated based on the ionisation and recombination rate.

The rates of ionisation $I(j)$ and recombination $R(j)$ of an atom per unit time is defined by

$$I(j) = C_{ion}(j,T)n_e(i), \quad R(j) = C_{rec}(j,T)n_e(i), \tag{5.53}$$

where j is number of j-th ionisation state. $C_{ion}(j,T)$ and $C_{rec}(j,T)$ are the ionisation and recombination coefficients which depend on the electron temperature, respectively. The rates used in this work are identical to those in Patnaude et al. (2009) and reference therein. The ion fraction X_j^{t+1} in each Lagrangian gas element is calculated by

$$\mathrm{X}_j^{t+1} = dtI_{j-1}\mathrm{X}_{j-1}^t + (1 - dt(I_j + R_j))\mathrm{X}_j^t + dtR_{j+1}\mathrm{X}_{j+1}^t, \tag{5.54}$$

where $t+1$ means the next time step. The first term in the right hand side refers to the ionisation from state $j-1$ and the last term means the recombination from the ion state of

$j+1$. The second term to the decrease of this ion with state j after dt.

In order to solve the equation (5.55), we adopt the implicit method of Crank-Nicolson scheme, since the implicit method keeps a numerical stability. The ion fraction is described by

$$-I_{j-1}\mathrm{X}_{j-1}^{t+1} + (1 + dt(I_j + R_j))\mathrm{X}_j^{t+1} - R_{j+1}\mathrm{X}_{j+1}^{t+1} = \mathrm{X}_j^t. \tag{5.55}$$

We can obtain the new ion fraction by solving the tridiagonal matrix as follows:

$$\begin{pmatrix} \beta_1 & \gamma_1 & & & \\ \alpha_2 & \beta_2 & \gamma_2 & & \\ & & \ddots & & \\ & & \alpha_{j-1} & \beta_{j-1} & \gamma_{j-1} \\ & & & \alpha_j & \beta_j \end{pmatrix} \begin{pmatrix} \mathrm{X}_1^{t+1} \\ \mathrm{X}_2^{t+1} \\ \vdots \\ \mathrm{X}_{j-1}^{t+1} \\ \mathrm{X}_j^{t+1} \end{pmatrix} = \begin{pmatrix} \mathrm{X}_1^t \\ \mathrm{X}_2^t \\ \vdots \\ \mathrm{X}_{j-1}^t \\ \mathrm{X}_j^t \end{pmatrix}$$

where

$$\alpha_{j-1} = -I_{j-1}dt, \tag{5.56}$$

$$\beta_j = 1 + (I_j + R_j)dt, \tag{5.57}$$

$$\gamma_{j+1} = -R_{j+1}dt. \tag{5.58}$$

We perform a test calculation for a simple case of $n_e = 1$ cm^{-3}. Figure 5.7 shows results of ion fractions of S with electron temperatures of $10^{4.3}$ K and 10^8 K. In the case of $T_e = 10^{4.3}$ K, the ionisation state reaches the CIE at a few 10^{12} s, where the initial ion state of S is only bare, while S is neutral in the case of $T_e = 10^8$ K. In both cases, ions become the CIE state at $\sim 10^{12}$ s that agrees with the ionisation equilibrium timescale of $\sim 10^{12}$ s (Masai 1994).

5.2.5 Simulation test for a young SNR

In order to verify our code for young SNRs, we compared our results with the CR-hydro-NEI code (Ellison et al. 2007, Patnaude et al. 2009; 2010, Ellison et al. 2010, Lee et al. 2012; 2013; 2014, Slane et al. 2014). Thanks to the data which they provided us, we can perform calculations starting from the same initial conditions and compare the results. Figures 5.8, 5.9 and 5.10 show side by side the results simulated by the CR-hydro-NEI code and our code without including radiative cooling. We simulate a CC SN of model s25D with the ISM density of 1 cm^{-3}. The velocity and mass loss rate of a wind are 20 km s^{-1} and 10^{-5} M$_\odot$ yr^{-1}, respectively. Profiles of density, velocity and temperatures at 500 yr simulated by our code are consistent with the CR-hydro-NEI code. A difference of the density around 1.75 pc is due to the effect of a gaussian smoothing. The position of the FS and RS at 500 yr are ~ 2.5 pc

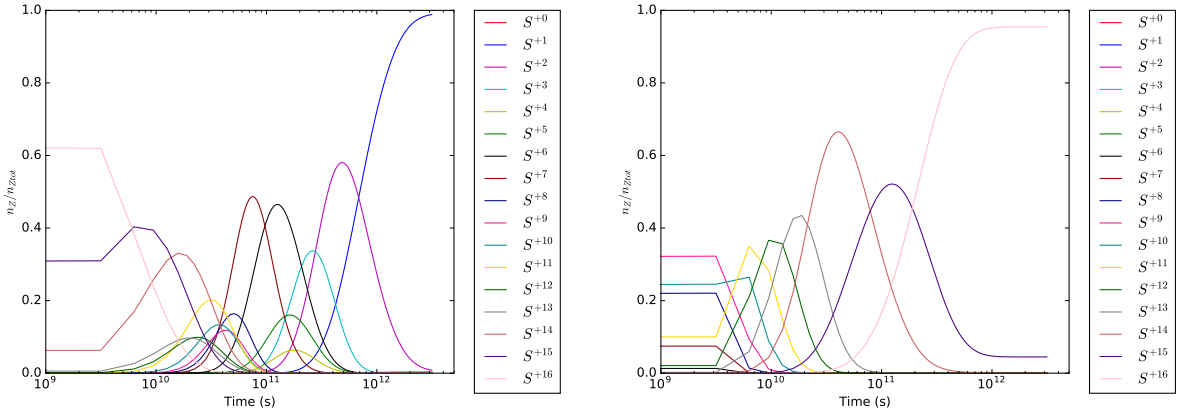

Figure 5.7: The time evolution of the ion fraction of S with electron temperatures of $10^{4.3}$ K (left) and 10^8 K (right). The ionisation state in both cases reaches the CIE at a few 10^{12} s that is consistent with the ionisation equilibrium timescales.

and ~ 2.0 pc in both simulations. Our code reproduces the results of the CR-hydro-NEI code faithfully. Results of simulations and verifications for evolved SNRs will be discussed in the next chapter.

5.3 Spectral synthesiser

The spectral generator provides X-ray spectra and images from the output of the hydrodynamics code using AtomDB. The structure of our spectral generator is shown in Figure 5.11. This code requires as input the radius of Lagrangian grid, grid width, electron temperature, densities of electrons and ions, and ion fractions of each element, which are obtained from the output file of the hydrodynamics code. In this study, we calculate the emission from 13 elements (H, He, C, N, O, Ne, Mg, Si, S, Ar, Ca, Fe, Ni: 181 ionisation states) and other ions are ignored.

For calculating the X-ray spectra of an optically-thin plasma, atomic transition rates and energies of the ions are needed. AtomDB is an atomic database for modelling X-ray spectra from hot, collisionally ionised plasma with $10^4 \leq T_e \leq 10^9$ K (Smith & Brickhouse 2001). AtomDB provides two FITS files containing a line list and compressed continua (Smith & Brickhouse 2001). The first, line list file, has information on the wavelength λ (Å), the line emissivity ϵ (photons cm^3 s^{-1}), the atomic number Z of the element, the ion stage, and the transition level (upper and lower), and so on grouped by the electron temperature. The ion stage is described as 1 for neutral atom, 2 for singly-ionised and so on. Thus, we can obtain the energies and the emissivities of all lines emitted from an ion at a given temperature. The compressed continua file contains the atomic number, the ion stage, and 4 vectors. One is a

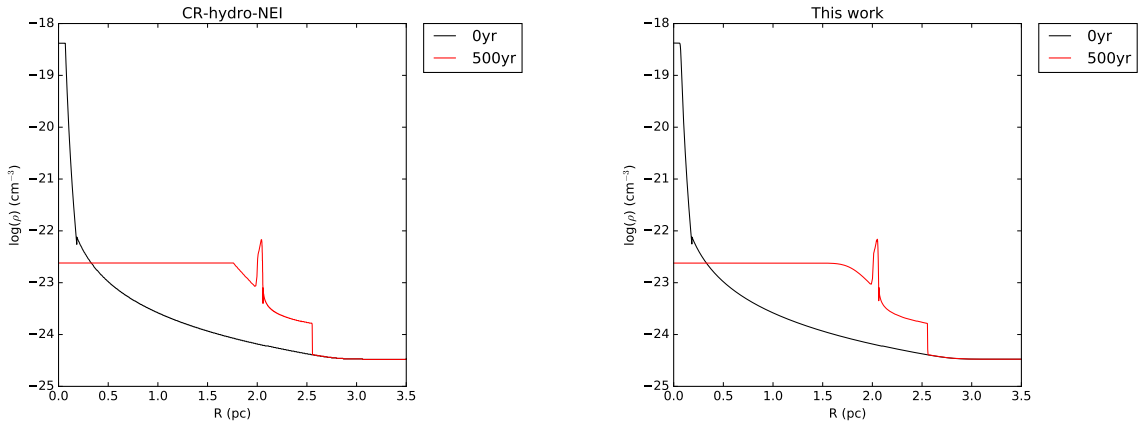

Figure 5.8: Density simulated by the CR-hydro-NEI code (left) and our code (right).

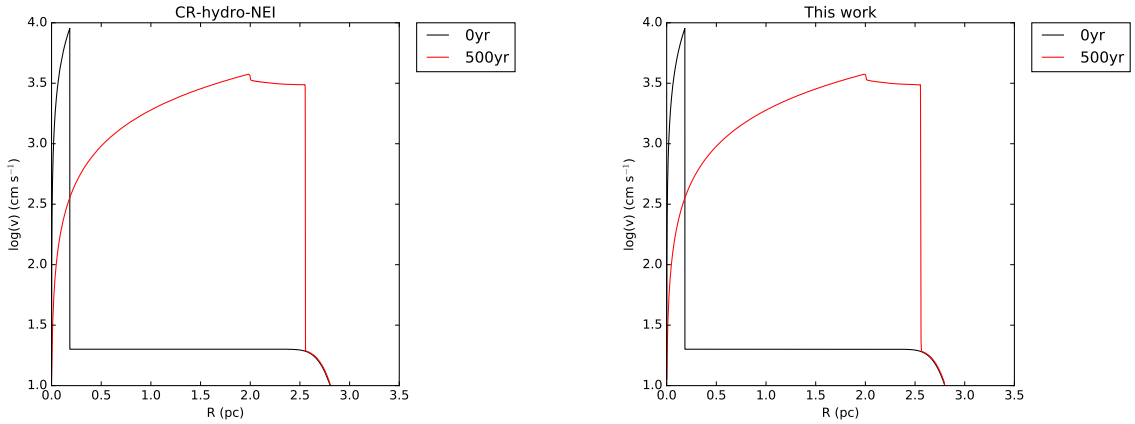

Figure 5.9: Velocity simulated by the CR-hydro-NEI code (left) and our code (right).

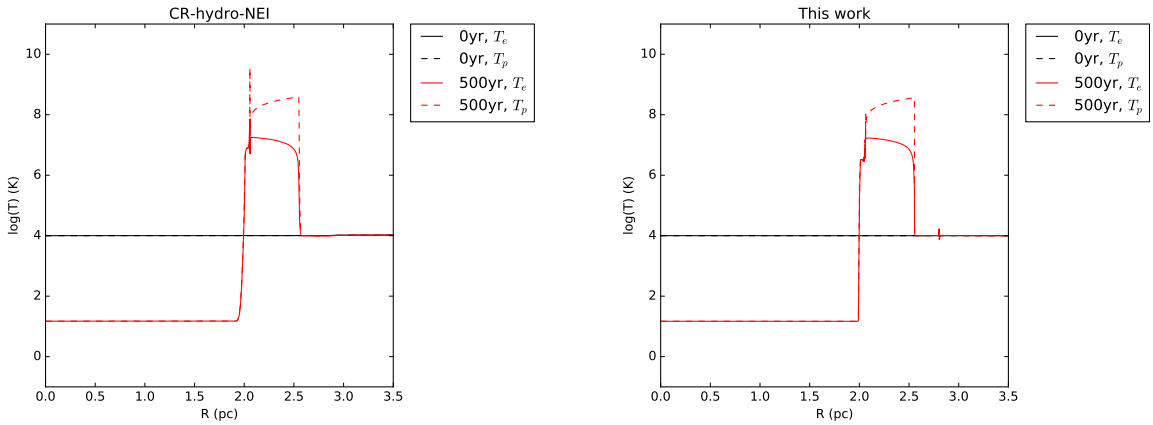

Figure 5.10: Temperatures of protons and electrons simulated by the CR-hydro-NEI code (left) and our code (right).

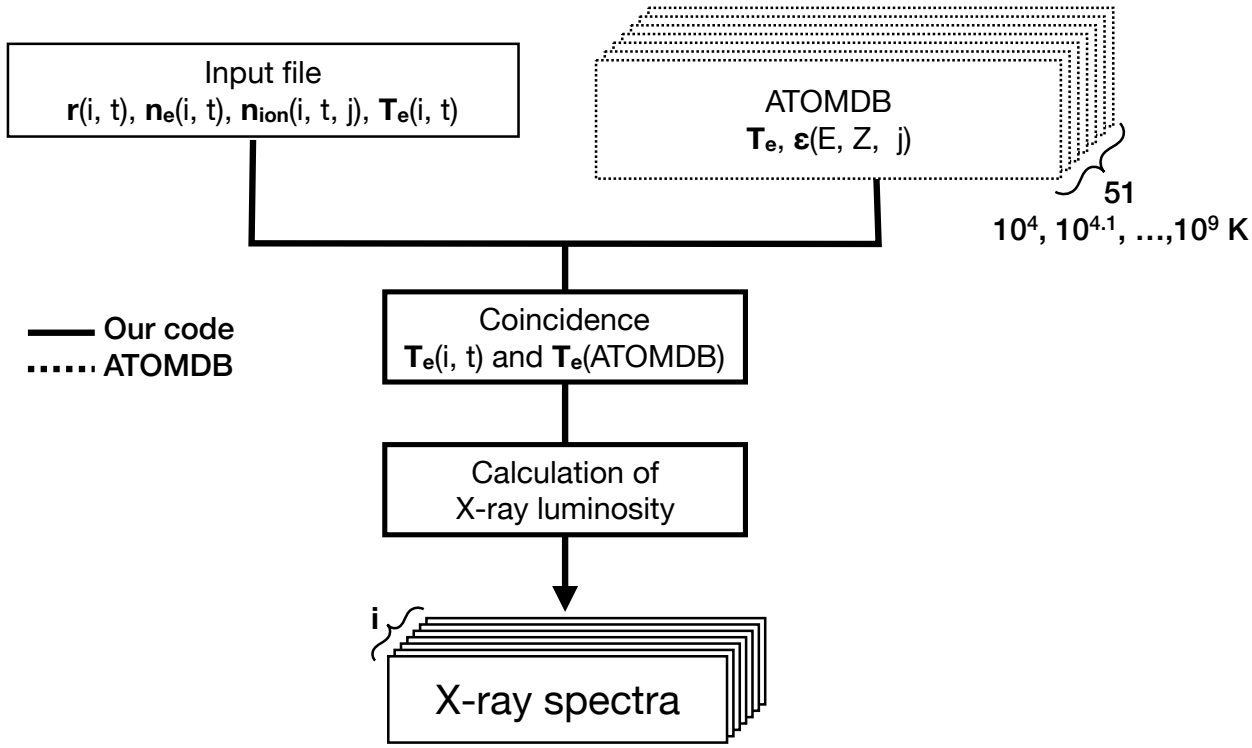

Figure 5.11: Outline of our spectral generator.

vector containing the energies (keV) where the continuum value is calculated, and the second vector is the continuum level (photons cm^3 s^{-1} keV^{-1}) at the corresponding energies. The third and fourth vectors are the energy (keV) and pseudo-continuum (photons cm^3 s^{-1} keV^{-1}). The pseudo-continuum consists of lines which are too weak to list individually and are stored here so that they may contribute to the total spectrum without taking up too much space. We use the NEI database in the AtomDB version 3.0.8 released on February 12, 2017.

Using the output file from the hydrodynamics code at the age of t and the AtomDB database, we calculate the total emission from 13 elements and generate the X-ray spectra and images. At first, a data list in AtomDB which matches with the temperature $T_e(i)$ is chosen at "Coincidence" as illustrated in Figure 5.11. In the next the part, the total emission is calculated for all ions of the 13 elements considered. The emission $I_{j\to k}$ from a line is given by

$$I_{j\to k} = n_j A_{j\to k} \tag{5.59}$$

where n_j is the number of ions of element Z, ion $z1$, in state j. $A_{j\to k}$ means the Einstein A

coefficient of spontaneous emission (s^{-1}). n_j is calculated by

$$n_j = \frac{n_j}{n_{z1}} \frac{n_{z1}}{n_Z} \frac{n_Z}{n_H} \frac{n_H}{n_e} n_e. \tag{5.60}$$

where n_j/n_{z1} is the fraction of the ion population in level j and N_{z1}/N_Z is the ion fraction. The elemental abundance n_Z/n_H in AtomDB is used from Anders & Grevesse (1989). $A_{j\to k}\frac{n_j}{n_{z1}}$ at density of the block is provided as $\epsilon_{j\to k}$ (photons cm^3 s^{-1}) from the database. Thus, we can obtain the total emission from a grid i by

$$\begin{aligned} I(E,i) &= \sum_{Z,z1,j} I_{j\to k}(i), & (5.61)\\ &= \sum_{Z,z1,j} \frac{\epsilon_{j\to k}(E,Z,z1,j)}{Abd_Z} \frac{n_{z1}(i)}{n_Z(i)} \frac{n_Z(i)}{n_H(i)} n_H(i) n_e(i), & (5.62)\\ &= N_e(i) \sum_{Z,z1,j} \frac{\epsilon_{j\to k}(E,Z,z1)}{Abd_Z} n_{z1}(i), & (5.63) \end{aligned}$$

where Abd_Z is the elemental abundance in Anders & Grevesse (1989). $n_{z1}(i)$, $n_Z(i)$, $n_H(i)$ and $n_e(i)$ are data from our simulations. Then, the photon flux F_X (photons cm^{-2} s^{-1}) can be calculated as

$$F_X(E,i) = \frac{1}{4\pi D^2} \int I(E,i) dV(i). \tag{5.64}$$

X-ray spectra in an energy range of 0.5–10.0 keV are generated by calculating the flux in each energy bin.

Figure 5.12 shows examples of model X-ray spectra. We calculate the X-ray spectrum at every age and grid position. Our code provides the time evolution of the X-ray spectra at every 100 yr temporal step. We also need to note that the observed spectra are projected along the line of sight.

The differences between previous models and this work are summarised in Table 5.1. Calculation of ion states is implemented in all of the models. Since previous studies of SNR simulations do not include a process of radiative cooling, their applications are limited to simulation of young SNRs. A recombining plasma model implemented in XSPEC (RNEI model) assumes that a plasma in collisional equilibrium is cooled suddenly down to T_e and the product of $n_e t$. RNEI is not suitable for study how progenitor models and ambient gas affect the time evolution of plasma. Therefore, our code is useful for simulations of conditions of plasma in evolved SNRs.

Table 5.1: The difference between previous models and this work

	Itoh & Masai (1989)	Lee et al. (2012)	RNEI model*	This work
Hydrodynamics	◯	◯	×	◯
Coulomb interaction	◯	◯	×	◯
Radiative cooling	×	×	×	◯
$T_e(t)$	◯	◯	×†	◯
$n_e(t)$	◯	◯	◯‡	◯
Target age	Young	Young	All	All
Estimation from spectra				
Age	-	◯	◯‡	◯
Progenitor	-	◯	×	◯
Ambient gas	-	◯	×	◯

* RNEI model is a recombining plasma model in XSPEC.

† The electron temperature of RNEI model in XSPEC is independent of time.

‡ They are only available as the form of $n_e t$.

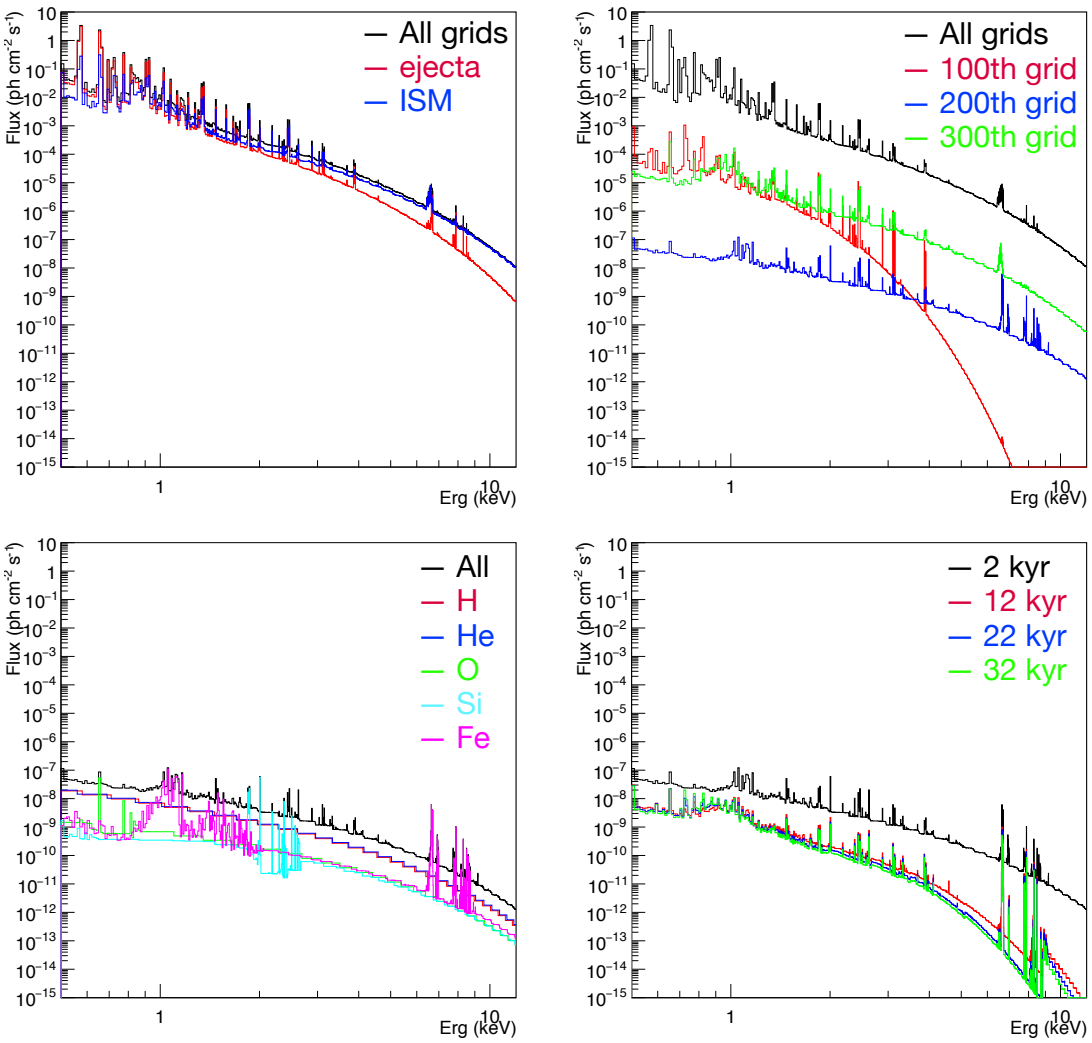

Figure 5.12: Example of X-ray spectra. The top left panel shows the spectra from all grids (black), ejecta (red) and ISM (blue) at 2 kyr. The top right panel shows the spectra from all grids (black), 100th (red), 200th (blue) and 300th (green) grid at 2 kyr. The bottom left panel shows the spectra from all elements (black), H (red), He (blue), O (green), Si (cyan) and Fe (magenta) in the 200th grid at 2 kyr. The bottom right panel shows the spectra from the 200th grid at 2 kyr (black), 12 kyr (red), 22 kyr (blue) and 32 kyr (green).

Chapter 6

Characteristic observables calculated from the simulations

In order to find the condition of the surrounding environment which explains the plasma state observed in X-rays, we need common indicators that enable us to compare results of the simulations with observations. The plasma state is described by the electron temperature and the ion fractions. Our simulation give us this information at every grid position and age. However, an observed X-ray spectrum is a result of integration along the line of sight. Therefore, we have to estimate correct values integrated along the line of sight from the simulation data. In addition to the electron temperature, we introduce the concept of the ionising temperature adopted as an indicator.

6.1 Electron temperature and ionisation temperature

We define two types of temperature from observational data: One is the electron temperature which is determined from the X-ray continuum. The other is the ionisation temperature which is used as an indicator of describing the ionisation state of the X-ray emitting plasma.

The electron temperature can be determined directly by spectral fitting with a thermal plasma model such as APEC and RNEI included in the XSPEC fitting package. APEC and RNEI are models describing thermal plasma in the XSPEC code. The APEC model is an emission spectrum from CIE plasma calculated based on AtomDB. The free parameters of this model are given by the electron temperature (kT_e), metal abundances and the volume emission measure (VEM). On the other hand, the RNEI model is an emission spectrum from NEI plasma calculated by the AtomDB. The RNEI model has kT_e, metal abundances, the VEM, the initial ionisation temperature (kT_{init}) which measures the initial ionisation state, and the non-equilibrium timescale ($n_e t$) as parameters. The RNEI model assumes a simplified condition

in which the ionisation state vary with $n_e t$ under that constant kT_e. If kT_{init} is smaller than kT_e, the plasma is in an ionising state, while the case of $kT_{init} > kT_e$ corresponds to recombining plasma. The electron temperature is calculated from the shape of the Bremsstrahlung component. Using these models, the spectral analysis enables us to estimate the electron temperature. We should note that the observed X-ray spectra are integrated along the line of sight. Therefore, the electron temperature is considered to be a temperature averaged over the line of sight.

Fitting the RNEI model to an observed spectra, we can estimate the ionisation temperature of each element. The ionisation temperature is the equivalent electron temperature that reproduce the observed ion fractions in a CIE plasma; when the plasma is out of equilibrium, this temperature can be different from the true electron temperature. For example, if the ion fractions of S XIV and S XV are ∼90% and ∼10%, kT_Z is 0.8 keV as you can see from the dash lines in figure 6.1, which shows the ion fractions of S in a CIE plasma (Arnaud & Rothenflug 1985). Since lines of sulphur is detected in many SNRs and ion fraction of S at $kT_e \sim 2$ keV distributes around S XV and S XVI, S is appropriate for the estimation of the ionisation temperature from 0.1 keV to 10 keV. The ionisation temperature obtained from observations also distributes in 0.1 keV to 10 keV (Kawasaki et al. 2005). Therefore, we use the ratio of S XV and S XVI in this work.

6.2 Timescale of interactions

To study the time evolution of the electron and ionisation temperatures, it is important to understand what the dominant physical effect is on these temperatures. Considerable causes of electron heating and cooling include the Coulomb interaction, radiative cooling, adiabatic expansion and adiabatic compression. The time evolution of the ionisation temperature is related to the ionisation and recombination timescales.

We consider timescales of the Coulomb interaction, radiative cooling, ionisation and recombination. In this calculation, we assume that the proton and electron densities are the same ($n_p = n_e$). The evolution of the electron temperature by the Coulomb interaction is explained in §5.2.3. From equation (5.36), the equilibration timescale (τ_{eq}) of the Coulomb interaction is

$$\tau_{eq} = \frac{3}{296\sqrt{2\pi}} \frac{m_e m_p}{n_p e^4} \left(\frac{kT_p}{m_p} + \frac{kT_e}{m_e} \right)^{\frac{3}{2}}, \tag{6.1}$$

where logΛ is fixed at 37 which is a typical value for SNR plasmas. τ_{eq} is longer when the ratio of the proton temperature to the electron temperature (T_p/T_e) is larger. τ_{eq} is in inverse proportion to n_p. As explained §5.2.3, the timescale of the radiative cooling (τ_{cool}) is described

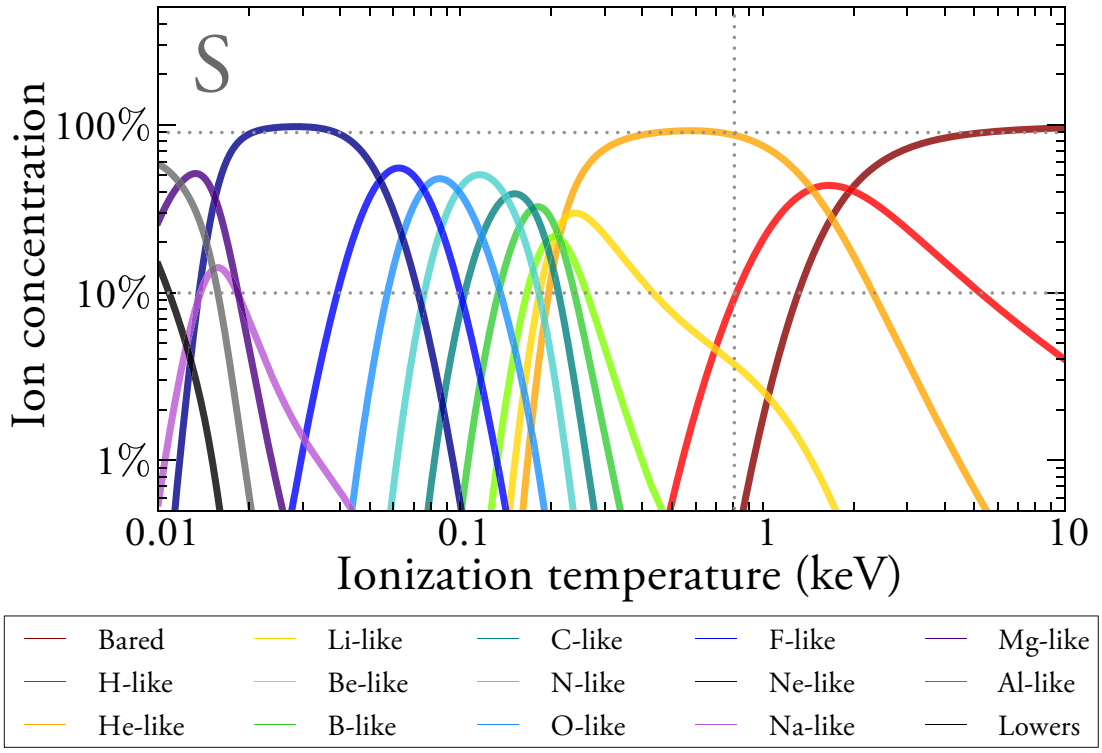

Figure 6.1: Ionic fraction as a function of the ionisation temperature for S from Arnaud & Rothenflug (1985). The figure is taken from Sawada (2011). Grey dashed lines indicate an ion concentration of 10% and 90% and the temperature of 0.8 keV.

as

$$\tau_{cool} = \frac{3k}{2\Lambda(T_e)n_p}T_e. \tag{6.2}$$

The timescale to reach an ionisation equilibrium for an element with atomic number Z is calculated by

$$\tau_{ion-eq} = n_e^{-1}\sum_{j=0}^{Z}(I_j + R_j)^{-1}, \tag{6.3}$$

where I_j and R_j are rates of the ionisation and recombination for an ion state j of an element Z (Masai 1994). Since T_Z is estimated from S (Z = 16) in our simulation, τ_{ion} and τ_{rec} are

described as

$$\tau_{ion} = \sum_{j=0}^{16} \frac{1}{n_e I_j}, \tag{6.4}$$

$$\tau_{rec} = \sum_{j=0}^{16} \frac{1}{n_e R_j}. \tag{6.5}$$

The typical $n_e \tau_{ion-eq}$ in SNR plasmas is $\sim 10^{12}$ cm^{-3}s (Masai 1994).

Figure 6.2 shows the timescales of the Coulomb interaction, radiative cooling, ionisation, and recombination as a function of temperature , where we assume the densities to be 1 cm^{-3}. τ_{eq} (black line) is calculated assuming that T_p/T_e is the ratio of the proton mass to the electron mass (m_p/m_e) which is the ratio just after a shock (solid). Electrons achieve the Maxwell distribution in very short time. The radiative cooling process at low electron temperature ($<$ 0.1 keV) is more effective than that at high electron temperature (red line). The ionisation equilibrium timescale is $\sim 10^4$ yr. Since these timescales are in proportion to $1/n_p$ or $1/n_e$, these timescales become shorter in a dense gas ($n_e > 1$ cm^{-3}).

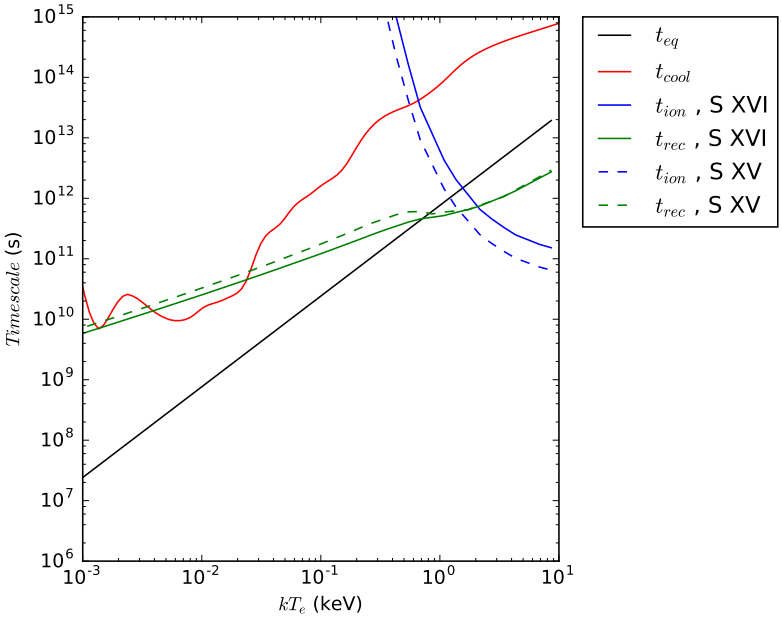

Figure 6.2: Timescales of Coulomb interaction, cooling, ionising and recombining.

6.3 Simulation results of an evolved SNR

In this section we show the simulation results of CC SNR with the ISM density of 1.0 cm^{-3} and describe the dynamics of the SNR. Figure 6.3 shows the initial condition of a simulation. Since the recombining plasma is observed in evolved CC SNRs, we adopt an ejecta model of s25D developed by Rauscher et al. (2002), which corresponds to a 25 $M_\odot$ main sequence progenitor with initially solar metallicity. The mass of the ejecta (M_{ej}) is 12.3 $M_\odot$ with the explosion energy (E_{SN}) of 1.2 $\times$ 10^{51} erg. The mass loss ratio ($\dot{M}_{CSM}$) and velocity (v_{CSM}) of the CSM are 10^{-5} $M_\odot$ yr^{-1} and 20 km s^{-1}, respectively. We assume that the ISM density is 1 cm^{-3} which is a typical value for the ISM. Temperatures of the ejecta, CSM and ISM are 10^4 K at which X-rays is not emitted.

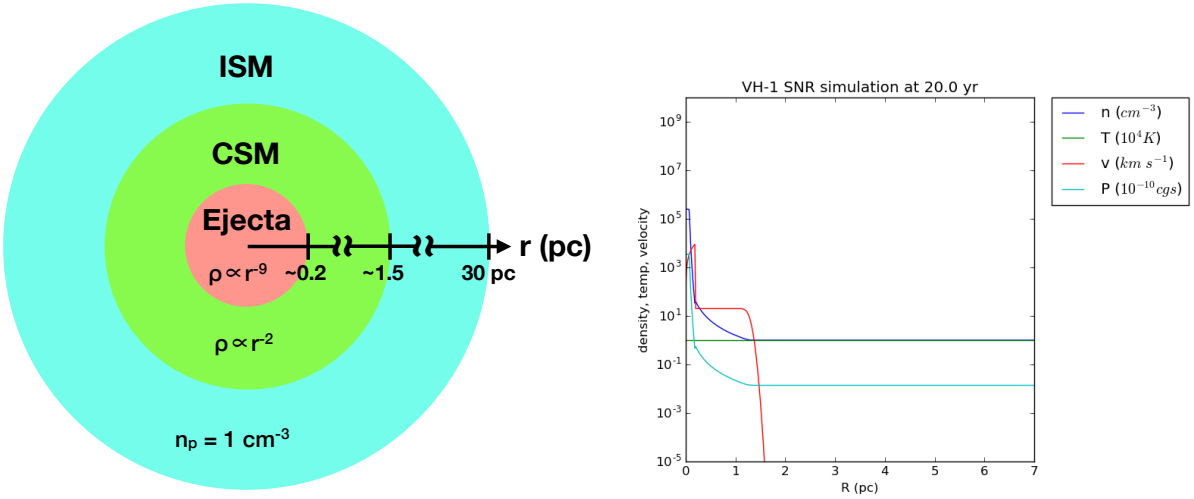

Figure 6.3: Initial condition of a CC SNR simulation with n_{ISM} of 1 cm^{-3}. $\dot{M}_{CSM}$ and v_{CSM} are 10^{-5} $M_\odot$ yr^{-1} and 20 km s^{-1}.

As results of the simulation, we obtain the time evolution of the density, velocity and temperatures of electrons and ions as shown in figure 6.4. Two shock waves are created at the contact discontinuity (CD) between the ejecta and CSM and they advance toward the inside and the outside of the SNR. The shock wave moving into the CSM and ISM is called the forward shock (FS) and can be seen as a density jump in the cyan line at 5 pc in figure 6.4. The reverse shock (RS), which appears as a density jump in the cyan line at 4 pc, goes toward the inside of the SNR and finally arrives at the centre at the age of $\sim 8 \times 10^3$ yr, which is consistent with other works. The density around the CD, where the ejecta is shocked at an early phase, becomes high because the RS moves in the denser ejecta. Then, electrons reach the thermal equilibrium in a short time because of their high density. Since the temperature of 10^5–10^6 K is severely affected by radiative cooling, the temperature of the ejecta around the

CD decreases and matter is compressed more significantly. The same situation occurs behind the FS at 4×10^4 yr. Due to decreasing of the shock speed, the post-shock temperature at the FS becomes low enough such that radiative cooling is extremely effective. The Coulomb interaction is effective in gas elements of high densities, therefore, temperatures of electrons and ions equilibrate in a short time. Because of the lack of convection in the 1-D simulation, ejecta is pushed back by the ISM at $\sim 5 \times 10^3$ yr and, consequently, the velocity of the shocked ejecta changes to a minus sign.

Figure 6.5 shows the velocity of the FS and RS and their positions. As we described in §2.2.1, the velocity of the FS decreases as shown by the blue line in figure 6.5 (left). Since the RS moves through the dense ejecta ($\propto r^{-9}$) at the young age, its velocity decreases in a short time, e.g. $t_{eq} \sim 300$ yr ($n_p = 1$, $kT_e = 0.1$). After that, the RS is accelerated when the RS has completely ascended the steep outer envelope of the ejecta. Though the RS propagates outwards in the observer frame, the RS moves to inside when the ejecta is pushed back. The RS reaches the centre of the SNR at ~ 8000 yr as shown by the behaviour of the green line in figure 6.5 (right).

In order to investigate the X-ray emission, let us consider a snapshot at an age of 5×10^3 yr. Figure 6.6 shows the profile of the densities and temperatures of the protons and electrons, velocity, pressure, and X-ray spectra from a subset of grids at 5×10^3 yr. Coloured spectra in the right panel of Figure 6.6 are X-ray spectra at grid points indicated by arrows in the left panel (30th, 60th, 100th, 201st, 300th, 450th grids). The magenta arrow shows the position of the ejecta at the CD. The structure of spectra from each grid is clearly different and it implies a difference of the temperature and ionisation state. Focussing on the green spectrum from a gas element through which the shock swept past at an early phase, we can see the RRC component at ~ 2.4 keV and ~ 3.2 keV, which comes from the He-like Si and He-like S, respectively. An edge at ~ 8.8 keV in the spectrum from the CD is the RRC from He-like Fe. Although we can see the RRC component in the spectra of the 100th and 200th grid points, the RRC component does not appear in other spectra including the integrated spectrum. Therefore, the RRC observed in X-ray spectra is considered to come from around the CD where elements are shocked at an early phase and ionised to a higher state.

6.4 Temperatures derived from the simulation results

The ionisation temperature is estimated from the ion fractions described in §6.1. However, there are multiple choices of ions and elements to determine the ionisation temperature. We use a ratio between ion fractions of S XV and S XVI. We calculate the ratio of $n_{\mathrm{S\ XV}} I_{\mathrm{S\ XV}}(T_e)$ to $n_{\mathrm{S\ XVI}} R_{\mathrm{S\ XVI}}(T_e)$ at $10^{3.8}$–10^8 K every $10^{0.1}$ K, where I and R are rates of the ionisation and recombination. T_Z is considered to be the temperature for which the ratio is closest

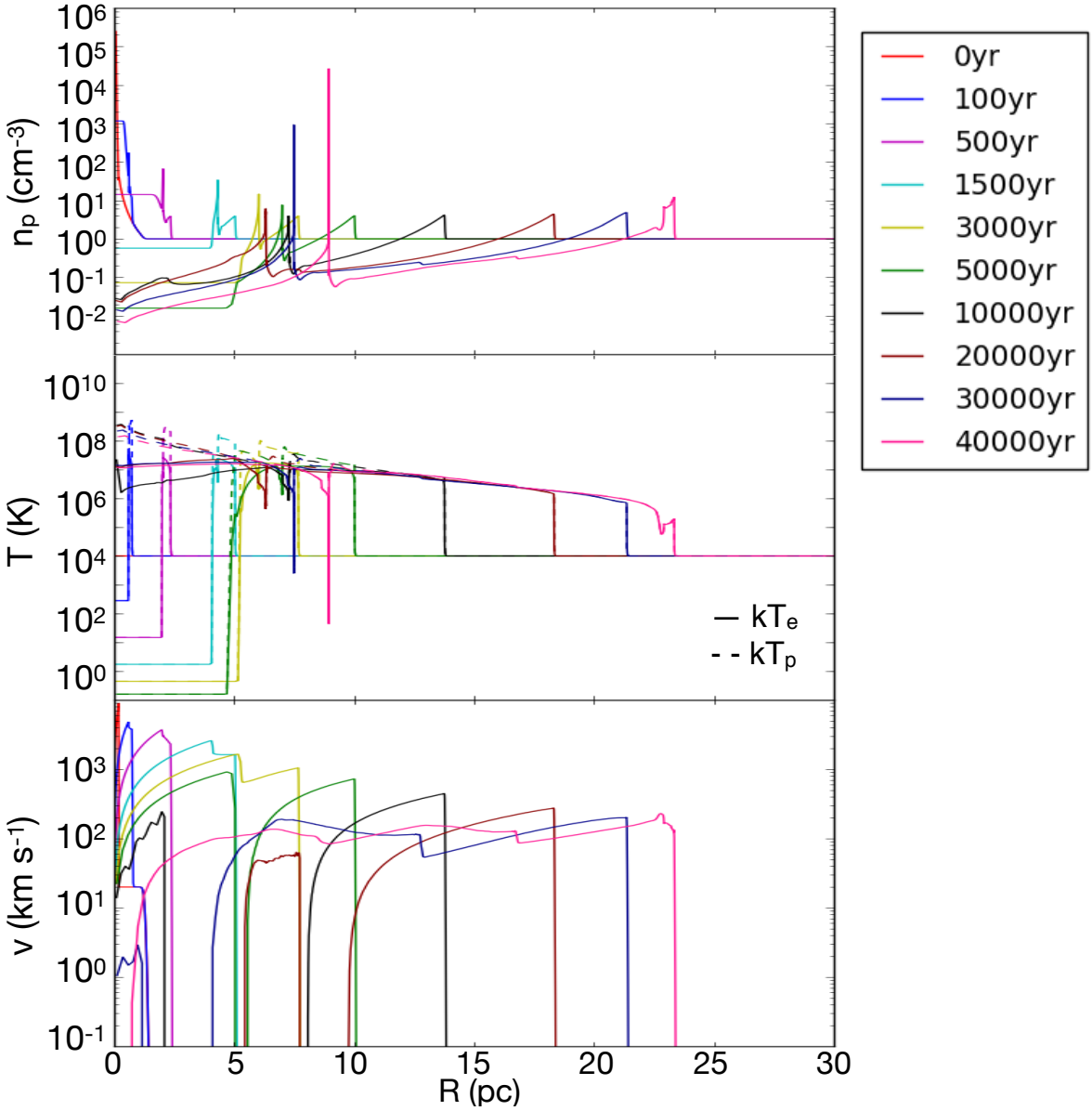

Figure 6.4: Density, velocity and temperatures of electrons and protons at the age of 0, 1×10^2, 5×10^2, 1.5×10^3, 3×10^3, 1×10^4, 2×10^4, 3×10^4, 4×10^4 yr. The post-shock temperature at the FS becomes low at 4×10^4 yr because radiative cooling is extremely effective.

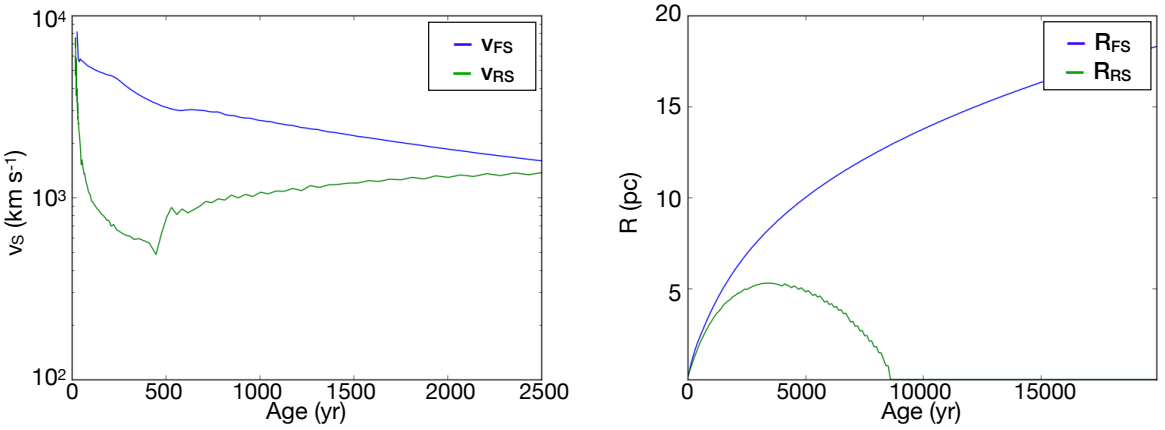

Figure 6.5: The time profile of shock velocities (left) and radius (right) of the FS (blue) and RS (green). The velocity of the RS decreases in a short time due to the RS moves through the dense ejecta, which reaches the centre of the SNR at $\sim$ 8000 yr.

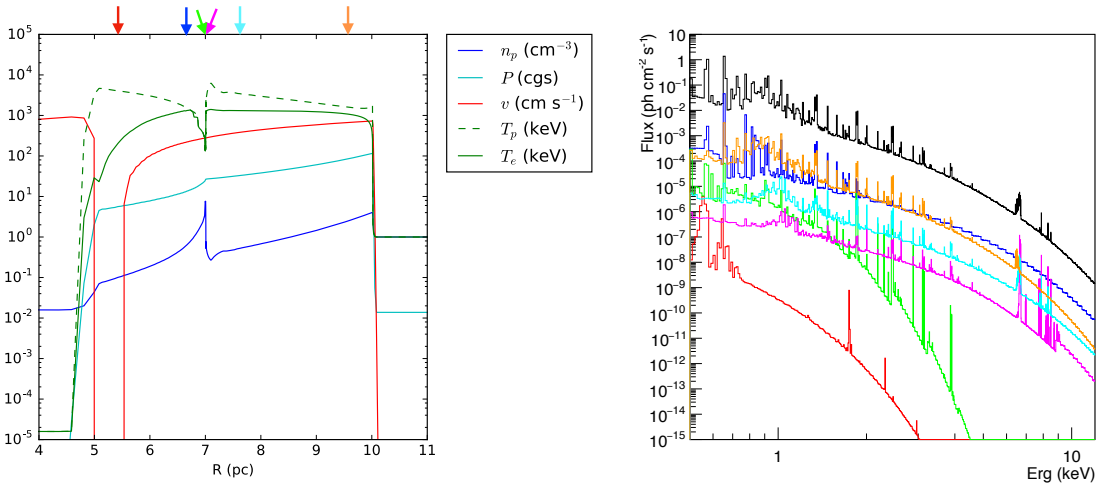

Figure 6.6: The profile of n_p, T_p, v, P, n_e, T_e (left) and X-ray spectra (right) at 500 yr. Black spectrum is the total X-ray spectrum of all grids. Red, blue, green, magenta and cyan show spectra at grids shown as arrows in the left panel. The RRC components are seen at $\sim$ 2.4 keV and $\sim$ 3.2 keV (He-like Si and He-like S) in the green spectrum, though they disappear in the total (black).

to 1. Figure 6.7 shows the ion fraction of S, the electron temperature and the ionisation temperature estimated from $n_{\rm S\ XV}$ and $n_{\rm S\ XVI}$. For example, the ion fraction of $n_{\rm S\ XV}$ and $n_{\rm S\ XVI}$ at ~ 8 pc are $\sim$0.8 and $\sim$0.1 (Figurer 6.7, left), then T_Z is determined to be $\sim$0.8 keV. This result is consistent with Arnaud & Rothenflug (1985) as shown in figure 6.1. The profile of temperatures are quite difference in the position. The electron temperature is higher than the ionisation temperature in most grid. However, the ionisation temperature is over the electron temperature at $\sim$7 pc where the density is highest.

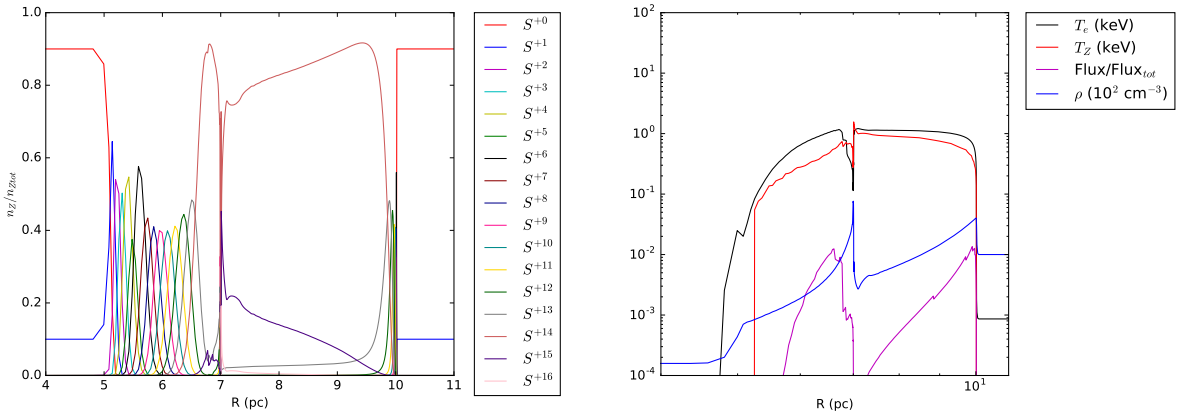

Figure 6.7: The left panel shows the ion fraction of S. The right panel shows the electron (black), ionisation (red) temperatures, the photon flux ratio (magenta), and the density ratio (blue). The outside ejecta and ISM are dominant in average temperatures.

In order to investigate what leads to various electron and ionisation temperatures, we consider their time evolution. Figure 6.8 shows the time evolution of the ionisation temperature at five grid points shown as arrows in a left panel of figure 6.6. The post-shock temperature of the electron rapidly increases after the shock in all grids. After the shock, the electron temperature increases for a while because the Coulomb interaction is effective. When the adiabatic expansion becomes dominant, the electron temperature begins to go down gradually. The electron temperature becomes lower than the ionisation temperature because of the adiabatic cooling which happens at a faster rate than the transition of the ion state ($t_{rec} \sim 10^5$ yr) as shown in Figure 6.9. After that, the ionisation temperature begins to decrease so as to reach the ionisation equilibrium state. A rise of temperatures at $\sim$ 300 yr occurs due to the break out of the FS from the CSM to the ISM. Because the radiative cooling is extremely effective for 10^5–10^6 K electrons, the electron temperature as depicted by the green line decreases rapidly at 20–30 kyr. Rises of 0.1–1.0 keV around 1.0–1.1×10^4 yr in each grid occurs by the RS which goes through the centre of the SNR from the other way.

For comparison with observations, we have to calculate an average of the electron and

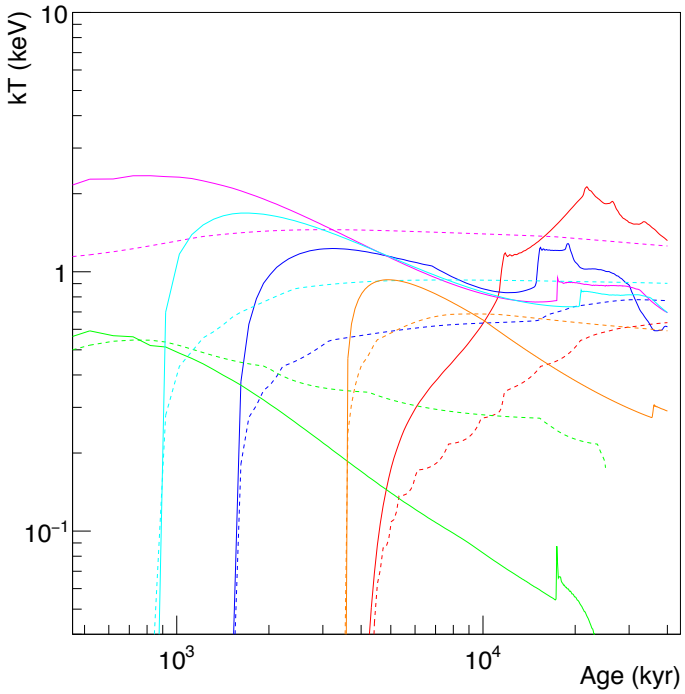

Figure 6.8: The time evolution of electron (solid) and ionisation (dash) temperatures at grids indicated by arrows in as a left panel of Figure 6.6. The post-shock temperature of the electron rapidly increases after the shock in all grids. The electron temperature becomes lower than the ionisation temperature because of adiabatic and radiative cooling, then the RP is produced.

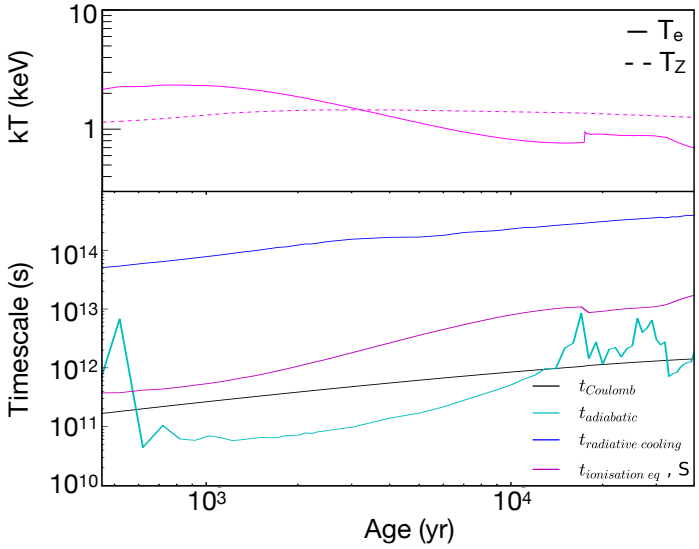

Figure 6.9: The top panel shows the time evolution of electron (solid) and ionisation (dash) temperatures on the edge of ejecta (201st grid). The lower panel shows the timescales of Coulomb interaction, adiabatic expansion, radiative cooling and ionisation equilibrium. The timescale of adiabatic expansion is shorter than the ionisation equilibrium timescale, the electron temperature becomes lower than the ionisation temperature.

ionisation temperatures because X-ray observations give us only a temperature and a pattern of ion fractions estimated from an X-ray spectrum integrated along the line of sight. The volume emission measure would be a good indicator for the calculation of weighted averages of T_e and T_Z. The electron temperature obtained from spectra is, however, estimated from the X-ray emission. Thus, we perform this averaging with a weight of the photon flux (ph cm^{-2} s^{-1}) in 0.5–10.0 keV emitted from each grid shown as a magenta line in figure 6.7. The electron and ionisation temperatures integrated from the RS to the FS is 0.87 keV and 0.55 keV. The average temperatures from the RS to the CD are Te = 0.93 keV and Tz = 0.52 keV, while those from the CD to the FS are Te = 0.86 keV and Tz = 0.55 keV. Therefore, the plasma at 5×10^3 yr is ionising plasma and the ISM is dominant.

Before mentioning about the time evolution of the temperatures averaged in the whole SNR, we describe their behaviour in the ejecta (RS–CD) and the ISM (CD–FS) since their time evolutions are extremely different between the ejecta and the ISM. Figure 6.10 shows T_e and T_Z in the CD–FS weighted by the photon flux in 0.5–10.0 keV as a function of age, and the ratio of T_Z to T_e. The electron temperature and ionisation temperature downstream of the shock decrease gradually due to the slowing down of the shock speed (see figure 6.5). Since the density at the FS is largest in the CD–FS as shown in figure 6.11, the temperatures around the FS are dominant. Thus, the averages of the electron temperature and the ionisation temperature decline in the FS–CD. In addition, the shocked ISM cools by adiabatic expansion. An increase of the temperatures at ∼300 yr is caused by the breakout of the FS through the CSM to the ISM described in the previous section. The ionisation temperature becomes higher than the electron temperature at $\sim 1.2 \times 10^4$ yr. The increase at t$\sim 3 \times 10^4$ is occurs because of the reduction of the photon flux at the FS where radiative cooling is dominant. Although the ionisation temperatures decrease due to the recombination, T_Z/T_e increases continuously because the electron temperature decreases faster than the ionisation temperature by adiabatic expansion and radiative cooling.

The electron and ionisation temperatures in the RS–CD have a more complex behaviour than that in the CD–FS. Figure 6.12 shows the electron and ionisation temperatures in the RS–CD and the ratio of the ionisation temperature to the electron temperature. At first, the electron and ionisation temperatures decrease like that in the CD–FS. However, they increase at ∼400 yr when the reverse shock is strengthened and accelerated into the ejecta. The ejecta abundance at the RS is drastically changed between 1–2 $\times 10^3$ yr, thus the dominant grids are changed. Therefore, the electron temperature rises, while the ionisation temperature goes down. After that, the electron temperature behaves similarly to that in the CD–FS. The electron temperature increases rapidly at $\sim 1.2 \times 10^4$ yr once more. The causes is the shock heating by the RS which has passed by the centre of the SNR. When the ejecta expand again (age $\sim 2 \times 10^4$ yr), the electron temperature decreases by adiabatic and radiative cooling.

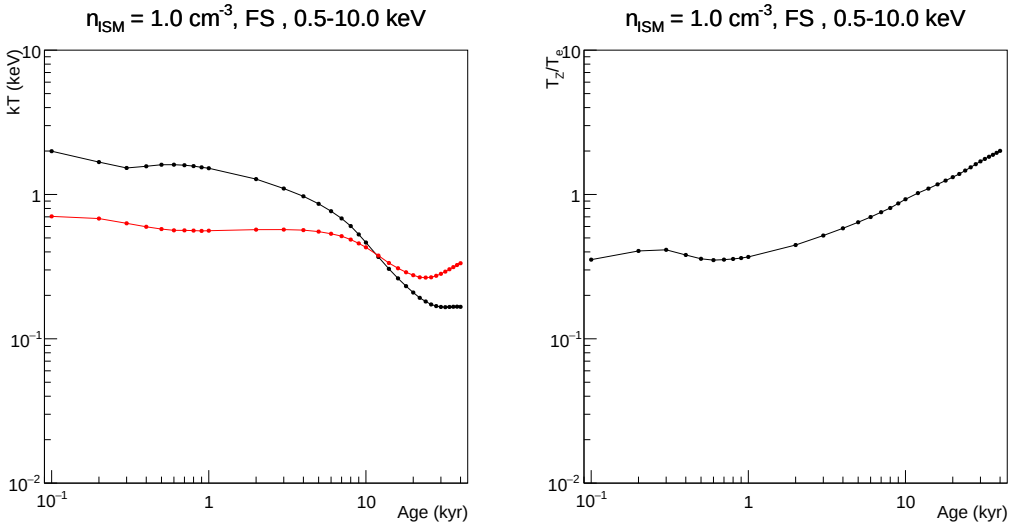

Figure 6.10: Temperatures (left) and the ratio of the ionisation temperature to the electron temperature (right) as a function of age. In the left panel, T_e (black) and T_Z (red) are integrated from the FS to the CD with the weight of the photon flux in 0.5–10 keV.

The electron and ionisation temperatures in the whole SNR is affected by the feature of the ejecta and the ISM. Figure 6.13 shows the electron and ionisation temperatures in the whole SNR (the RS–FS) and the ratio of the ionisation temperature to the electron temperature. The electron and ionisation temperatures decrease basically. The plasma transfers from the IP to the RP at 3×10^4 yr.

6.5 Dependence on density of ISM

The surrounding environment in which an SN explosion occurs should have a strong impact on the evolution of its remnant. One of the most important properties of the surroundings is the density of the ISM. In this section, we investigate how the ISM density influences the ionisation history of the SNR plasma.

As we introduced in the previous section, the ratio of the ionisation temperature to the electron temperature reflects the degree of the deviation from the CIE state. The ratio of ionisation temperature to the electron temperature depends on age as described in the previous section. In this section, we study the effect of the ISM density on T_Z/T_e. The simulated density of the ISM is 1.0 (previous section), 3.0, 10.0, and 30.0 cm^{-3}. Other parameters are fixed at the value of the simulation in the previous section.

Figure 6.14 shows the dependence of the time evolution of the temperatures in the CD–FS on the ISM density, and the ratio of the ionisation temperature to the electron temperature. The

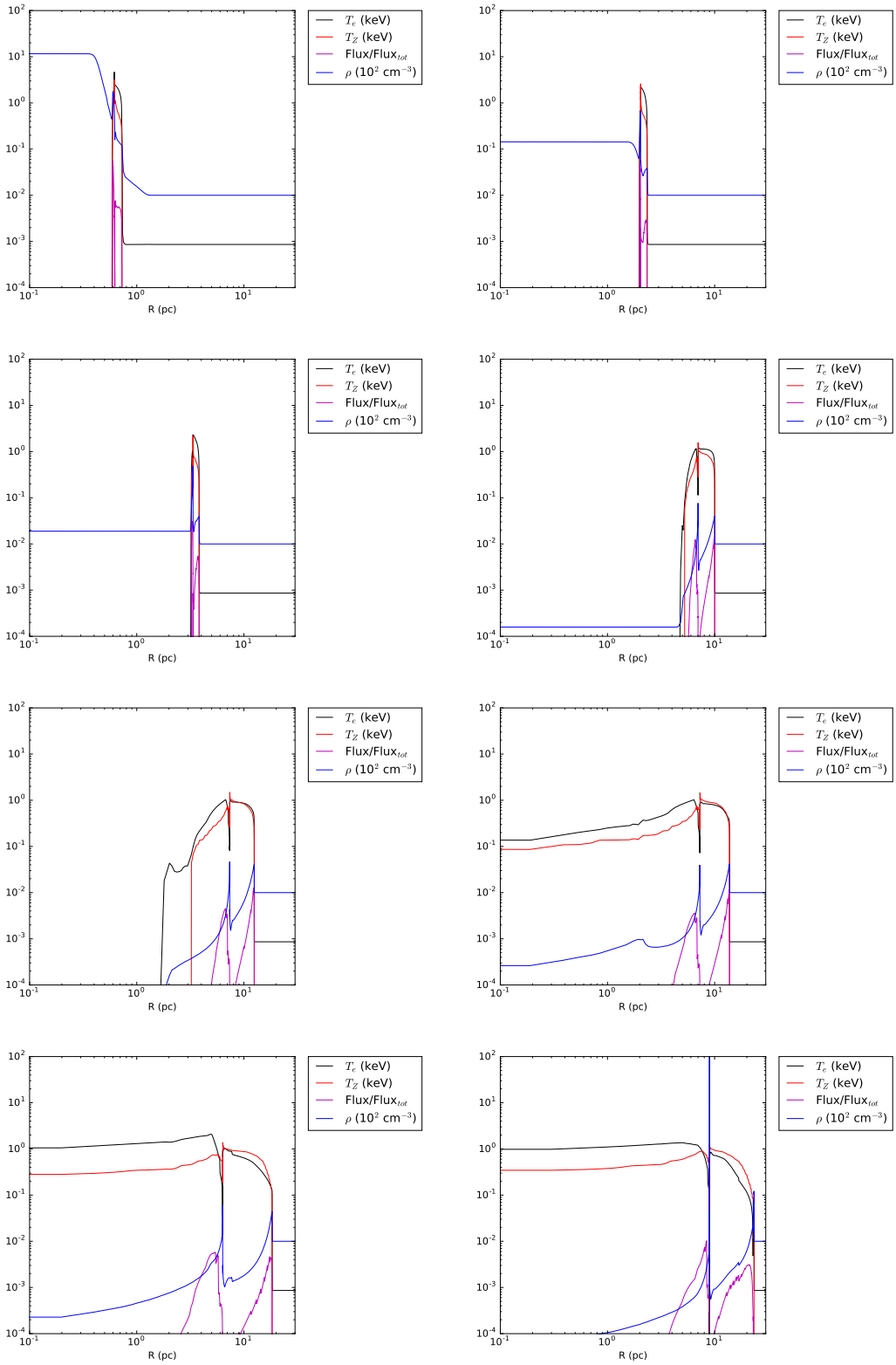

Figure 6.11: The profile of densities, temperatures and photon flux as a function of radius at 0.1, 0.5, 1, 5, 8, 10, 20, and 40 kyr extracted from the simulation with $n_{ISM} = 1$ cm^{-3}

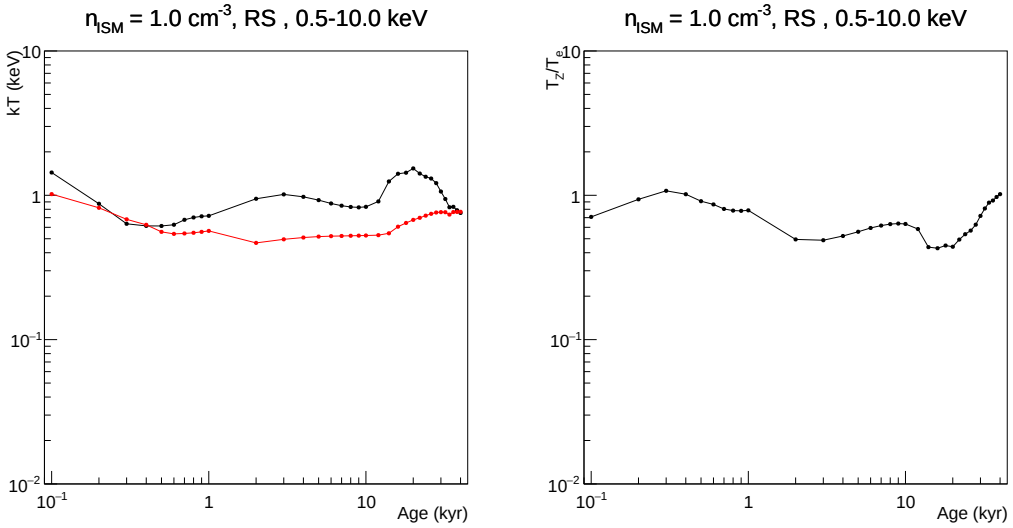

Figure 6.12: Temperatures (left) and the ratio of the ionisation temperature to the electron temperature (right) as a function of age. In the left panel, T_e (black) and T_Z (red) are integrated from the RS to the CD with the weight of the photon flux in 0.5–10 keV.

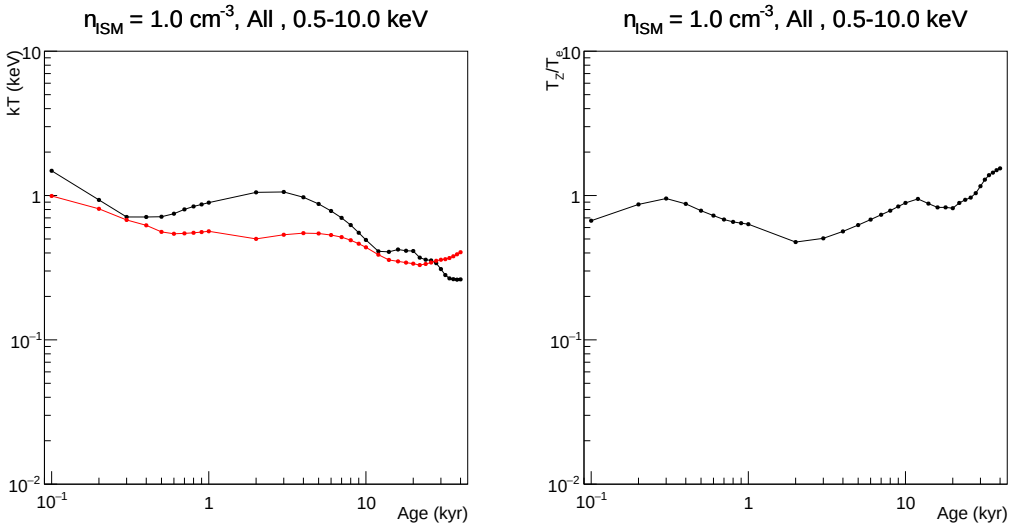

Figure 6.13: Temperatures (left) and the ratio of the ionisation temperature to the electron temperature (right) as a function of age. In left panel, T_e (black) and T_Z (red) are integrated from the RS to the FS with the weight of the photon flux in 0.5–10 keV.

profile of temperatures at each ISM density is shown in figure 6.15. The electron temperature and ionisation temperature in FS–CD decrease gradually like in the case of 1.0 cm^{-3}. The age when the ionisation temperature reaches T_e becomes shorter as the ISM density is larger. This is caused by the difference of the ionisation timescale which is short in the dense gas and the slowdown in the speed of the FS in the dense gas. Moreover, the recombination timescale is also short in the dense gas. Therefore, the ionisation temperature in a recombining plasma decreases in a short time and the plasma approaches quicker back to a CIE state. In the simulation with the ISM density of 30 cm^{-3}, the electron temperature declines most rapidly because of fast deceleration of the FS and radiative cooling. The recombining plasma formed at a younger age as the ISM density becomes high, while T_Z/T_e is not in proportion to the ISM density doe to the recombination timescale is inversely proportional to that. The simulation with $n_{ISM} = 3$ cm^{-3} show the maximising T_Z/T_e at an age of a few 10^4 yr.

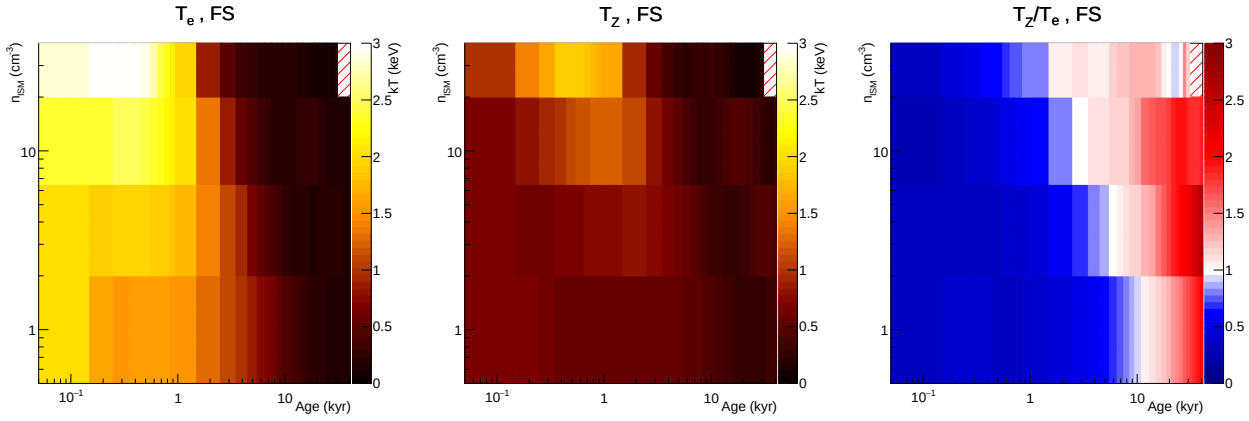

Figure 6.14: T_e (left), T_e (centre) and T_Z/T_e (right) in FS–CD weighted by the photon flux in 0.5–10.0 keV. The Red area in the right panel shows RPs. The age when the ionisation temperature reaches T_e becomes shorter as the ISM density is larger by the short ionisation timescale and large slowdown in the speed of the FS in the dense gas.

Figure 6.16 shows the dependence of the time evolution of the temperatures in RS–CD on the ISM density, and T_z/T_e. The profile of temperatures at each ISM density is shown in figure 6.17. The electron temperatures in RS–CD show several changes in the sign of the gradient with time in all simulations. As we described previous section, a first increase occurs when the reverse shock becomes strong. In the second time, the electron temperature of the shocked ejecta rises due to the deceleration of the shocked ISM. The ionisation temperature is finally higher than the electron temperature and the state of ejecta becomes the RP. The recombining process in the ejecta is similarly dominant as time passes and the surrounding gas becomes dense. Additionally, if a SN explodes in the dense ISM, the plasma state makes a transition to the RP earlier.

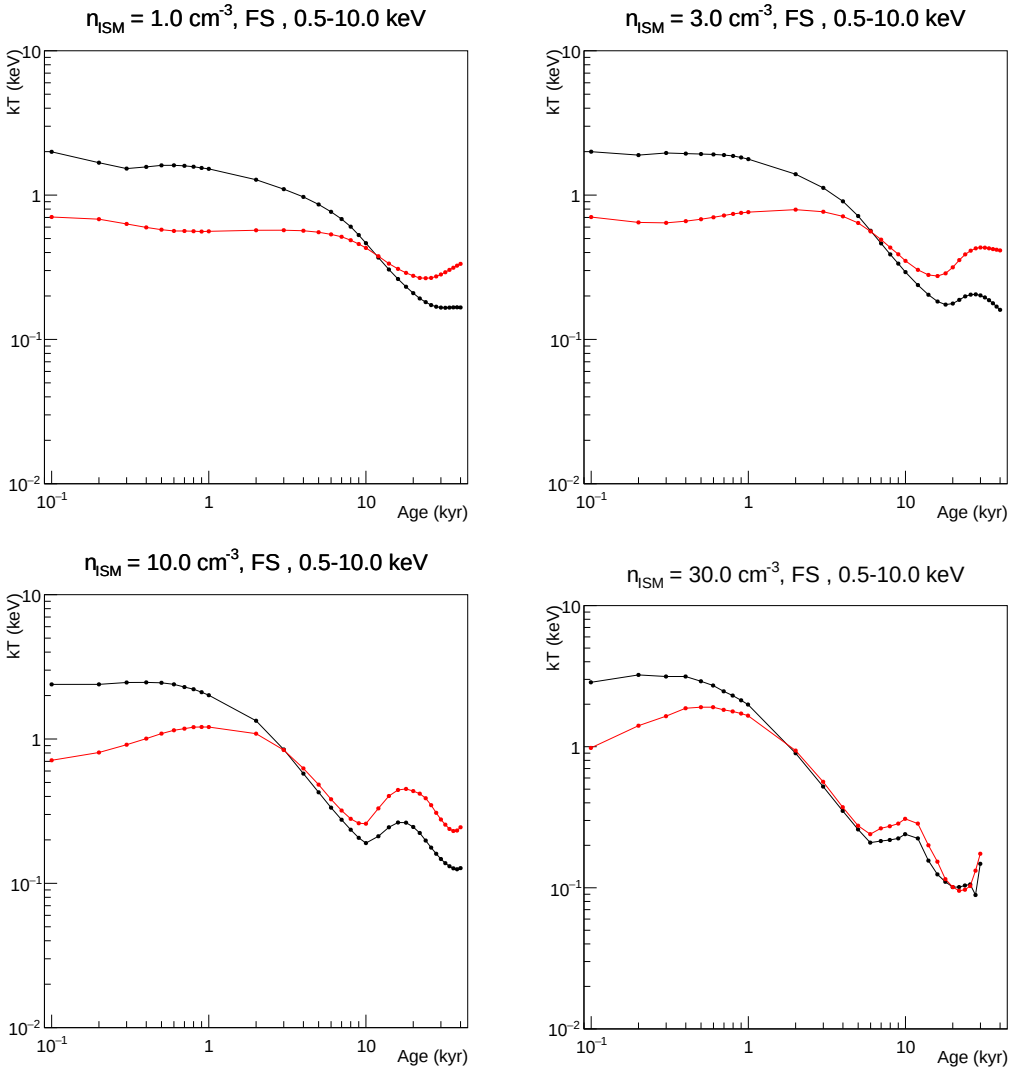

Figure 6.15: T_e (black), T_Z (red) in FS–CD weighted by the photon flux in 0.5–10.0 keV.

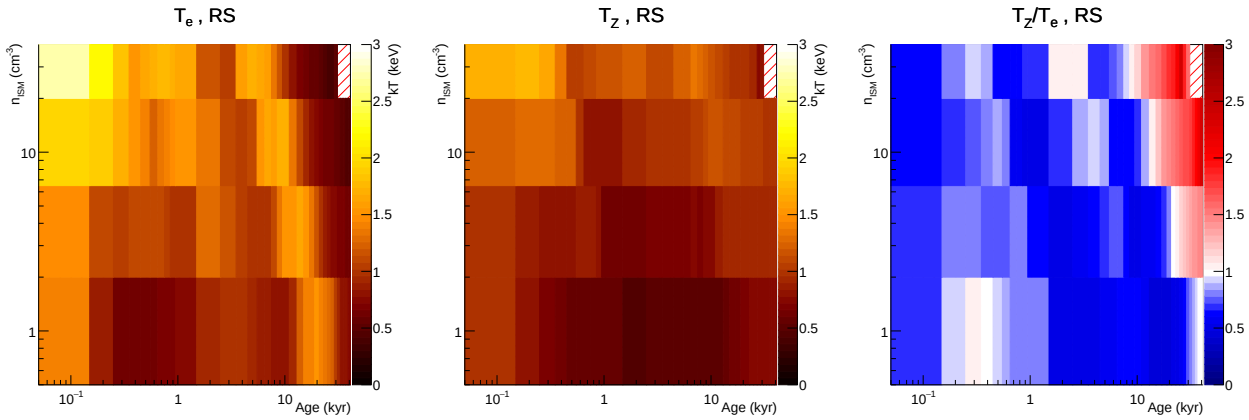

Figure 6.16: T_e (left), T_e (centre) and T_Z/T_e (right) in RS–CD weighted by the photon flux in 0.5–10.0 keV. The Red area in the right panel shows RPs. The ionisation temperature becomes higher than the electron temperature and the state of ejecta becomes the RP in the dense gas by adiabatic and radiative cooling.

Figure 6.18 shows the ratio of the photon flux in the RS–CD to that in the FS–CD estimated by spectra with an energy range of 0.5–10.0 keV. The X-ray luminosity from the ejecta is more dominant as the SNR is younger and the ISM is thin. Figure 6.19 shows the time evolution of temperatures and the ratio of the ionisation temperature to the electron temperature averaged over the entire SNR. The electron temperature decrease in a short time if the ISM is dense, and the maximum of T_e becomes higher than that in the thin ISM. The behaviour of the ionisation temperature is very similar to the electron temperature. The ratio of the ionisation temperature to the electron temperature is basically in proportion to the age and the ISM density. As the result of our study for the effect of the ISM density on the temperatures, the RP appears in a old SNR, especially with a dense ISM.

In order to confirm the effect of the ISM density on the X-ray spectrum, we fake Suzaku spectra from the simulation using the response file of CTB 1 XIS3. Figure 6.20 shows X-ray spectra simulated for each ISM density. We can see the behaviour of the electron temperature in the gradient of the continuum component. In addition, the H-like Si and H-like S RRC components are found in spectra at an age of a few 10^4 yr and the ISM density of 30 cm^{-3}.

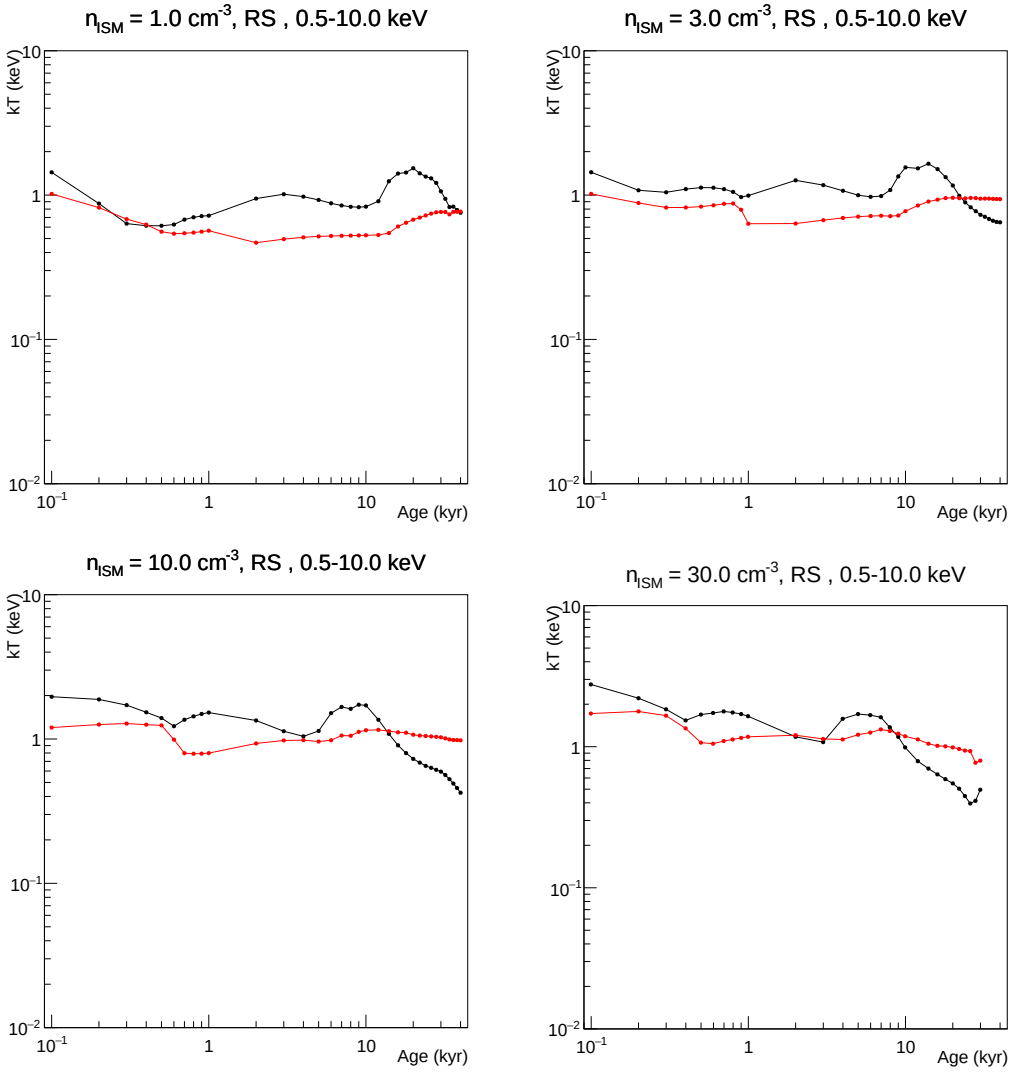

Figure 6.17: T_e (black), T_Z (red) in RS–CD weighted by the photon flux in 0.5–10.0 keV.

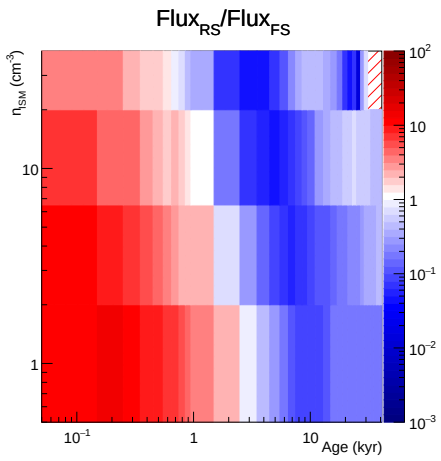

Figure 6.18: The ratio of the photon Flux in RS–CD to that in FS–CD. The photon Flux from the ejecta is more dominant as the SNR is younger.

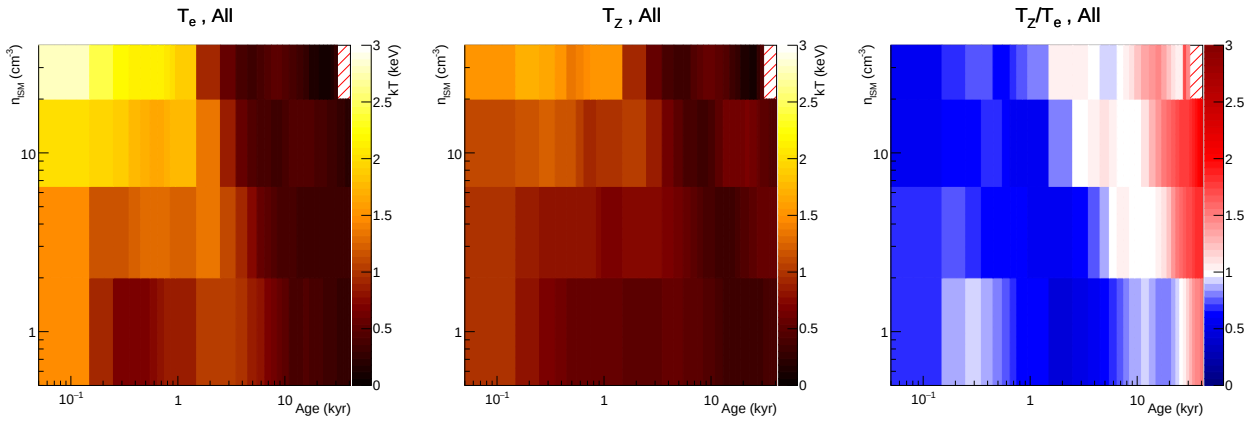

Figure 6.19: T_e (left), T_e (centre) and T_Z/T_e (right) in FS–RS weighted by the photon flux in 0.5–10.0 keV. The electron temperature decrease in a short time if the ISM is dense. The ratio of the ionisation temperature to the electron temperature is basically in proportion to the age and the ISM density.

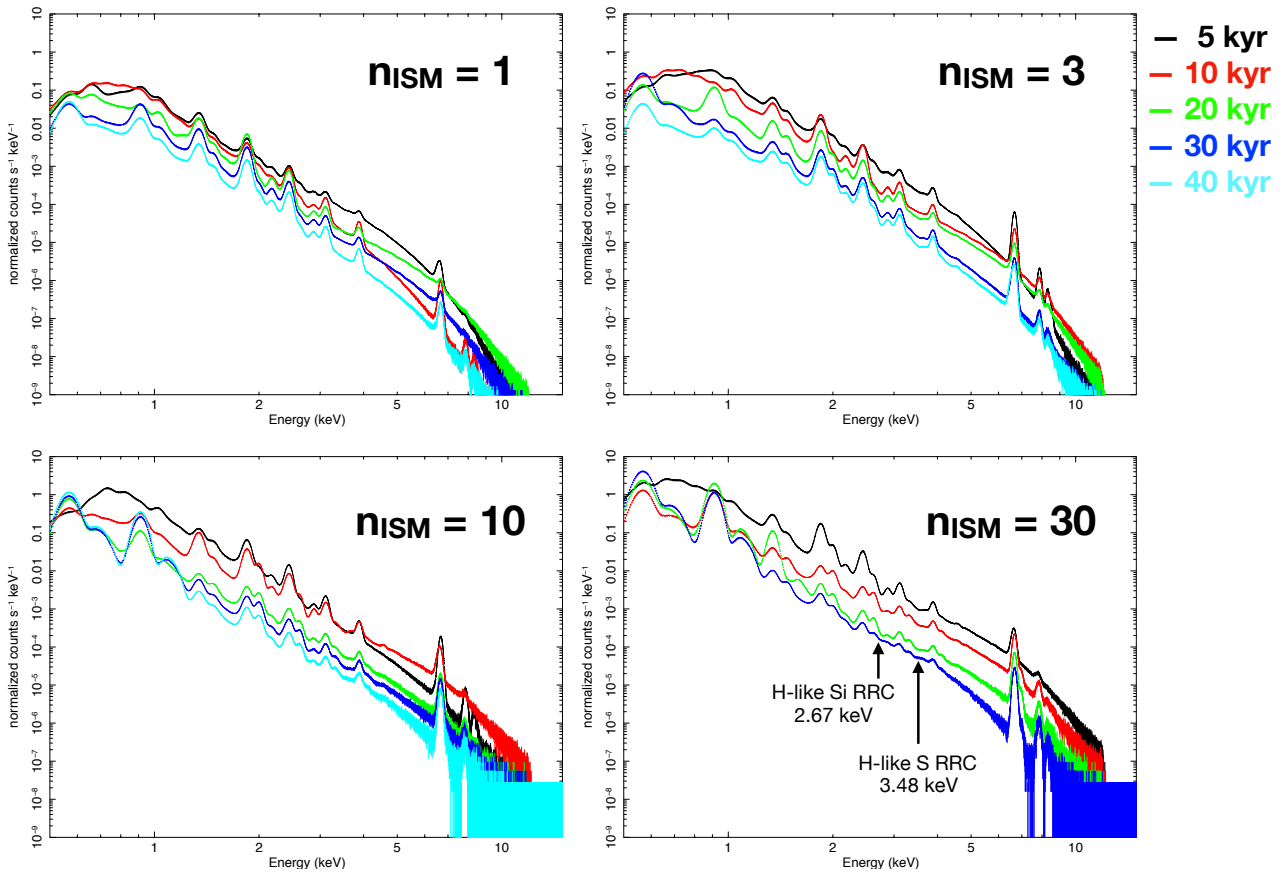

Figure 6.20: Simulated X-ray spectra for ISM densities of 1 (top left), 3 (top right), 10 (bottom left), 30 (bottom right) cm^{-3}, which faked by response file of CTB 1 XIS3. RRCs of H-like Si and H-like S are found in spectra at an age of a few 10^4 yr and $n_{ISM} = 30$ cm^{-3}.

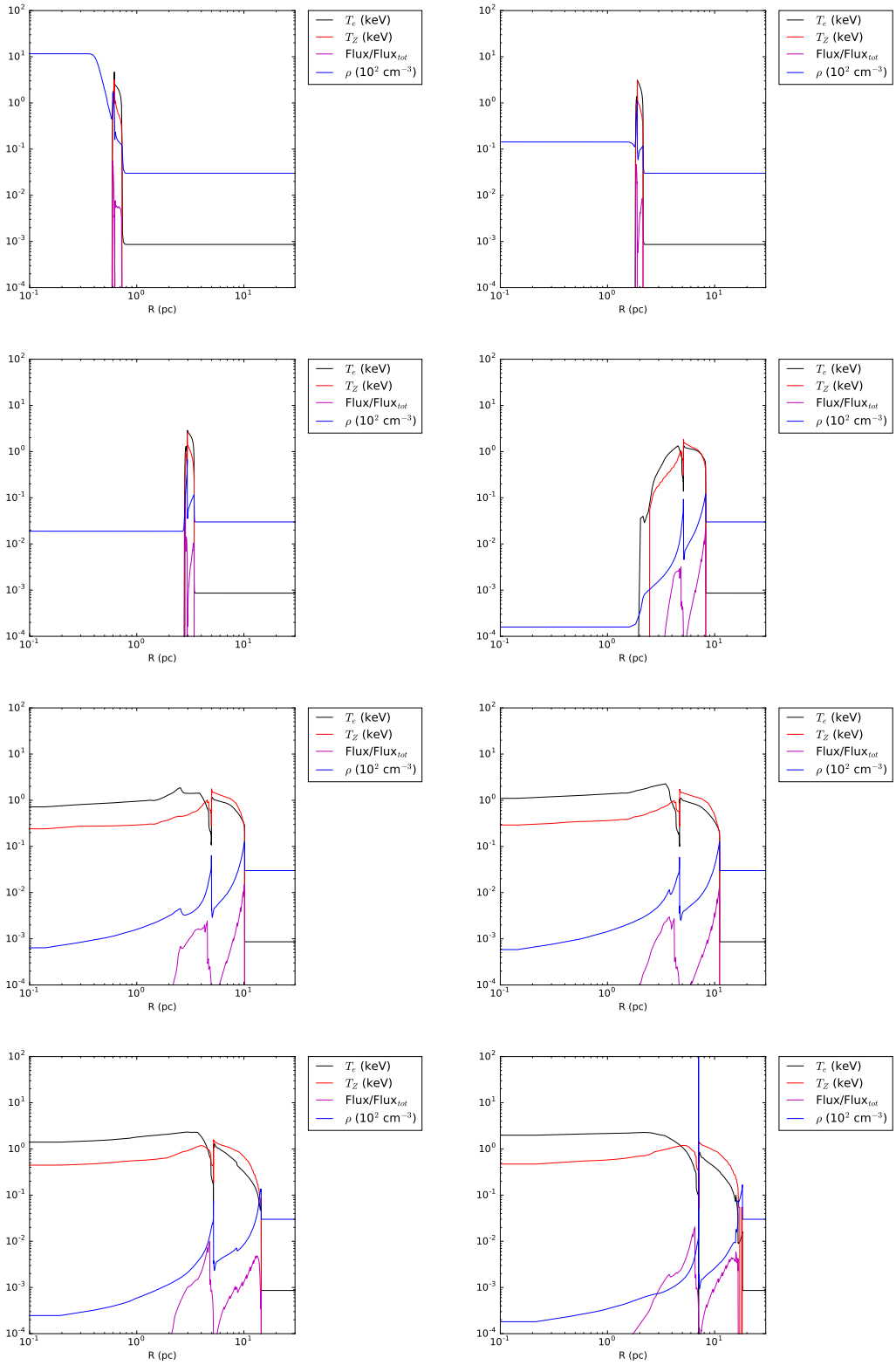

Figure 6.21: The profile of densities, temperatures and photon flux as a function of radius at 0.1, 0.5, 1, 5, 8, 10, 20, and 40 kyr extracted from the simulation with $n_{ISM} = 3$ cm^{-3}

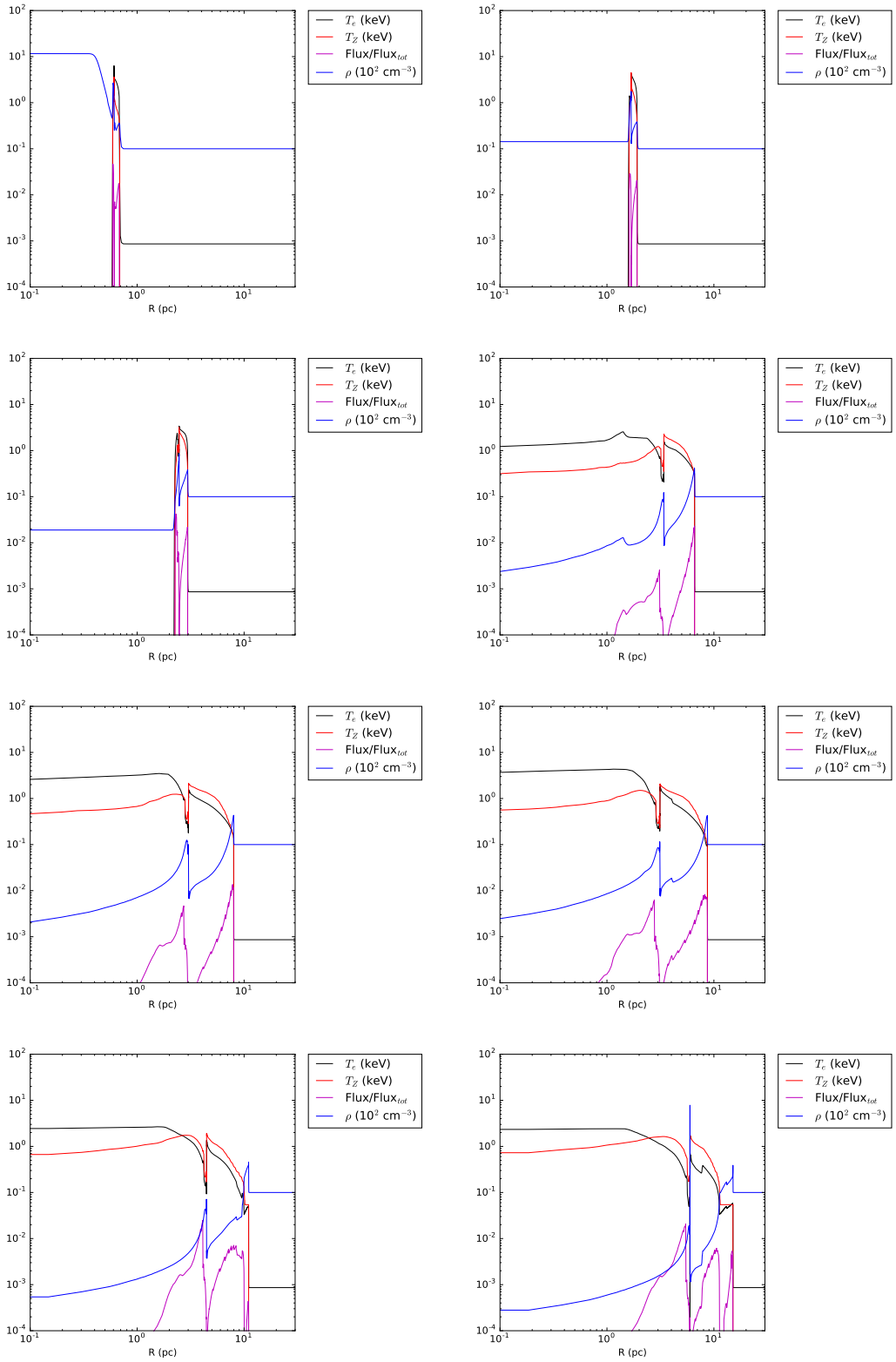

Figure 6.22: The profile of densities, temperatures and photon flux as a function of radius at 0.1, 0.5, 1, 5, 8, 10, 20, and 40 kyr extracted from the simulation with $n_{ISM} = 10$ cm^{-3}

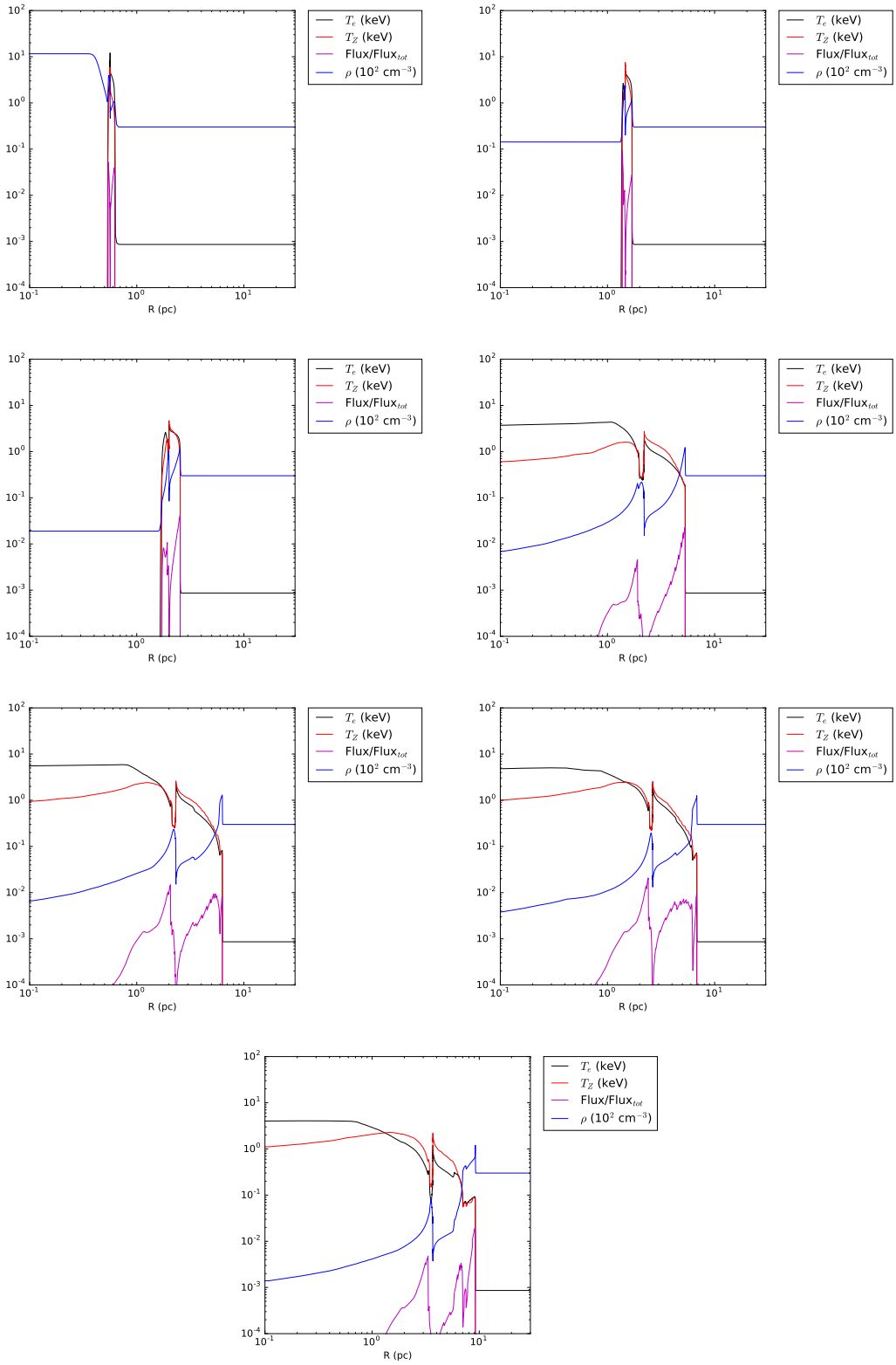

Figure 6.23: The profile of densities, temperatures and photon flux as a function of radius at 0.1, 0.5, 1, 5, 8, 10, and 20 kyr extracted from the simulation with $n_{ISM} = 30$ cm^{-3}

Chapter 7

Discussion on the formation of the recombining plasmas

In this chapter, we draw comparisons of the simulation results with observations to discuss physical and astrophysical causes of the formation of the recombining plasmas in evolved SNRs. At first, we consider the Cygnus Loop, a bright shell-like SNR with an old age, to check capability of our simulation code to follow long evolutions of SNRs. Then, we discuss evolved MM-SNRs that show the presence of the recombining plasmas.

7.1 The Cygnus Loop

Before considering MM-SNRs, it is helpful to compare our simulation with observations of a shell-like SNR, whose evolution is better understood, to check capability of our code. This gives a plain demonstration of our simulation study to follow the long stage evolution of an SNR, since previous simulation studies have not considered such evolved SNRs. In this section, we extract X-ray images and spectra that could be observed from our simulation, and make direct comparisons of characteristic observables introduced in Chapter 6.

We choose the Cygnus Loop, which is one of the brightest SNR in X-rays. Its age is estimated at 10–20 kyr (Welsh et al. 2002, Katsuda & Tsunemi 2008). The remnant is located at a distance of 0.54 kpc with a diameter of 26 pc (Uyaniker et al. 200, Blair et al. 2005). The mass of the progenitor is estimated to be 12 $M_{\odot}$ (Uchida 2010). Figure 7.1 shows an X-ray image of the Cygnus Loop by ROSAT (Uchida 2010) and the observed regions by X-ray satellites, XMM-Newton and Suzaku.

The density of the ISM surrounding the Cygnus Loop was derived by comparing the observations with the profile of the emission measure (EM) in the shell component estimated from the Sedov solutions with different densities (Uchida 2010). They reported that the EM profiles

are comparable to the models with ambient densities of 0.3–0.4 cm^{-3} at the northeast regions, while the ambient density increases to 0.7–0.9 cm^{-3} at the bright limb regions.

In the X-ray observations, the electron temperature of the ISM at the limb of the Cygnus Loop have been estimated at 0.2–0.3 keV (Uchida 2010). They analysed X-ray spectra at the limb with a model which has an ionisation-dominant plasma. The chemical composition of the model was fixed at the abundances relative to the solar values of the ISM component obtained by Tsunemi et al. (2007).

Concerning the central region of the remnant, they obtained the electron temperatures of the ejecta and the ISM by fitting the spectrum with a model having two temperature components. These electron temperatures are estimated at 0.2–0.3 keV and 0.4–0.6 keV. They fixed the abundances of the low-temperature component to those of the ISM, while the high-temperature component was assumed to be the X-ray emission from the ejecta.

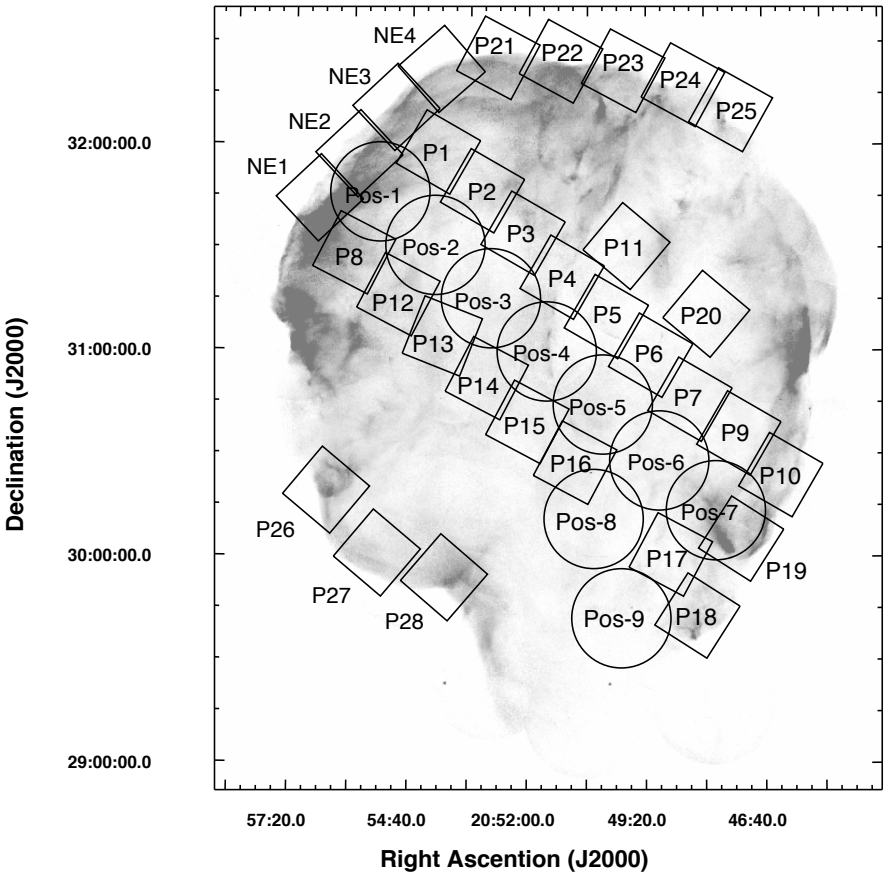

Figure 7.1: ROSAT image of the Cygnus Loop (Uchida 2010). The circles and squares denote the FOVs of the XMM-Newton MOS and the XMM-Newton XIS, respectively.

We conduct a simulation with parameters pf $n_{ISM} = 0.5$ cm^{-3} and a progenitor mass of 15 $M_\odot$, and took a snapshot at 10^4 yr. The ejecta mass and explosion energy are 10.9 $M_\odot$ and

1.21×10^{51} erg, respectively. These conditions match observational estimates of the Cygnus Loop.

Figure 7.2 shows X-ray images extracted from the simulation at an age of 10 kyr in energy bands of 0.5–10.0 keV, 0.5–1.0 keV, and 1–10.0 keV. These images display clear shell structures at the edge of the remnant in all energy ranges. The radius of the shell obtained from the simulation is ∼15 pc and well agrees with the observed value of 13 pc. The inner shell at r = 8 pc is created by the dense gas around the contact discontinuity between the ejecta and CSM, though this structure is not detected in the observations. Note that some small circular patterns are artefacts due to treatment of projection on a cartesian grid when making the sky images..

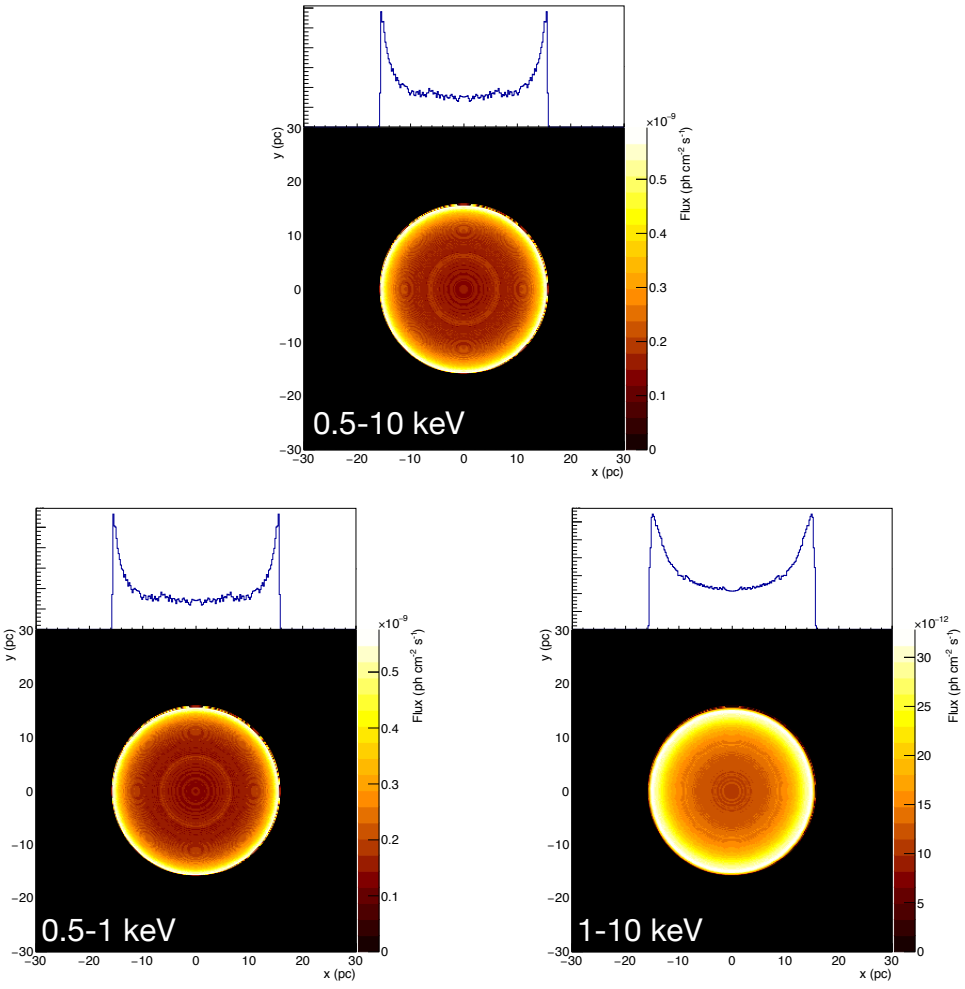

Figure 7.2: X-ray morphology obtained with the simulation. The image are snapshot at an age of 10^4 yr in 0.5–10.0 keV (top), 0.5–1.0 keV (bottom left), and 1.0–10.0 keV (bottom right). Each upper panel shows a cross section of the image at y = 0 cm in a linear scale. The shell structure appears at the edge of the remnant in all energy range. The radius is ∼ 15 pc, which is consistent with the observation (13 pc).

In order to compare the simulations with the observations in the ejecta and the ISM, we choose the two observed regions P11 and P23, as shown in Figure 7.1. The observations at P11 and P23 focused on the central region and the limb of the Cygnus Loop. Figure 7.3 compares simulated X-ray spectra with the observations in the ISM (P23) and the ejecta (P11). The Suzaku spectra are generated by using responses of the telescope and the detector on board Suzaku from the determined model parameters by Uchida (2010). The simulation model is attenuated by an interstellar absorption with observation value. The normalisation is scaled to fit. The simulated spectra used for the comparisons with P11 and P23 are integrated along the lines of sight at radii of 8 pc and 15 pc, respectively.

As shown in the left panel in Figure 7.3, the shape of the continuum component of our model well agree with the Suzaku spectrum in P23. The line emissions of H-like O VIII Lyα at 0.65 keV and Mg XI Heα at 1.3 keV are well reproduced. These mean that the abundances and ionisation states of Mg and O in our code are consistent with the observation. The intensities of line emissions around $\sim$ 0.8 keV and $\sim$ 1.1 keV are lower in our model than the Suzaku results. These energy correspond to the L-shell emission lines of iron. Therefore, these low intensities of the simulation indicate the different abundance ratio of Fe to the other element from the observation ($\mathrm{Fe_{sim}/O_{sim}} = 0.05$, $\mathrm{Fe_{obs}/O_{obs}} = 0.12$).

The continuum component of the Suzaku spectra in P11 is also reproduced by the simulation of the ejecta as shown in the right panel in Figure 7.3. We can see the lower intensities of the simulation than those of the observation around $\sim$ 0.8 keV. This is also explained by the lower Fe abundance of the simulation model than that of the observation.

We then compare the electron and ionisation temperatures between the simulations and observations. The electron temperatures were derived by Uchida (2010) and their results are summarised in Table 7.1. We calculate the ionisation temperatures from the spectral fitting results by Uchida (2010) is also shown in Table 7.1.

Table 7.1: Observation results.

Object	Region	$n_e t(10^{11})$	kT_e (keV)	kT_Z (keV)
Cygnus Loop	P23	$0.6^{+0.8}_{-0.2}$	$0.43^{+0.04}_{-0.05}$	$0.30^{+0.07}_{-0.03}$
	P11	0.7±0.3	0.63±0.01	$0.43^{+0.02}_{-0.07}$

Our simulation successfully produces the observed trend of the ionising plasma (IP), in which the electron temperature becomes higher than the ionisation temperature. In addition, we reproduced the higher electron temperature of the ejecta than that of the ISM, which is consistent with the observation. Figure 7.4 shows the time evolutions of the temperatures averaged over the ejecta and ISM calculated in the case from of $n_{ISM} = 0.5$ cm^{-3}, and the observation data points. For the simulation temperatures, we make use of temperatures averaged with the weight of the photon flux within the energy range of 0.5–10 keV at each Lagrangian grid.

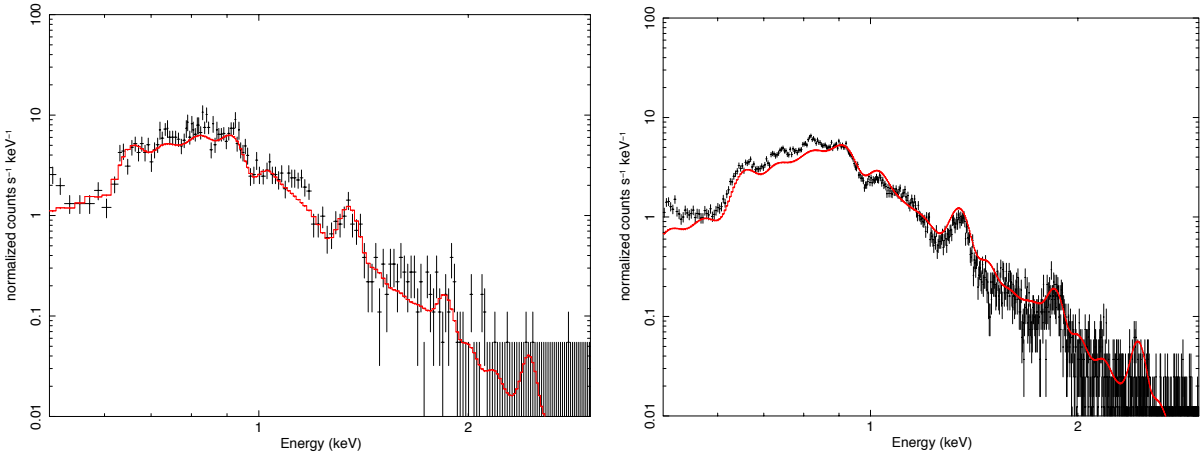

Figure 7.3: The left panel shows a Suzaku XIS spectrum at a limb of Cygnus Loop (P23 in figure 7.2) and our model (red line) of $n_{ISM} = 0.5$ cm^{-3} and an age of 10^4 yr extracted at a projected radius of 15 pc. The right panel shows an XIS spectrum at the centre of Cygnus Loop (P11 in figure 7.2) and our model of the same model with a projected radius of 8 pc. Note that these XIS spectra are "generated" spectra with the parameters by Uchida (2010) by the response file of the XIS3 analysis of CTB1. So, they are "faked" spectra using the XSPEC tool.

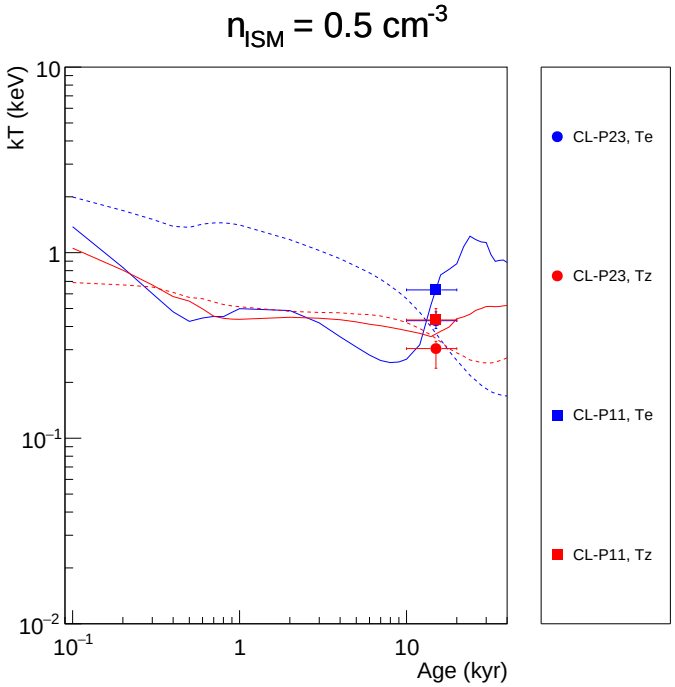

Figure 7.4: Comparisons of the electron (blue) and ionisation (red) temperatures in the two regions in the Cygnus Loop between our simulation model and the Suzaku observations. The solid and dashed lines are the flux-averaged temperatures calculated from the simulation as functions of the age in the regions of the ejecta and the ISM, respectively. This simulation assumes parameters of a progenitor mass of 15 $M_\odot$ and an ISM density of 0.5 cm^{-3}. The observational data points are shown in the same colour assignment and their extracted regions are found in the legend.

The electron and ionisation temperatures of the simulations are in good agreement with those obtained from the observations.

The simulations naturally produce basic observational figures and characteristics including the size, spectrum, electron and ionisation temperatures of the evolved shell-like SNR Cygnus Loop. It is demonstrated that our code is able to follow time evolution of an SNR from the early phase of its SN explosion to an old age of $\sim$10 kyr without any significant error. This check is an important milestone toward the application of the simulation code to evolved MM-SNRs.

7.2 Evolved MM-SNRs

In order to study the relation between the RP associated with MM SNRs and the dense ISM surrounding them, we here compare simulation results for ISM densities $n_{\rm ISM}$ = 1, 3, 10, and 30 cm^{-3} with observations of the evolved MM-SNR that show the presence of the RP. We assume the s25D model described in §5.2.2. In this section, we discuss the effects of the ISM on the formation of the RP based on the comparisons.

We select objects whose X-ray spectra have been analysed by using the recombining plasma model. The selected SNRs are CTB 1, IC 443, W49B, W28, W44, G346.6-0.2, 3C 391, G290.1-0.8, N49, Kes 17, G166.0+4.3, 3C 400.2, and HB 21. Key properties of these SNRs are summarised in Table 7.2. These objects are categorised into the MM-SNRs which have radio shells and centre-filled X-ray emissions. In order to compare the simulations with their observations in the same region, we use observation results extracted from the entire SNR region basically. If analysis results of the entire region is not available, we use an observation in a region where the strongest trend of the over-ionised state is detected.

Table 7.2: Observation results.

Object	Age (kyr)	Distance (kpc)	Size (pc)	Region	$n_e t$ (10^{11} cm^{-3} s)	kT_{init} (keV)	kT_e (keV)	kT_z (keV)	Ref.
CTB 1	9–44	1.6–3.1	16–30	SW	9.3	3.0	$0.186^{+0.008}_{-0.007}$	$0.78^{+0.03}_{-0.02}$	1
IC 443	4–30	0.7–2.0	10–26	SE	4.2	3.0	0.19±0.01	$1.17^{+0.02}_{-0.03}$	2
					4.2	5.0	$0.54^{+0.03}_{-0.01}$	1.50±0.04	
W49B	3.1–5.9	10.9–11.7	(12–14)×10	Whole	4.4	5.9	0.94±0.02	$1.72^{+0.04}_{-0.06}$	3
					0.9	3.26	$1.46^{+0.01}_{-0.08}$	$2.59^{+0.01}_{-0.08}$	
W28	33–36	1.6–2.2	22–30	Centre	10.1	3.8	$0.216^{+0.001}_{-0.005}$	0.74±0.02	4
					3.7	3.8	$0.52^{+0.01}_{-0.02}$	$1.53^{+0.04}_{-0.08}$	
W44	10–20	3	30×24	Whole	3.5	0.93	0.37±0.01	$0.73^{+0.03}_{-0.02}$	5
G346.6-0.2	14–16	7–8	16–18	A	4.8	5.0	$0.30^{+0.03}_{-0.01}$	$1.20^{+0.06}_{-0.14}$	6
3C391	7.4–8.4	6.7–7.5	(14–16)×10	Whole	14.0	1.8	0.495±0.015	$0.65^{+0.18}_{-0.10}$	7
G290.1-0.8	10–20	6–8	(26–34)×(10–24)	Centre	12.2	1.7	$0.42^{+0.02}_{-0.01}$	$0.66^{+0.14}_{-0.09}$	8
N49	4.8	50	22	Whole	7.0	11.0	0.62±0.01	$1.21^{+0.01}_{-0.04}$	9
Kes 17	2–40	≥9.7	≥22	Whole	16	5.0	0.73±0.03	$0.87^{+0.02}_{-0.05}$	10
G166.0+4.3	24	4.5–5.5	(72–88)×(46–56)	NE	6.1	3.0	0.46±0.03	1.13±0.05	11
3C400.2	14–32	2.0–3.6	(19–34)×(16–30)	NE	1.8	3.15	$0.71^{+0.03}_{-0.02}$	$1.99^{+0.29}_{-0.22}$	12
HB 21	4.8–15	1.2–2.2	(38–66)×(26–46)		3.2	5.9	0.17±0.01	0.52±0.08	13

[1] Craig & Hailey (1997), Koo & Heiles (1991), Fesen (1997), Lazendic & Slane (2006), Katsuragawa et al. (2018), [2] Troja et al. (2008), Olbert et al. (2001), Lozinskaya (1981), Green (1984), Matsumura et al. (2017b), [3] Smith et al. (1985), Moffett & Reynolds (1994), Zhu et al. (2014), Matsumura (2018), [4] Velazquez et al. (2002), Rho & Borkowski (2002), [5] Smith et al. (1985), Wolszczan et al. (1991), Goss (1968), Matsumura (2018), [6] Yamaguchi et al. (2013), [7] Leahy & Ranasinghe (2018), Ranasinghe & Leahy (2017), Sato et al. (2014), [8] Slane et al. (2002), Reynoso et al. (2006), Kamitsukasa et al. (2015), [9] Park et al. (2012), Pietrzynskiski et al. (2013), Uchida et al. (2015), [10] Gelfand et al. (2013), Caswell et al. (1975), Washino et al. (2016), [11] Burrows & Guo (1994), Pineailt et al. (1987), Matsumura et al. (2017a), [12] Long et al. (1991), Giacani et al. (1998), Ergin et al. (2017), [13] Lazendic & Slane (2006), Leahy (1987), Byun et al. (2006), Suzuki et al. (2018)

7.2.1 Morphology and sizes of the SNRs

Firstly, we compare X-ray images of SNRs extracted from the simulations with the observations. Figure 7.5 shows the simulated images of the X-ray emissions in an energy band of 0.5–10 keV at 10, 20, 30, and 40 kyr. The centre-filled X-ray emissions are formed in some parameters:n_{ISM} = 1 cm^{-3} at 10, 20, 30 kyr, n_{ISM} = 3 cm^{-3} at ages of 10, 20, 40 kyr, and n_{ISM} = 10 cm^{-3} at 10 kyr. Figures 7.6 and 7.7 show the simulated images of the X-ray emissions in an energy band of 0.5–1 keV and 1–10 keV. We can see the the centre-filled X-ray emissions in all of the 1–10 keV band images, while some images show the centre-filled X-ray emissions in an energy band of 0.5–1 keV. The X-rays with the high energy is emitted from the ejecta. Thus, the simulation can produce the important morphological feature of the MM-SNR that its X-ray emission is concentrated in the central region of the remnant. In other cases, the X-ray images look shell-like, but the X-ray intensities from the central region have a larger fraction when compared with the case of the Cygnus Loop. This increase of the central X-ray emission may suggest a link to MM-SNRs. Those results imply that a one-dimensional hydrodynamic process already contains a part of important effects that generate the morphological feature of the MM-SNR.

We then discuss the sizes of the MM-SNRs. Figure 7.8 shows the cross section of the 2-D images in 0.5–10 keV as a function of the age and for the different values of the the ISM density. The radii and the estimated ages of the observed SNRs are also shown in the same plots. The size of the remnant expands with time. The SNR size decreases as the ISM density sets higher because the FS is decelerated by the dense ISM in a short time. Most of the SNRs have sizes consistent with the simulation. G116.0+4.3 and N49 are larger than all of the simulations. The sizes of HB 21 and W44 agree with the simulation of n_{ISM} = 1 and 3 cm^{-3}, respectively. The other SNRs are well reproduced by the simulation of n_{ISM} = 10 or 30 cm^{-3}.

It should be noted that the distances to the objects and their ages have large uncertainties by a factor of $\sim$ 2. The morphology largely depends on time, and the above discussion on it can change due to the observational ages. Observation which gives us a correct distance and age is important to study the structure of X-ray emission in SNRs.

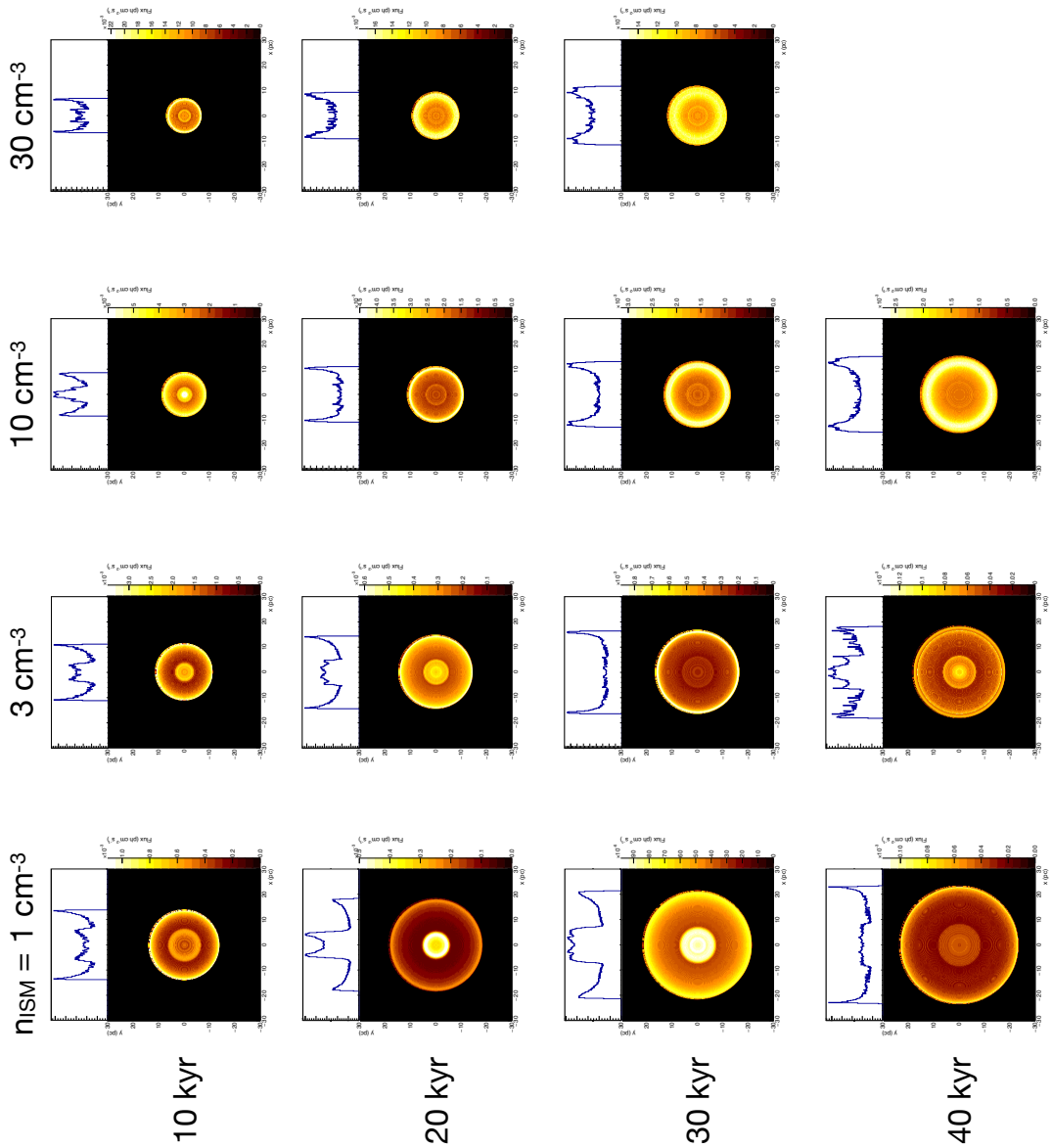

Figure 7.5: Simulated X-ray images in an energy band of 0.5–10 keV projected to the sky for different values of the ISM densities at difference ages. Each upper panel shows a cross section of the image at y = 0 cm. The centre-filled X-ray emissions are found in images of $n_{ISM} = 1$ cm^{-3} at 10, 20, 30 kyr, $n_{ISM} = 3$ cm^{-3} at ages of 10, 20, 40 kyr, and $n_{ISM} = 10$ cm^{-3} at 10 kyr. This result suggests the simulation can produce the important morphological feature of the MM-SNR.

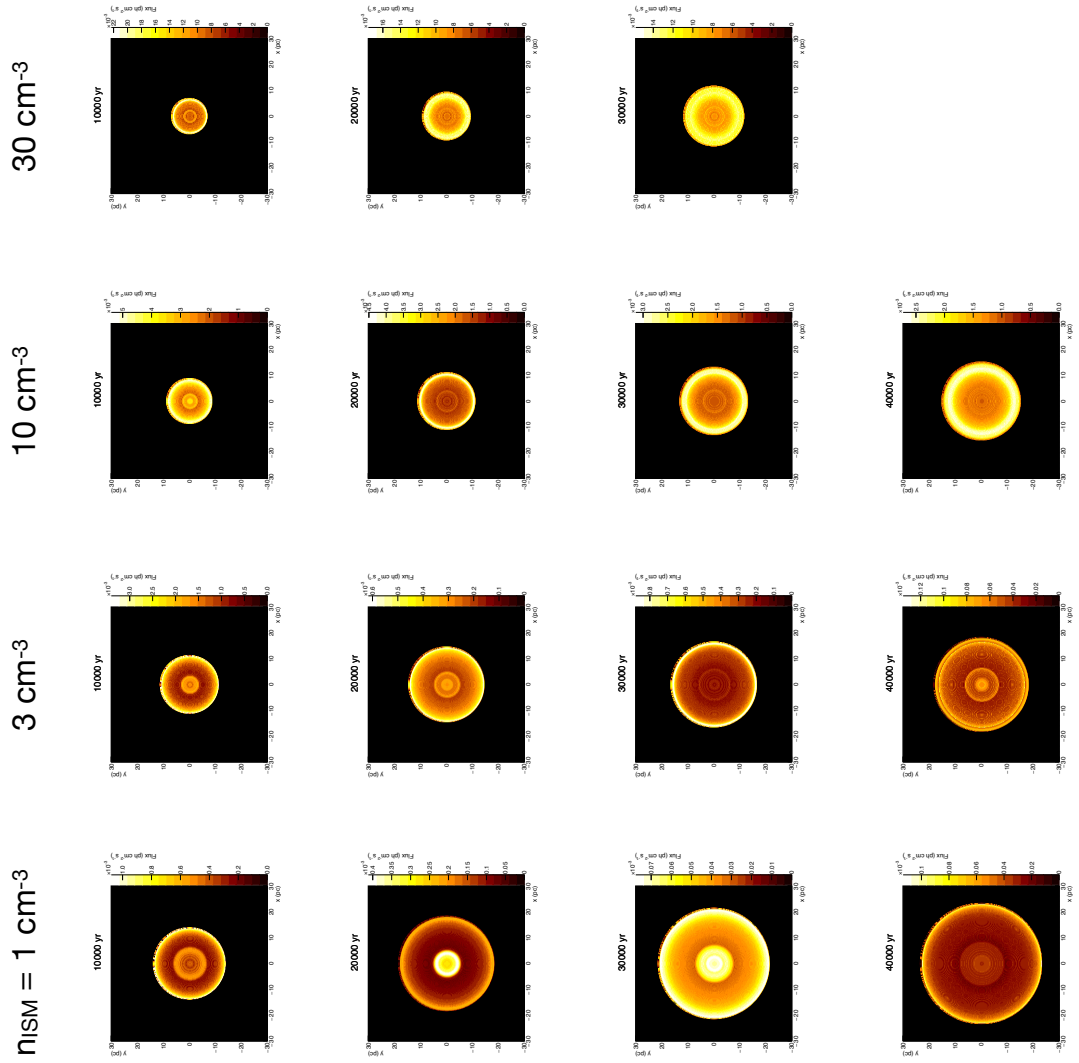

Figure 7.6: The same as Figure 7.5 but for an energy band of 0.5–1 keV. Most images show the shell structure which indicates that X-ray from the ISM is dominant in 0.5–1 keV.

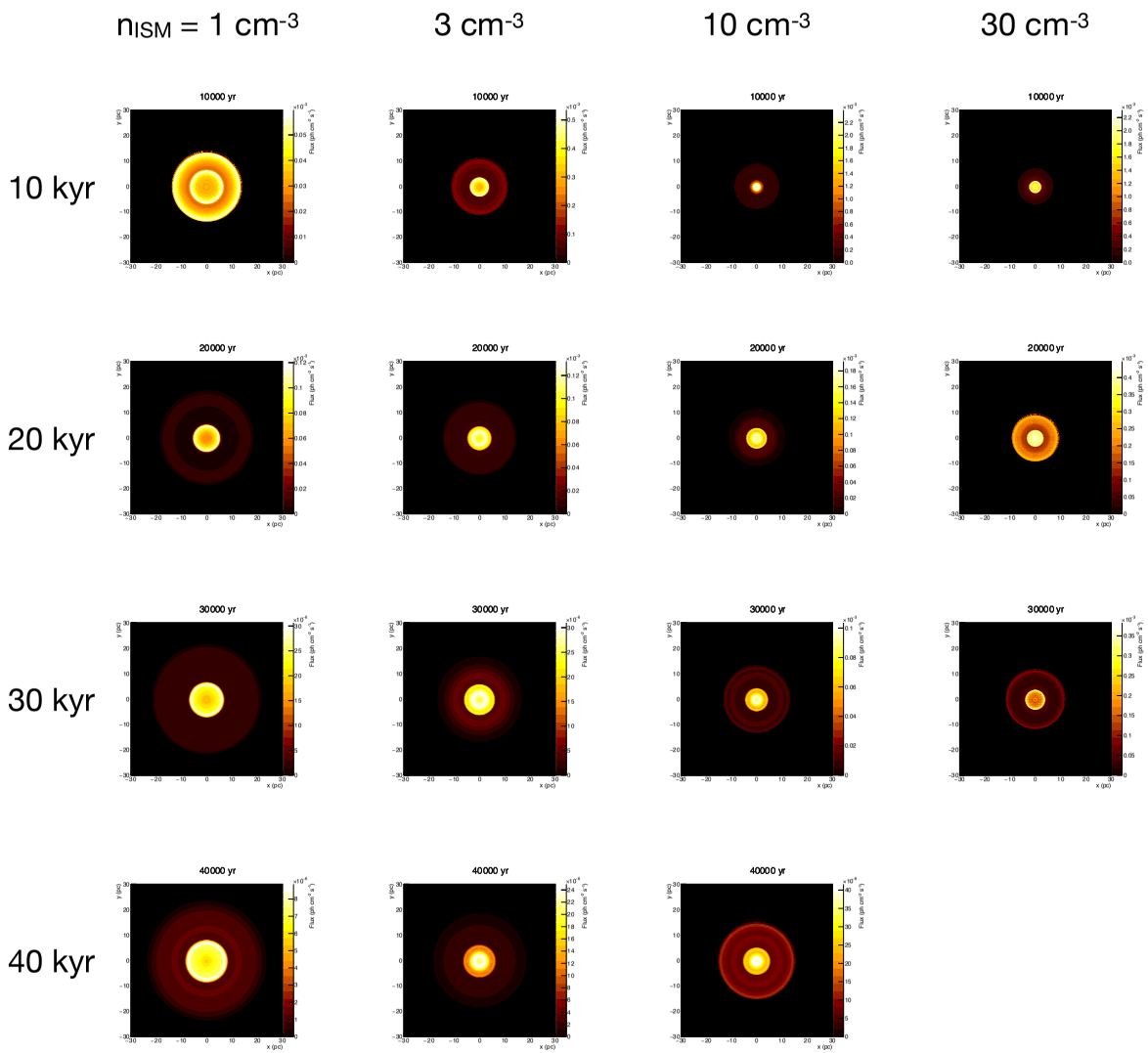

Figure 7.7: The same as Figure 7.5 but for an energy band of 1–10 keV. The centre-filled X-ray emissions are found in all images except the case of $n_{ISM} = 1$ cm^{-3} at 10 kyr.

7.2.2 X-ray spectra of IC 443

To make comparisons of X-ray spectra between the simulations and observations, we use an X-ray spectrum of IC 443 obtained with Suzaku. IC 443 is a bright MM-SNR, and thus its data quality is excellent for the comparisons. Moreover, this object has one of the most prominent features of the RRC in its X-ray spectrum at 1.96 keV (Mg XII), 2.67 keV (Si XIV), and 3.48 keV (S XVI). We focus on the southeast region of this SNR, here after IC 443 SE (Matsumura et al. 2017b). We subtract a background spectrum used by Matsumura et al. (2017b) form the observed spectrum. We make a model described by TBabs×(CC-Ejecta + power law), where CC-Ejecta is a plasma model generated from our simulation, and has three parameters of the ISM density, age, and normalisation. Parameters of the absorption (TBabs), photon index and normalisation of the power law component are fixed at the values obtained by Matsumura et al. (2017b).

Figure 7.9 shows the spectrum of IC 443 SE observed by Suzaku XIS3 and a model created by a simulation for a different ISM density in each panel. The ISM density of CC-Ejecta (blue line) is set to 1, 3, 10, or 30 cm^{-3} and the age is optimised by fitting to the data in each spectrum. The shape of the continuum for n_{ISM} = 30 cm^{-3} well agrees with the observed spectrum, whereas the intensities of a few lines are different. We find increases of the RRC of H-like Mg (1.96 keV), H-like Si (2.67 keV), and H-like S (3.48 keV) in the model of n_{ISM} = 30 cm^{-3} as shown by arrows in Figure 7.9, whose energy edge is 1.96, 2.67, and 3.48 keV, respectively. The age is estimated at 21.9±0.6 and 30 (upper limit) kyr by fitting with n_{ISM} = 10 and 30 cm^{-3}, respectively. These ages of IC 443 are consistent with a previous study Olbert et al. (2001).

A MM-SNR may be formed in a complex environment, e.g. inhomogeneous density. Our simulation assuming a uniform ISM density and one spatial dimension of the model can be too simple for such a complex structure. In order to consider the more complex ISM density, we build a model as a combination of two spectra with n_{ISM} = 1 and 30 cm^{-3} as shown in Figure 7.10. We obtain their normalisation ratio (1 cm^{-3}:30 cm^{-3}) of 5:3 by fitting the spectrum with the model. The degree of the agreement is significantly improved particularly at some lines. This suggests that the spectrum has been generated in a complex environment. However, the RRC features are only explained by the model with the dense ISM, which plays an important role in generating the RP. Therefore, we conclude that MM-SNRs which display RPs are results of interactions between a part of the SN ejecta and dense regions of the ISM with densities higher than $\sim 10\mathrm{cm}^{-3}$.

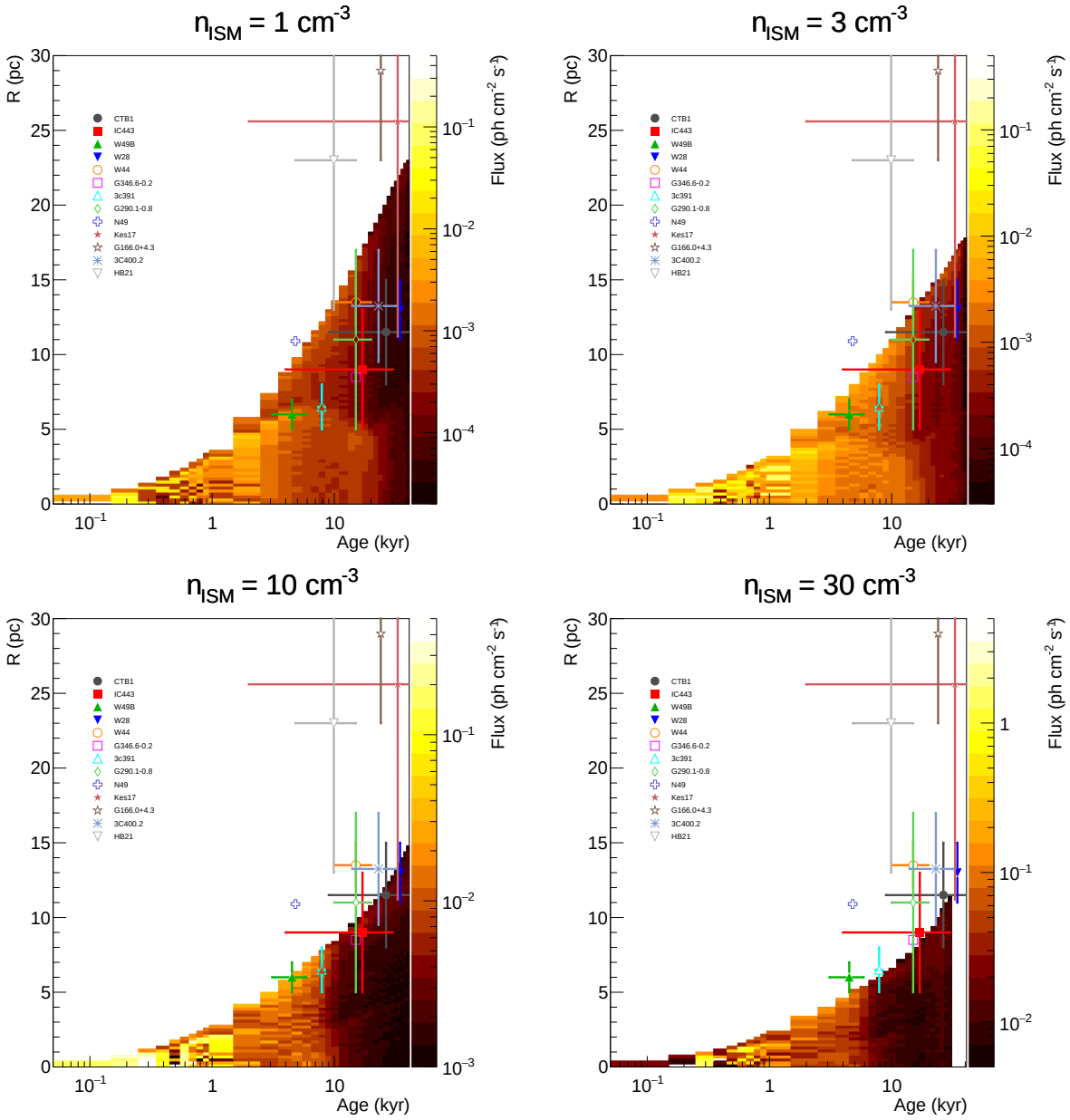

Figure 7.8: Time evolution of the radial profile of the X-ray images projected to the sky for different ISM densities. The sizes and ages of the SNRs on the observation list are plotted in each panel. Most of the SNRs have sizes consistent with the simulation of n_{ISM} = 10 and 30 cm^{-3}.

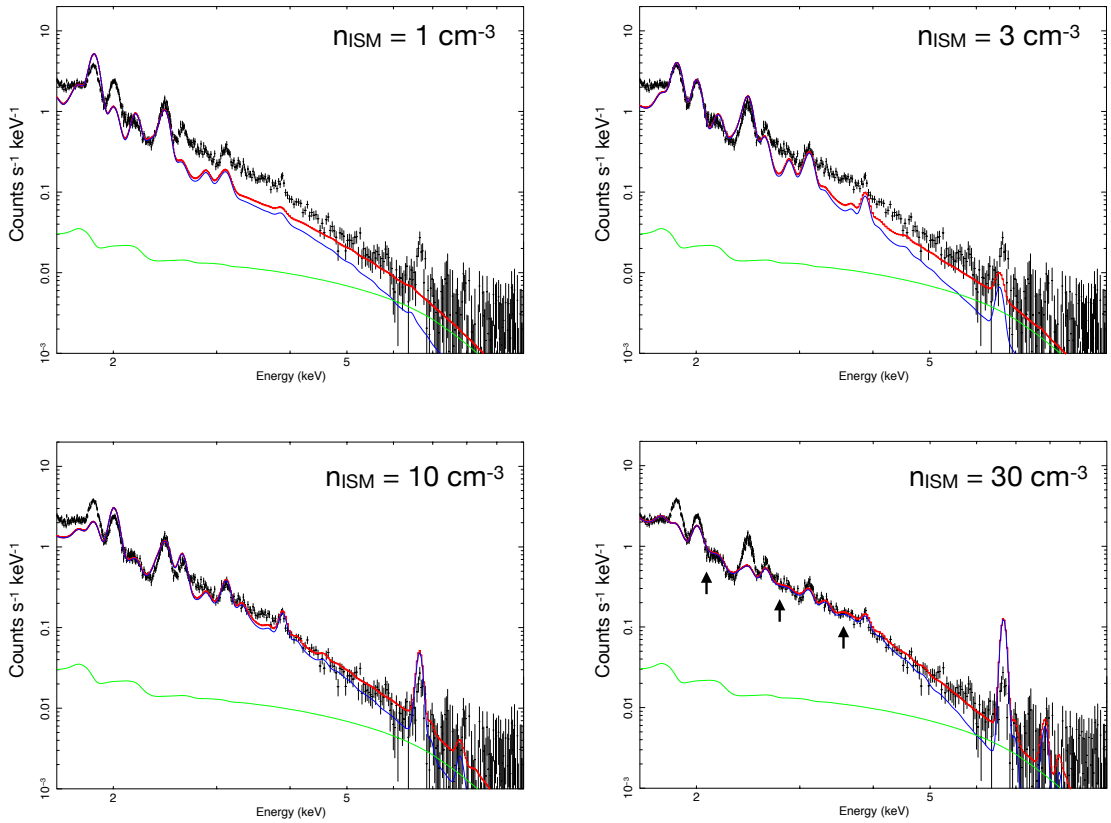

Figure 7.9: Suzaku XIS3 spectra of IC 443 SE (black) and the model created from our simulations (red). Blue and green lines are our plasma model (CC-Ejecta), and the power law component determined by Matsumura et al. (2017b). The arrows indicate the RRC from H-like Mg (1.96 keV), H-like Si (2.67 keV), and H-like S (3.48 keV). The shape of the continuum for $n_{ISM} = 30$ cm^{-3} well agrees with the observed spectrum.

7.2.3 Electron and ionisation temperatures

We compare the electron and ionisation temperatures between our simulations and the observations listed in Table 7.8. We show the observed temperatures of RP components. For SNRs which have been fitted with two temperature components, we indicate them by "-hi" and "-low". The electron and ionisation temperatures of the simulations average values with weights of the total photon flux in 0.5–10.0 keV over the grid (ref to Sec. 6.4). Although these comparisons are useful for considering the systematic samples of the MM-SNRs, we should be careful about the precision of the comparisons. The simulation values are averaged over a broad range in radius, and the observation values have been taken from different publications, which should have different observation and analysis conditions.

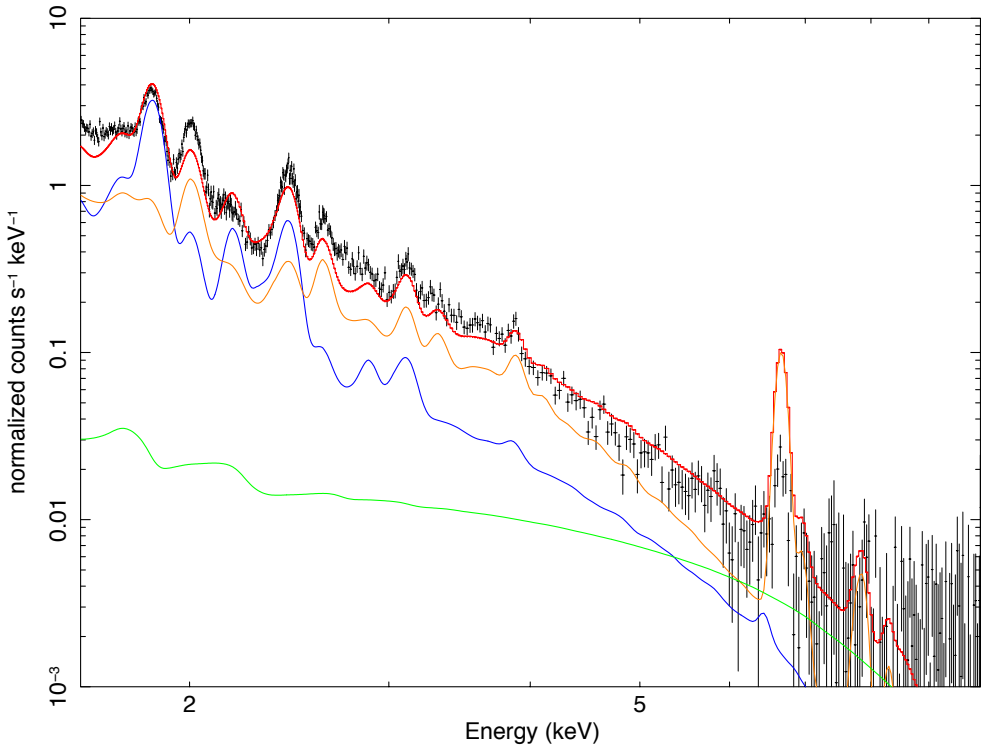

Figure 7.10: Suzaku XIS3 spectra of IC 443 SE (black) and the model (red) composed of two plasma components, which are obtained from our simulations of $n_{ISM} = 1$ cm^{-3} (blue) and 30 cm^{-3} (orange), and power-law component (green) determined by Matsumura et al. (2017b). The degree of the agreement is significantly improved particularly at some lines compared with the model created from simulation of $n_{ISM} = 30$ cm^{-3}.

Since the abundances of the RP estimated from the observations are not consistent with the chemical composition of ISM, the RP is probably dominated by the ejecta components. Figures 7.11 and 7.12 show the ionisation and electron temperatures obtained from the observations. The average temperatures of the ejecta calculated from the simulations are also plotted in these figures. The ionisation temperature of the ejecta increases as the ISM density gets higher. On the other hand, the electron temperature gets more rapidly cooled down in the cases of denser ISM. These results indicate the degree of the RP increase with ISM density, as we described in Chapter 6. Since it is possible that the ISM components have modest contributions to the observed RPs, we compare the average temperatures of the ISM extracted from the simulations with the temperatures obtained from the observations as shown in Figures 7.13 and 7.14. We get clearly lower ionisation temperatures than that of the observations in all of the simulations.

Overall, the simulations with the ISM densities of $n_{ISM} = 10$ or 30 cm^{-3} agree well with observational trends. These simulations show obvious presence of the RPs after ages of $\sim 10^4$ yr. Particularly, the ionisation temperatures of the simulations are in excellent agreement with

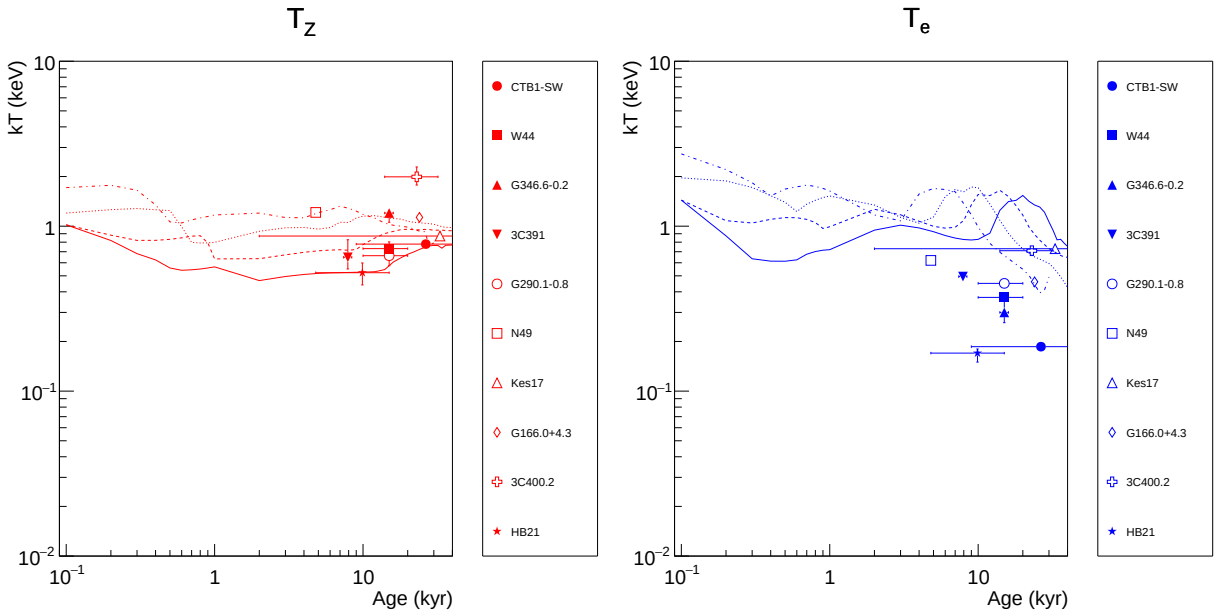

Figure 7.11: The ionisation (left) and electron (right) temperature estimated from the observations and the averaged temperatures extracted from the simulations of the ejecta. The solid, dashed, dotted, and dot-dashed lines denote the simulations of n_{ISM} = 1, 3, 10, and 30 cm^{-3}, respectively. The ionisation temperatures of the simulations are in excellent agreement with the observed values. Most of the SNRs have lower electron temperatures than the simulations predicted.

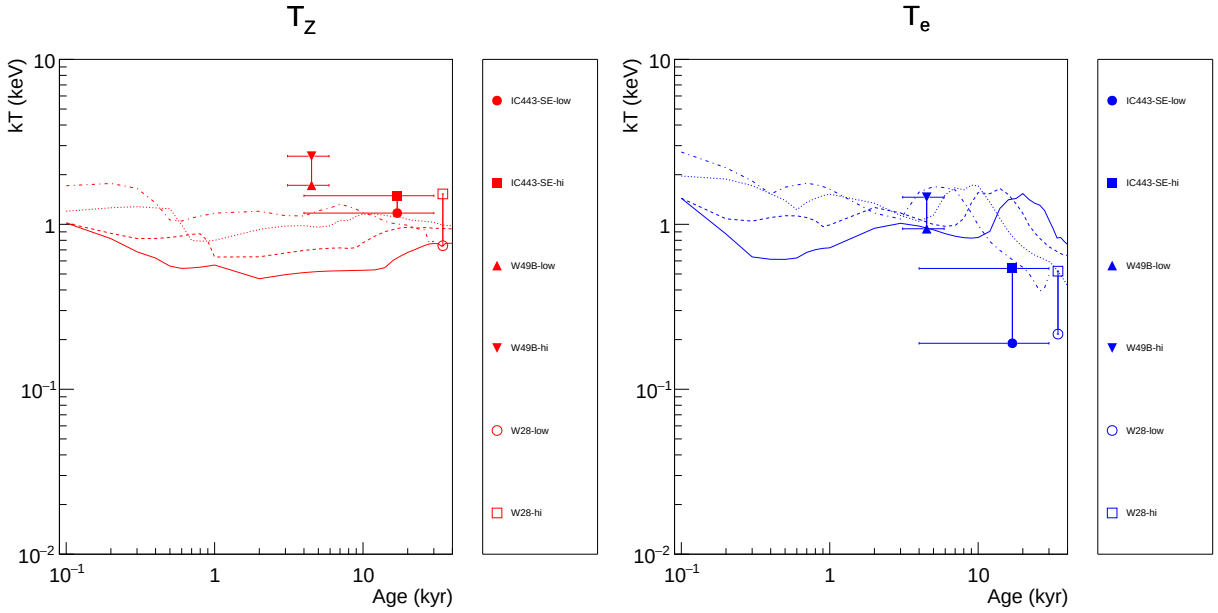

Figure 7.12: The same as Figure 7.11 but for showing observations with two temperatures models.

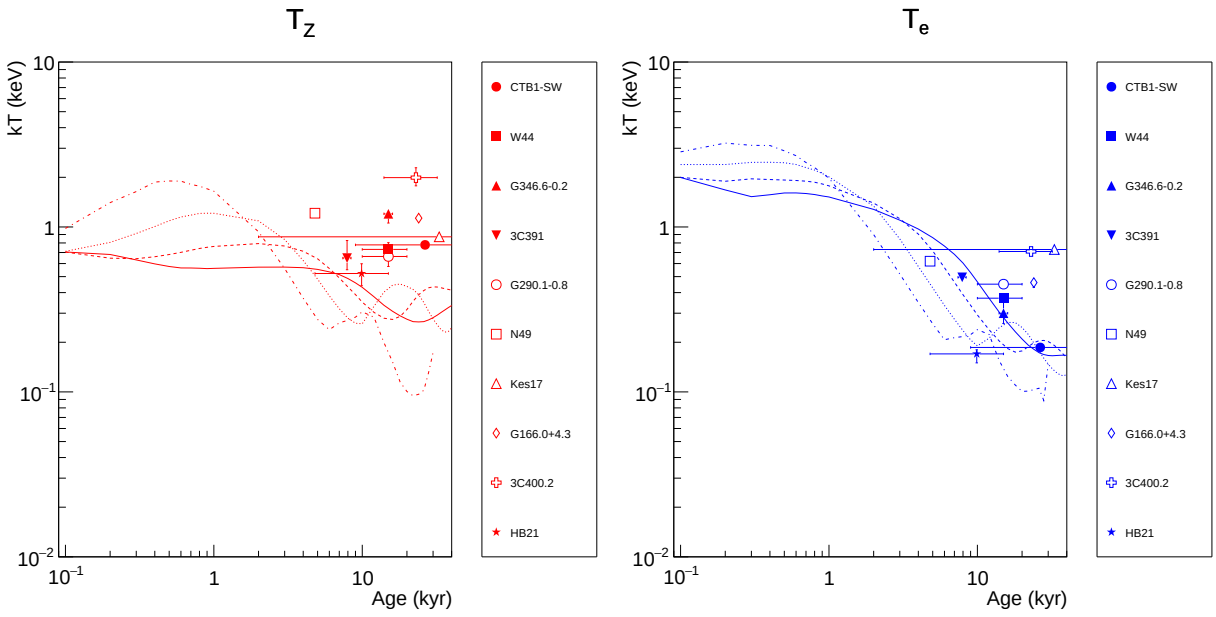

Figure 7.13: The same as Figure 7.11 but for showing simulation curves extracted from the ISM region. The ionisation temperatures of the simulations are larger than that of observed values, while the electron temperatures agree with observations.

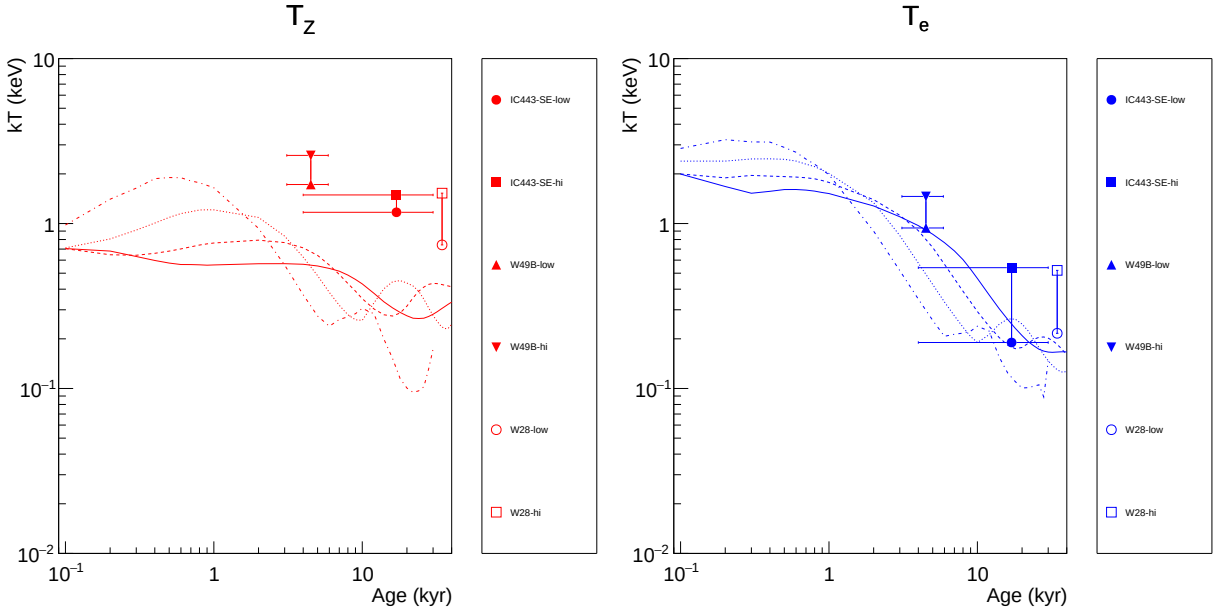

Figure 7.14: The same as Figure 7.13 but for showing observations with two temperatures models.

the observed values. This means that our code successfully produces time evolution of the ion fractions, which essentially depend on the initial shock heating and integrations of the ionisations and the recombinations of all ions after the heating. In concern of the electron temperatures, on the other hand, several objects (Kes 17, G166.0+4.3, 3C400.2, and IC 443) nicely fit to the simulations, but most of the SNRs seen to have lower temperatures than the simulations predicted, suggesting the higher degree of the RP. These difference do not necessarily mean that our code can not calculate accurate electron temperatures, since the observation list is affected by selection bias whether the RP is detected in spectra analysis. It is still important to think about how to account for the low temperature seen in the observations.

There are many possibilities of physical or astrophysical processes that can lower the electron temperature of the simulation model. Firstly, we notice the rising trend of the electron temperature of the ejecta component after 3 kyr in the simulation of $n_{ISM} = 30$ cm^{-3}. This is due to re-heating by the reverse shock which has passed by the centre of the SNR. We think that this secondary heating can be enhanced in a pure one-dimensional model, and this effect can be milder if the SN explosion and its surroundings have more complex structure. If the re-heating effect is smaller, we get a lower electron temperature in old ages.

We should also think of cooling mechanisms which are not included in our model. One of the most probable processes is thermal conduction between plasmas of SNRs (e.g. Shelton 1999). This process transports energy from the hot ejecta outward to the cold ISM, making the ejecta cooled down. Thermal conduction can also work between the shocked ISM of the SNR plasma and the surrounding ISM such as cold molecular or atomic clouds (e.g. Matsumura et al. 2017b). The thermal energy of the ejecta can be consumed for some other physical processes, such as excitation of turbulence or non-thermal particles. From an astrophysical viewpoint, the ejecta can interact with small cold clouds which are not spatially resolved in observations, reducing its thermal energy by evaporating them. The rarefaction is a one of the candidate mechanisms. If a SN expands in the dense CSM created by a high mass loss rate of the SN, the SNR plasma expands and cools when the FS pass through the dense CSM (e.g. Uchida et al. 2012, Yamaguchi et al. 2018). These processes could be included in our code in a phenomenological way, but this is beyond the scope of this thesis.

7.3 Final remarks

The discoveries of the RPs in evolved MM-SNRs surprised us because such old SNRs had been thought to reach thermal equilibrium locally. Thus, much efforts have been made for detection of the RP features, the enhanced RRC, from many objects, and for seeking a physical or astrophysical origin of the RPs. For an interpretation of the RPs, we have built a time-dependent one-dimensional plasma model simulating a SNR which produces observable quantities such as

the simplified morphology, the detailed high-resolution spectrum, and the electron and ionisation temperatures. Our model clearly illustrates that the formation of the RP is a natural consequence of the evolution of a SNR in a dense environment up to an age of 10 kyr or older. This conclusion is important because we do not assume any additional physical processes which are not fully understood. Essentially, the RP can be explained by the combination of simple processes: hydrodynamic processes including the shock heating and adiabatic cooling, energy exchanges between ions and electrons via Coulomb interactions, and collisional ionisation and recombinations of ions.

In order to look into more details, the dependence of the RP formation on parameters of the progenitor, SN explosion and wind should be studied. In this study, we use constant values for the explosion energy and progenitor mass, but they are possibly influential parameters. In addition, the radiative cooling process is calculated using simple cooling curve and this is an improvement point in future work. Moreover, the model can include additional cooling processes discussed in the previous section.

Observationally, our model holds promising application for future high-resolution spectroscopy as we have already compiled a numerical database model (so-called table model in XSPEC) which can be used in X-ray data analysis. X-ray micro-calorimeters, which have 25 times better energy resolutions compared to the Suzaku CCD, are best fitted to our purpose. For example, the XRISM satellite, scheduled for launch in 2022, will bring us much detailed spectra of MM-SNRs in which we can investigate multiple components of different parts of the plasma with even less ambiguity.

Chapter 8

Conclusions

We studied the plasma evolution of evolved SNRs. Firstly, we analysed data from the CTB 1 observation with Suzaku. The signature of recombining plasma was found in its southwestern region, likely associated with an atomic cloud. Secondly, in order to study physical and astrophysical causes of the formation of the recombining plasmas in evolved SNRs, we introduce a time-dependent one-dimensional plasma model. The model is implemented into a simulation code that treats the one-dimensional hydrodynamics of the plasma that is driven by interactions between the SN ejecta and its surroundings. In order to verify the accuracy of the code, we examine the results of the simulation using several sets of parameters. Then we compared the results of the simulation with observations of MM SNR that exhibit the signature of recombining plasma.

CTB 1 is an SNR that exhibits mixed morphology. We observed it with Suzaku for a total exposure of $\sim$ 82 ks and obtained the following results from the spectral analysis. The 0.6–2.0 keV spectra in the NE breakout region of CTB 1 were fitted with a CIE plasma model with a electron temperature (kT_e) of $\sim$ 0.3 keV, whereas those in the SW inner-shell region were well represented by an RP model with $kT_e \sim 0.19$ keV, $kT_{init} = 3.0$ keV and $n_e t \sim 9 \times 10^{11}$ cm^{-3}s. This is the first detection of an RP in CTB 1.

The characteristic morphology of CTB 1 provides us an unique opportunity to test formation scenarios of recombining plasma. Our results imply that the electron temperature in the inner-shell region is lower than that in the breakout region, and the temperature is the lowest at the rim of the shell. In addition, t_{rec} increases toward the outer region. Therefore, the thermal conduction scenario is likely for the formation of the RP in CTB 1 rather than the rarefaction scenario. The Ne abundance is almost uniform in the observed regions, whereas the Fe abundance is enhanced in the inner-shell region, suggesting the asymmetric ejecta distribution. The diffuse hard X-ray emission represented by a power-law function is detected. The photon index is $\sim$ 2.5 and the total flux is $\sim 5 \times 10^{-13}$ erg cm^{-2} s^{-1} in the 2–10 keV band. The surface brightness is peaked at the centre of CTB 1. The origin of this emission is an open question

but one possibility is a pulsar wind nebula associated with this remnant.

In order to reveal the relationship between the evolution of plasma of SNRs and the ISM density, we developed a new framework which enables us to simulate the evolution of plasma in SNRs with ages of $>10^4$ yr. Our framework consist of a hydrodynamics code and a spectral generator. The hydrodynamics code provides the method for simulation of the time evolution of electron temperatures and ion fractions for all ions. The calculation of the hydrodynamics code is based on one-dimensional hydrodynamics simulations by the Lagrangian approach. In addition to the shock heating, Coulomb interaction, balance of ionisation and recombination. The spectral generator produces X-ray spectra and images from output data of the hydrodynamics code such as the electron temperature, density of electrons and ions, and ion fractions.

Using this framework, we study the relation between the RP and ISM density, and compare simulations of different ISM densities with observations. We calculate the ionisation temperature estimated from the ion fractions in each ISM density (1, 3, 10, and 30 cm^{-3}). From dependence of the electron and ionisation temperatures on the ISM density, we obtain the results that the recombination plasma is produced in evolved SNRs ($\sim 10^4$ yr) which exploded in dense ISM. In addition, the age of a transition from the ionisation plasma to the recombination plasma is younger as a CC-SN explodes in the denser ISM. Our simulation result of $n_{ISM} = 0.5$ cm^{-3} well agrees with the observation of an evolved SNR Cygnus Loop, whose plasma is specified to be an ionising state. Our model produces basic observational figures and characteristics including the size, spectrum, electron and ionisation temperatures of the evolved shell-like SNR Cygnus Loop. We demonstrate capability of our code for simulations of evolved SNRs without any significant error.

By comparing the simulations with observations of evolved SNRs that show the presence of the recombination plasma, we successfully produce the ionisation temperatures of the simulation models which are in excellent agreement with the observed values. The lower electron temperatures with an age of $> 10^4$ yr than the ionisation temperatures obtained from simulation are consistent with observational trends. Our code clearly illustrates that the formation of the recombination plasma is a natural consequence of evolution of an SNR in a dense environment to an age of 10^4 yr or older. The RP can be explained by the combination of well understood physical processes: hydrodynamic processes including the shock heating and adiabatic cooling, energy exchanges between ions and electrons via Coulomb interactions, and collisional ionisations and recombinations of ions.

Appendix A

Comparison of simulation results with observations

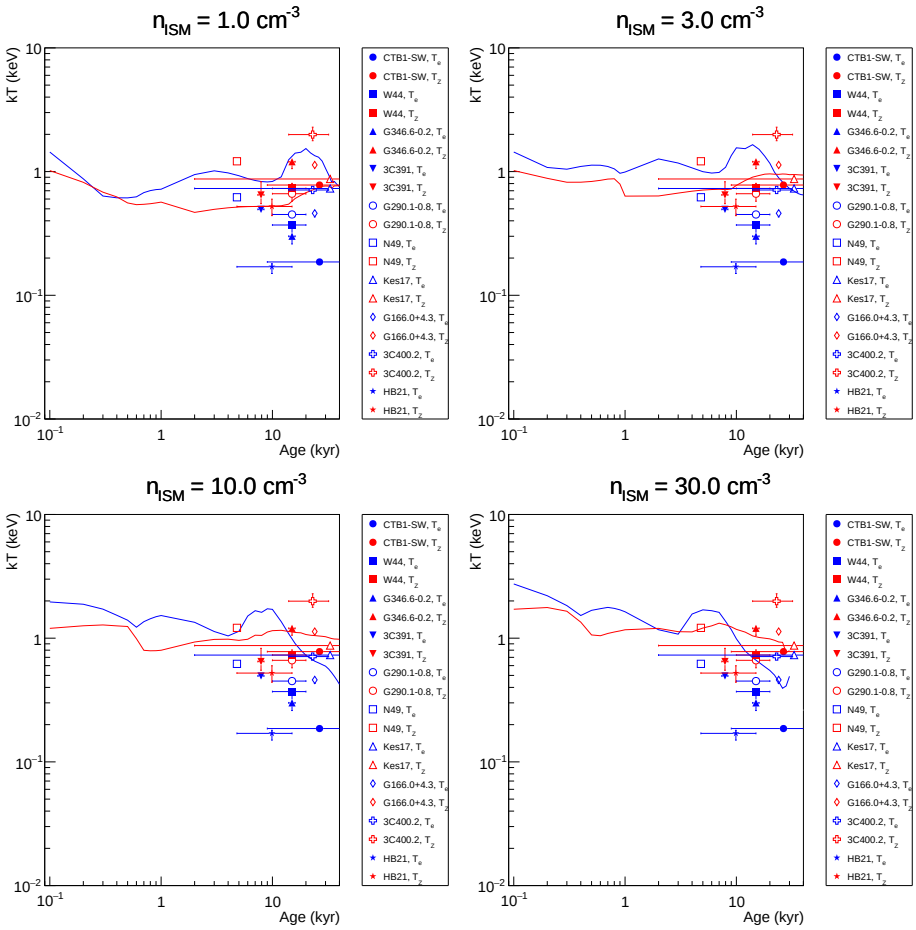

Figure 1: The electron (blue) and ionisation (red) temperatures obtained from the observational data and the average temperatures extracted from the simulations of the ejecta.

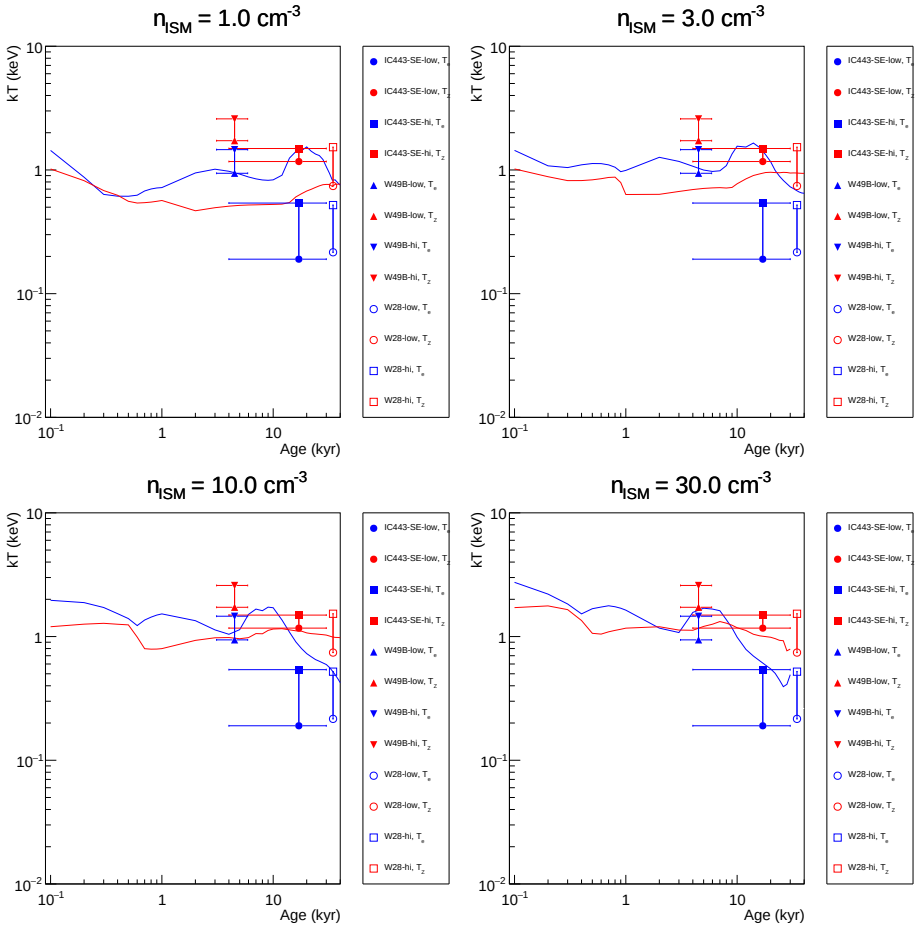

Figure 2: The same as Figure 1 but for showing observations with two temperatures models.

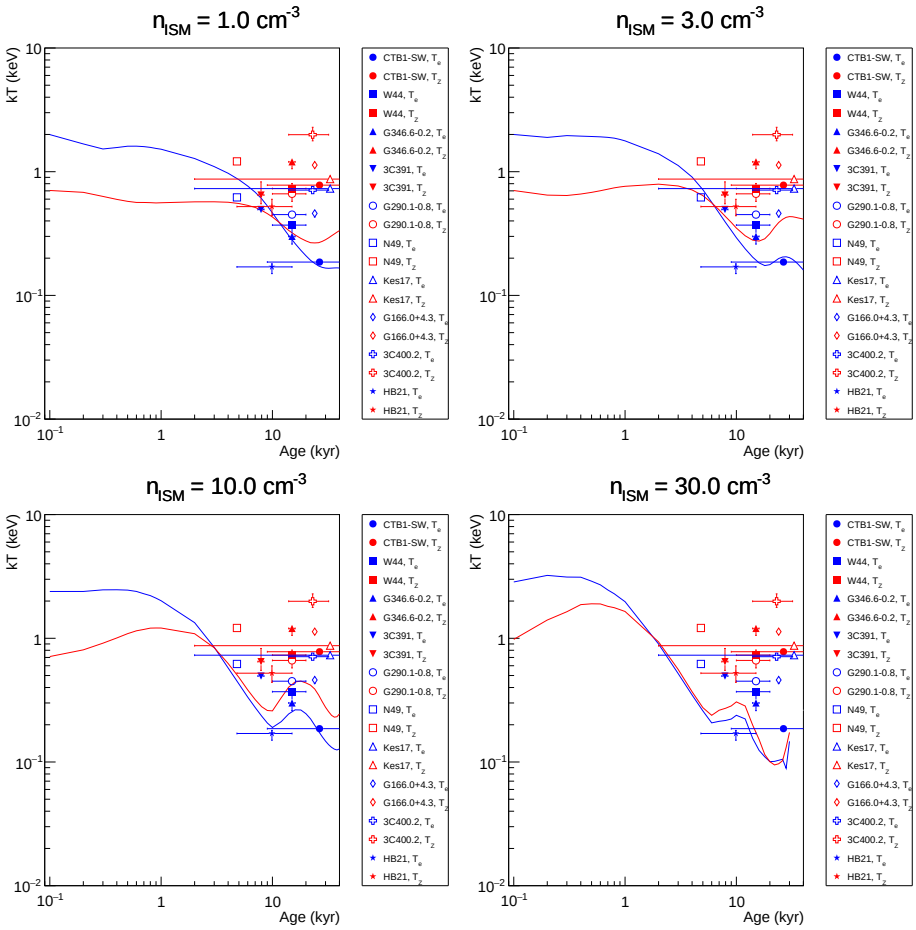

Figure 3: The same as Figure 1 but for showing simulation curves extracted from the ISM region.

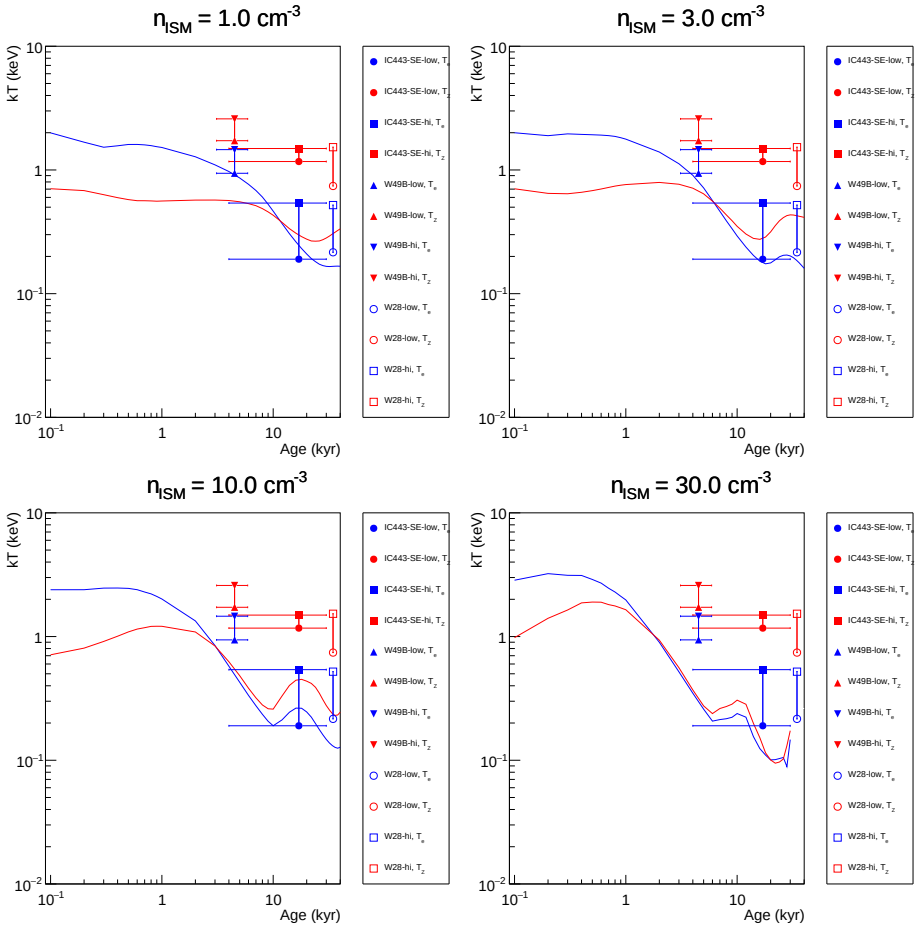

Figure 4: The same as Figure 3 but for showing observations with two temperatures models.

Bibliography

Acero, F. 2016, The Astrophysical Journal Supplement Series, 224, 50

Anders, E., & Grevesse, N. 1989, Geochimica et Cosmochimica Acta, 53, 197

Arnaud, M., & Rothenflug, R. 1985, Astron. Astrophys. Suppl. Ser., 60, 425

Badenes, C., Hughes, J. P., , G. C.-C., & Bravo, E. 2008, The Astrophysical Journal, 680, 1149

Bamba, A., Anada, T., Mori, T. D. K., et al. 2010, The Astrophysical Journal, 719, 116

Barbon, R., Ciatti, F., & Rosino, L. 1973, Astron. and Astrophys, 29, 57

Blair, W. P., Sankrit, R., & Raymond, J. C. 2005, The Astrophysical Journal, 129, 2268

Borkowski, K. J., Reynolds, S. P., & Roberts, M. S. E. 2016, The Astrophysical Journal, 819, 160

Bressaard, P. J., & van de Hulst, H. C. 1962, Rev. Mod. Phys., 34, 507

Burrows, D. N., & Guo, Z. 1994, The Astrophysical Journal, 421, 19

Byun, D.-Y., Koo, B.-C., Tatematsu, K., & Sunada, K. 2006, The Astrophysical Journal, 637, 283

Callen, J. D. 2006, Fundamentals of Plasma Physics (Madison, WI: Univ. Wisconsin)

Caswell, J. L., Murray, J. D., Roger, R. S., Cole, D. J., & CookeJ, D. . 1975, Astronomy and Astrophysics, 45, 239

Chevalier, R. A. 1974, The Astrophysical Journal, 188, 501

—. 1982, The Astrophysical Journal, 258, 790

Chevalier, R. A., & Luo, D. 1994, The Astrophysical Journal, 421, 225

Cioffi, D. F., McKee, C. F., & Bertschinger, E. 1988, The Astrophysical Journal, 334, 252

Colella, P., & Woodward, P. R. 1984, Journal of Conputational physics, 54, 174

Cox, D. P., Shelton, R. L., Maciejewski, W., et al. 1999, The Astrophysical Journal, 524, 179

Craig, W. W., & Hailey, C. J. 1997, The Astrophysical Journal, 488, 307

Elias, J. H., Matthews, K., Neugebauer, G., & Persson, S. E. 1985, The Astrophysical Journal, 296, 379

Ellison, D. C., Patnaude, D. J., Slane, P., Blasi, P., & Gabici, S. 2007, The Astrophysical Journal, 661, 879

Ellison, D. C., Patnaude, D. J., Slane, P., & Raymond, J. 2010, The Astrophysical Journal, 712, 287

Ergin, T., Sezer, A., Sano, H., Yamazaki, R., & Fukui, Y. 2017, The Astrophysical Journal, 842, 22

Fesen, R. A. 1997, The Astronomical Journal, 113, 767

Filippenko, A. V. 1988, The Astronomical Journal, 96, 6

Foster, A. R., Ji, L., Smith, R. K., & Brickhouse, N. S. 2012, The Astrophysical Journal, 756, 128

Gelfand, J. D., Castro, D., Slane, P. O., et al. 2013, The Astrophysical Journal, 777, 148

Giacani, E. B., Dubner, G., Cappa, C., & Testori, J. 1998, Astron. Astrophys. Suppl. Ser., 133, 61

Goss, W. M. 1968, The Astrophysical Journal Supplement Series, 15, 131

Green, D. 1984, Mon. Not. R. astr. Soc., 209, 449

Güdel, M., & Nazé, Y. 2009, Astronomy and Astrophysics Review, 17, 309

Hailey, C. J., & Craig, W. W. 1994, The Astrophysical Journal, 434, 635

Heyer, M. H., Brunt, C., Snell, R. L., Howe, J. E., & Schloerb, F. P. 1998, The Astrophysical Journal Supplement Series, 115, 241

Ishisaki, Y., et al. 2007, Publ. Astron. Soc. Japan, 59, S113

Itoh, H., & Masai, K. 1989, Mon. Not. R. astr. Soc., 236, 885

Itoh, N., Sakamoto, T., Kusano, S., Kawana, Y., & Nozawa, S. 2002, Astronomy and Astrophysics, 382, 722

Iwamoto, K., Brachwitz, F., Nomoto, K., et al. 1999, The Astrophysical Journal Supplement Series, 125, 439

Johnstone, C. P., & Güdel, M. 2015, Astronomy and Astrophysics, 578, 129

Kalberla, P. M. W., Burton, W. B., Hartmann, D., et al. 2005, Astronomy and Astrophysics, 440, 775

Kamitsukasa, F., Koyama, K., Uchida, H., et al. 2015, Publ. Astron. Soc. Japan, 67, 16

Kargaltsev, O., Misanovic, Z., Pavlov, G. G., Wong, J. A., & Garmire, G. P. 2008, The Astrophysical Journal, 684, 542

Karzas, W. J., & Latter, R. 1961, The Astrophysical Journal Supplement Series, 6, 167

Katsuda, S., & Tsunemi, H. 2008, Advances in Space Research, 41, 383

Katsuda, S., Tsunemi, H., Miyata, E., et al. 2008, Publ. Astron. Soc. Japan, 60, 107

Katsuragawa, M., Nakashima, S., Matsumura, H., et al. 2018, Publ. Astron. Soc. Japan, 70, 110

Kawasaki, M., Ozaki, M., Nagase, F., Inoue, H., & Petre, R. 2005, The Astrophysical Journal, 631, 935

Kawasaki, M. T., Ozaki, M., Nagase, F., et al. 2002, The Astrophysical Journal, 572, 897

Kelley, R., et al. 2007, Publ. Astron. Soc. Japan, 59, S77

Kokubun, M., et al. 2007, Publ. Astron. Soc. Japan, 59, S53

Koo, B.-C., & Heiles, C. 1991, The Astrophysical Journal, 382, 204

Kothes, R., Fedotov, K., Foster, T. J., & Uyanker, B. 2006, Astronomy and Astrophysics, 457, 1081

Koyama, K., et al. 2007, Publ. Astron. Soc. Japan, 59, S23

Kushino, A., Ishisaki, Y., Morita, U., et al. 2002, Publ. Astron. Soc. Japan, 54, 327

Landecker, T. L., Roger, R. S., & Dewdney, P. E. 1982, The Astrophysical Journal, 87, 1379

Lazendic, J. S., & Slane, P. O. 2006, The Astrophysical Journal, 647, 350

Leahy, D. A. 1987, Mon. Not. R. astr. Soc., 228, 907

Leahy, D. A., & Ranasinghe, S. 2018, The Astrophysical Journal, 866, 9

Lee, S.-H., Ellison, D. C., & Nagataki, S. 2012, The Astrophysical Journal, 750, 156

Lee, S.-H., Patnaude, D. J., Ellison, D. C., Nagataki, S., & Slane, P. O. 2014, The Astrophysical Journal, 791, 97

Lee, S.-H., Slane, P. O., Ellison, D. C., Nagataki, S., & Patnaude, D. J. 2013, The Astrophysical Journal, 767, 20

Long, K. S., Blair, W. P., White, R. L., & Matsui, Y. 1991, The Astrophysical Journal, 373, 567

Lopez, L. A., Ramirez-Ruiz, E., Castro, D., & Pearson, S. 2013, The Astrophysical Journal, 764, 50

Lozinskaya, T. A. 1981, Sov.Astron. Lett., 7, 17

Lu, F. J., Ge, M. Y., Zheng, S. J., et al. 2015, The Astrophysical Journal, 805, 142

Martínez-Rodríguez, H., Badenes, C., Lee, S.-H., et al. 2018, The Astrophysical Journal, 865, 151

Masai, K. 1994, The Astrophysical Journal, 437, 770

Masui, K., Mitsuda, K., Yamasaki, N. Y., et al. 2009, Publ. Astron. Soc. Japan, 61, 115

Matsumura, H. 2018, PhD thesis, Kyoto Univ.

Matsumura, H., Tanaka, T., Uchida, H., Okon, H., & Tsuru, T. G. 2017b, The Astrophysical Journal, 851, 73

Matsumura, H., Uchida, H., Tanaka, T., et al. 2017a, Publ. Astron. Soc. Japan, 69, 30

Mattana, F., Falanga, M., tz, D. G., et al. 2009, The Astrophysical Journal, 694, 12

McKee, C. F., & Ostriker, J. P. 1977, The Astrophysical Journal, 218, 148

Minkowski, R. 1939, The Astrophysical Journal, 89, 156

—. 1940, Publications of the Astronomical Society of the Pacific, 52, 206

Mitsuda, K., et al. 2007, Publ. Astron. Soc. Japan, 59, 1

Moffett, D. A., & Reynolds, S. P. 1994, The Astrophysical Journal, 437, 705

Moretti, A., Pagani, C., Cusumano, G., et al. 2009, Astronomy and Astrophysics, 493, 501

Nomoto, K. 1982, The Astrophysical Journal, 253, 798

Nomoto, K., Thielemann, F.-K., & Yoloi, K. 1984, The Astrophysical Journal, 286, 644

Nomoto, K., Tominaga, N., Umeda, H., Kobayashi, C., & Maeda, K. 2006, Nuclear Physics A, 777, 424

Ohnishi, T., Koyama, K., Tsuru, T. G., et al. 2011, Publ. Astron. Soc. Japan, 63, 527

Olbert, C. M., Clearfield, C. R., Williams, N. E., Keohane, J. W., & Frail, D. A. 2001, The Astrophysical Journal, 554, 205

Ozawa, M., Koyama, K., Yamaguchi, H., Masai, K., & Tamagawa, T. 2009, The Astrophysical Journal, 706, 71

Pannuti, T. G., Rho, J., Borkowski, K. J., & Cameron, P. B. 2010, The Astronomical Journal, 140, 1787

Park, S., Hughes, J. P., Slane, P. O., et al. 2012, The Astrophysical Journal, 748, 117

Patnaude, D. J., Ellison, D. C., & Slane, P. 2009, The Astrophysical Journal, 696, 1956

Patnaude, D. J., Slane, P., Raymond, J. C., & Ellison, D. C. 2010, The Astrophysical Journal, 725, 1476

Pietrzynskiski, G., Graczyk, D., Gieren, W., et al. 2013, Nature, 495, 76

Pineailt, S., Landecker, T. L., & Routledge, D. 1987, The Astrophysical Journal, 315, 580

Ranasinghe, S., & Leahy, D. A. 2017, The Astrophysical Journal, 843, 119

Rauscher, T., Heger, A., Hoffman, R. D., & Woosley, S. E. 2002, The Astrophysical Journal, 576, 323

Rauscher, T., & Thielemann, F.-K. 2000, Atomic Data and Nuclear Data Tables, 75, 1

Reynoso, E. M., Johnston, S., Green, A. J., & rbel S. Koribalski, B. 2006, Mon. Not. R. astr. Soc., 369, 416

Rho, J., & Borkowski, K. J. 2002, The Astrophysical Journal, 575, 201

Rho, J., & Petre, R. 1998, The Astrophysical Journal, 503, 167

Sato, T., Koyama, K., Takahashi, T., Odaka, H., & Nakashima, S. 2014, Publ. Astron. Soc. Japan, 66, 124

Sawada, M. 2011, PhD thesis, Kyoto Unv.

Sawada, M., & Koyama, K. 2012, Publ. Astron. Soc. Japan, 64, 81

Schlegel, E. M. 1990, Mon. Not. R. astr. Soc., 244, 269

Schure, K. M., Kosenko, D., Kaastra, J. S., Keppens, R., & Vink, J. 2009, Astronomy and Astrophysics, 508, 751

Sedov, L. I. 1959, Similarity and Dimensional Methods in Mechanics (New York: Academic Press)

Sekiya, N., Yamasaki, N. Y., Mitsuda, K., & Takei, Y. 2014, Publ. Astron. Soc. Japan, 66, 1

Serlemitsos, P. J., et al. 2007, Publ. Astron. Soc. Japan, 59, S9

Shelton, R. L. 1999, The Astrophysical Journal, 521, 217

Slane, P., Helfand, D. J., van der Swaluw, E., & Murray, S. S. 2004, The Astrophysical Journal, 616, 403

Slane, P., Lee, S.-H., Ellison, D. C., et al. 2014, The Astrophysical Journal, 783, 33

Slane, P., Smith, R. K., Hughes, J. P., & Petre, R. 2002, The Astrophysical Journal, 564, 284

Smith, A., Jones, L. R., Peacock, A., & Pye, J. P. 1985, The Astrophysical Journal, 296, 469

Smith, R. K., & Brickhouse, N. S. 2001, Spectroscopic Challenges of Photoionized Plasmas, 247, 161

Spitzer, L. 1965, Physics of Fully Ionized Gases (Physics of Fully Ionized Gases, New York: Interscience Publishers)

Suzuki, H., Bamba, A., Nakazawa, K., et al. 2018, Publ. Astron. Soc. Japan, 70, 75

Takahashi, T., et al. 2007, Publ. Astron. Soc. Japan, 59, S35

Takeuchi, Y., Yamaguchi, H., & Tamagawa, T. 2016, Publ. Astron. Soc. Japan, 68, 1

Tatematsu, K., Fukui, Y., Landecker, T. L., & Roger, R. S. 1990, Astronomy and Astrophysics, 237, 189

Tawa, N., Hayashida, K., Nagai, M., Nakamoto, H., & Tsunemi, H. 2008, Publ. Astron. Soc. Japan, 60, 11

Taylor, G. 1950, Royal Society of London Proceedings Series A, 201, 159

Troja, E., Bocchino, F., Miceli, M., , & Reale, F. 2008, Astronomy and Astrophysics, 485, 777

Truelove, J. K., & Mckee, C. F. 1999, The Astrophysical Journal Supplement Series, 120, 299

Tsunemi, H., Katsuda, S., Nemes, N., & Miller, E. D. 2007, The Astrophysical Journal, 671, 1717

Uchida, H. 2010, PhD thesis, Osaka Univ.

Uchida, H., Koyama, K., & Yamaguchi, H. 2015, The Astrophysical Journal, 808, 77

Uchida, H., Tsunemi, H., Katsuda, S., Kimura, M., & Kosugi, H. 2009, Publ. Astron. Soc. Japan, 61, 301

Uchida, H., Koyama, K., Yamaguchi, H., et al. 2012, Publ. Astron. Soc. Japan, 64, 141

Utrobin, V. P. 1996, Astronomy and Astrophysics, 306, 219

Uyaniker, B., Reich, W., Yar, A., Kothes, R., & rst, E. F. 200, Astronomy and Astrophysics, 389, 61

Velazquez, P. F., Dubner, G. M., Goss, W. M., & Green, A. J. 2002, The Astronomical Journal, 124, 2145

Vink, J. 2012, Astronomy and Astrophysics Review, 20, 1

Vink, J., Bamba, A., & Yamazaki, R. 2011, The Astrophysical Journal, 727, 131

Washino, R., Uchida, H., Nobukawa, M., et al. 2016, Publ. Astron. Soc. Japan, 68, 1

Watson, M. G., & otheres. 2009, Astronomy and Astrophysics, 493, 339

Webbink, R. F. 1984, The Astrophysical Journal, 277, 355

Welsh, B. Y., Sallmen, S., Sfeir, D., & Lallement, R. 2002, Astronomy and Astrophysics, 391, 705

Wheeler, J. C., Harkness, R. P., Barker, E. S., Cochran, A. L., & Wills, D. 1987, The Astrophysical Journal, 313, 69

White, R. L., & Long, K. S. 1991, The Astrophysical Journal, 373, 543

Wilms, J., Allen, A., & Mccray, R. 2000, The Astrophysical Journal, 542, 914

Wolszczan, A., Cordes, J. M., & Dewey, R. J. 1991, The Astrophysical Journal, 372, 99

Yamaguchi, H., Ozawa, M., Koyama, K., et al. 2009, The Astrophysical Journal, 705, 6

Yamaguchi, H., Badenes, C., Petre, R., et al. 2014a, The Astrophysical Journal Letters, 785, 27

Yamaguchi, H., Eriksen, K. A., Badenes, C., et al. 2014b, The Astrophysical Journal, 780, 136

Yamaguchi, H., Tanaka, T., Wik, D. R., et al. 2018, The Astrophysical Journal Letters, 868, 35

Yamaguchi, S., Nobukawa, M., Koyama, K., & Yonemori, M. 2013, Publ. Astron. Soc. Japan, 65, 6

Yar-Uyaniker, A., Uyaniker, B., & Kothes, R. 2004, The Astrophysical Journal, 616, 247

Yusef-Zadeh, F., Wardle, M., Wardle, J., & Sakano, M. 2003, The Astrophysical Journal, 585, 319

Zel'dovich, Y. B., & Raizer, Y. P. 1966, Physics of shock waves and high-temperature hydrodynamic phenomena (New York: Academic Press)

Zhu, H., Tian, W. W., & Zuo, P. 2014, The Astrophysical Journal, 793, 95

Acknowledgements

My deepest appreciation goes to my supervisor Professor T. Takahashi who has guided and encouraged me over the five years of my graduate course. I would like to express my deep gratitude to Dr. S.-H. Lee. He introduced me to this study and provided a deep insight into nature of supernova remnants and many essential discussions. I am very much thankful to Dr. H. Odaka for many helpful discussion on astrophysics and hydrodynamics simulations. Dr. S. Nakashima and H. Matsumura provided an insight into the analysis and many discussion on supernova remnants. I deeply appreciate to them. I also wish to thank Dr. A. Simionescu for fruitful discussions on astrophysics and valued feedback. Professor Y. Uchiyama, Dr. A. Bamba, Dr. T. Tanaka, Dr. Y. Uchida and M. Arakawa gave me essential ideas about the analysis and detailed discussions on physics of supernova remnants. I am very grateful to Dr. P. Caradonna. He read of my thesis all night for several days and gave me helpful comments. I would like to express my gratitude to all the people of Takahashi group. Finally, I thank my family for their support and understanding.

This work is supported by Research Fellowships of Japan Society for the Promotion of Science (JSPS) for Young Scientists and KAKENHI grant number 16J02332.